EDUCACIÓN
SECRETARÍA DE EDUCACIÓN PÚBLICA

Instituto Politécnico Nacional
"La Técnica al Servicio de la Patria"

Research in Computing Science

Vol. 154 No. 4
Abril 2025

Research in Computing Science

***RESEARCH IN COMPUTING SCIENCE**, Año 25, Volumen 154, No. 4, Abril de 2025, es una publicación mensual, editada por el Instituto Politécnico Nacional, a través del Centro de Investigación en Computación. Av. Juan de Dios Bátiz S/N, Esq. Av. Miguel Othón de Mendizábal, Col. Nueva Industrial Vallejo, C.P. 07738, Ciudad de México, Tel. 57 29 60 00, ext. 56571. https://www.rcs.cic.ipn.mx. Editor responsable: Dr. Grigori Sidorov. Reserva de Derechos al Uso Exclusivo del Título No. 04-2019-082310242100-203. ISSN: en trámite, otorgado por el Instituto Nacional del Derecho de Autor. Responsable de la última actualización de este número: el Centro de Investigación en Computación, Dr. Grigori Sidorov, Av. Juan de Dios Bátiz S/N, Esq. Av. Miguel Othón de Mendizábal, Col. Nueva Industrial Vallejo, C.P. 07738. Fecha de última modificación 04 de Abril de 2025.*

***RESEARCH IN COMPUTING SCIENCE**, Year 25, Volume 154, No. 4, April, 2025, is a monthly publication edited by the National Polytechnic Institute through the Center for Computing Research. Av. Juan de Dios Bátiz S/N, Esq. Miguel Othón de Mendizábal, Nueva Industrial Vallejo, C.P. 07738, Mexico City, Tel. 57 29 60 00, ext. 56571. https://www.rcs.cic.ipn.mx. Editor in charge: Dr. Grigori Sidorov. Reservation of Exclusive Use Rights of Title No. 04-2019-082310242100-203. ISSN: pending, granted by the National Copyright Institute. Responsible for the latest update of this issue: the Computer Research Center, Dr. Grigori Sidorov, Av. Juan de Dios Bátiz S/N, Esq. Av. Miguel Othón de Mendizábal, Col. Nueva Industrial Vallejo, C.P. 07738. Last modified on April 4, 2025.*

Advances in Optics and Photonics for Science and Engineering

Mary Carmen Peña-Gomar
Rafael Guzmán-Cabrera
Miguel Torres-Cisneros (eds.)

Instituto Politécnico Nacional, Centro de Investigación en Computación
México 2025

ISSN: in process

Formerly ISSNs: 1870-4069, 1665-9899

Instituto Politécnico Nacional (IPN)
Centro de Investigación en Computación (CIC)
Av. Juan de Dios Bátiz s/n esq. M. Othón de Mendizábal
Unidad Profesional "Adolfo López Mateos", Zacatenco
07738, México D.F., México

http://www.rcs.cic.ipn.mx
http://www.ipn.mx
http://www.cic.ipn.mx

Indexed in LATINDEX, DBLP and Periodica

Electronic edition

ISSN 1870-4069

Table of Contents

Page

ISSN 1870-4069

Crystal 3D Analysis in Micrographs Applied to Cellular COVID Anomalies Identification

Bolivia Cuevas-Otahola[1], Jesús Arriaga-Hernandez[2], María Morín-Castillo[1], José Oliveros-Oliveros[2], Ana Vega-Salgado[3]

[1] Benemérita Universidad Autónoma de Puebla, Facultad de Ciencias de la Electrónica, Mexico

[2] Benemérita Universidad Autónoma de Puebla, Facultad de Ciencias Físico Matemáticas, Mexico

[3] Instituto Nacional de Astrofísica, Departamento de Óptica, Mexico

{bolivia.cuevasotahola, jesus.arriagahernandez}@viep.com.mx, maria.morin@correo.buap.mx, oliveros@fcfm.buap.mx, karem_vega@inaoe.mx

Abstract. In this work, we introduce a set of algorithms, constituting an image processing technique based on algebraic-topological and probabilistic concepts, to carry out 3D objects recognition in flat images (FI) with flat illumination and perpendicular to the objects plane. Such features are found in micrographs from SEM (Scanning Electron Microscope), TEM (Transmission Electron Microscope), and HIM (Helium Ion Microscopy). Hence, our work is based on the analysis of FI obtained by HIM to observe the COVID-19 behavior in controlled cell cultures. We found a certain optimization in the characterization of anomalies due to COVID-19 for cell cultures Vero E6, infected with COVID-19, allowing us to determine if the COVID-19 overlaps or joins (as a cell anomaly deforming a given zone) the cell membrane.

Keywords: Image processing, helium ion microscopy (HIM), 3d objects recognition, COVID-19 cell behavior, cell culture anomalies.

1 Introduction

In this work, we obtain 3D objects from FI obtained by HIM for Vero 6 cells infected with COVID-19, obtained and analyzed with a medical scope by Frese et al. [6]. To this aim, we set as a base the algorithms developed by Arriaga et al. [4, 3], Gerchberg-Saxton [7] modified with the 2D Legendre polynomials [2] based on the concepts to build the isomorphism in Arriaga et al. [1], to identify and analyze anomalies as a source of cell pathologies from their GT.

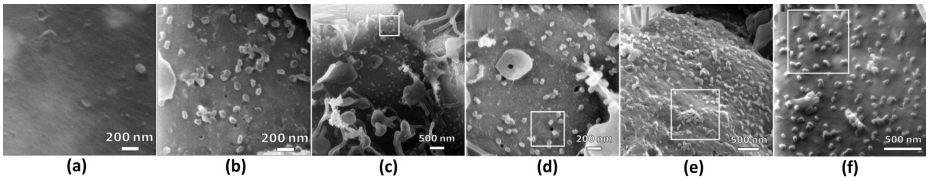

Fig. 1. In (a), we show mock-infected cells with FOV $1.7\,\mu\mathrm{m}$, in (b) MOI-1 with FOV $1.7\,\mu\mathrm{m}$, in (c) MOI-1 at FOV $5\,\mu\mathrm{m}$, and in (d) FOV at $2\,\mu\mathrm{m}$, without charge compensation in (e) and (f) MOI-1 with charge compensation with FOV $3.5\,\mu\mathrm{m}$, and $2\,\mu\mathrm{m}$.

We have developed these techniques to segment images using the GT histogram and filter using binary masks [8]. On the other hand, we developed the Gercberg-Saxton with the 2D Legendre polynomials [4] to recover the information and reduce the image noise. We increase the image resolution creating intermediate points between the original image pixels by interpolating in terms of the 1D Legendre polynomials in probabilistic regimes [2], allowing us to observe anomalies leading us to the identification of pathologic sources.

1.1 Main Applied Techniques

We use an isomorphism based on the GT images analysis, with flat illumination perpendicular to the analyzed object (see Arriaga et al. [1]), with a base $\widehat{e_1}$ (pixel 1) and $\widehat{e_0}$ (pixel 0) in a linear combination $\overrightarrow{P_{i,j}} = \alpha_{i,j}\ \widehat{e_1} + \beta_{i,j}\ \widehat{e_0}$, with $\alpha_{i,j}$ and $\beta_{i,j}$ scalars in $\mathbb{R}$, and i, j, denoting the matrix entries, rows and columns, respectively.

We obtain the vector space V_{RM}. We re-scale the GT in $l = \{l_i \mid i \in [0, 255] \subset \mathbb{Z}\}$ to $g = \{g_j \mid \{j \in [1,\ 256] \subset \mathbb{Z}\} \cup 0\}$, associating the white color to the tone g_{256}, and black with g_1. Hence, the FI image is given by $\{\widehat{e_0},\ \widehat{e_1}\}$, generating the FI with $\overrightarrow{K_{i,j}} = \gamma_{i,j}\ \widehat{e_1} + \eta_{i,j}\ \widehat{e_0}$, with $\gamma_{i,j}$ and $\eta_{i,j}$ scalars in $[1,\ 256] \subset \mathbb{Z} \subset \mathbb{R}$. The latter results in $(\{\widehat{e_0},\ \widehat{e_1}\})$ for the vectors spaces V_{RM}, and V_{PI}, where the space V_{RM} is built from the space V_{IP}, defining an isomorphism [1]. Hence, we define:

Let V_{RM} the vector space defined as the RM images, V_{FI} the vector space defining the FIs and the metric d (a real function). If for two vectors from different pixels and gray tones holds $d\left(\overrightarrow{K_{l,h}},\ \overrightarrow{K_{i,j}}\right) = 0$, then, for the pixels in which g reaches a minimum difference holds $T(K_{i,j}) = P_{i,j}$, and $T(K_{l,h}) = P_{l,h}$ simultaneously.

Here $d(.,.)$ is a metric function, representing, in this case, the distance between different GT vectors regarding the previously mentioned base, and T is a linear mapping. We modify the Gerchberg-Saxton algorithm with the 2D Legendre polynomials [4], considering the algorithm by Gerchberg et al. [7], where a numerical Fourier transform (FFT) is used to reduce noise and recover the phase.

We optimize the iterative process before applying the inverse transform (IFFT), performing a low-order multilinear fit based on the 2D Legendre polynomials in Arriaga et al. [4]. Finally, we use the 1D Legendre polynomials (LP) as a base capable of generating any family of polynomials based on the LP from a linear regression.

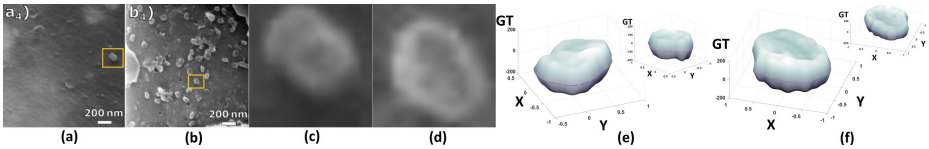

Fig. 2. In (a) and (b), we show a simple segmentation, in (c) and (d) the Gerchberg-Saxton algorithm [7] application, modified with the 2D-LP [2], and in (e) and (f) the 3D objects applying the isomorphism in Arriaga et al. [1].

We build the most probable pixels between the existing pixels, using linear fits, interpolations, and regressions (Arriaga et al. [2]), generating an image with a higher resolution, having the most probable information according to that of the original image, based in probabilistic theory and linear algebra.

1.2 Image Selection and Segmentation

The HIM (Helium ion microscopy) image analysis, is characterized by the obtained sub-nanoscale range images [6], in cell biology [5], stem cells [10], and with less impact in the analysis of biological samples. The HIM application to visualize viruses and hosts has been used in the analysis of E. coli bacteria infected with Fago T4 [9], etc.

We obtain medical images of Vero E6 cells infected with COVID-19 from the work by Frese et al. [6], using an innovative technique in the area of HIM (Helium ion Microscopy). We focused on the results shown in Fig. 1 with size 1024×1024 for a Vero E6 analysis, biologically mock-infected and infected at MOI (multiplicity of infection) of approximately 1 (MOI 1).

In Fig. 1 (a), we show mock-infected cells with FOV (field of view) of $1.7\,\mu\mathrm{m}$, in Fig. 1 (b) MOI-1 infected cells with FOV of $1.7\,\mu\mathrm{m}$. We show the results by Frese [6] with the effects of the deposited carbon over the samples during the images formation with the HIM. However, due to the involved charge conductivity, the study region looks brighter, showing an infected cell in MOI-1 at a FOV of $5\,\mu\mathrm{m}$ in Fig. 1 (c).

Subsequently, we move over the cell culture plane to obtain an image with a FOV of $2\,\mu\mathrm{m}$ in Fig. 1 (d), in both cases without compensating the charge. Finally, we obtain cell culture images of the infected cells in MOI-1 with charge compensation with FOV $3.5\,\mu\mathrm{m}$ in Fig. 1 (e), showing, subsequently, a different sample with FOV $2\,\mu\mathrm{m}$.

2 Results

In the first place, we focus on the interest zones in each image (Fig. 1) to carry out a preliminary segmentation procedure, highlighting the objectives of the base work, analyzing the cell cultures with COVID-19, where we observe cell anomalies joined to the membrane and just overlapped.

Hence, in Fig. 2 (a) and (b), we show a simple segmentation procedure with a square region (similar to the original one in Frese, in their Figs. 1 (a) and (b), to show the extent of our processing techniques). Subsequently, we apply the i-LP by Arriaga et al. [2] to increase the image resolution from 100×100 to 700×700 pixels with a mean error margin of 0.037% regarding the zoom-in performed by Frese [6].

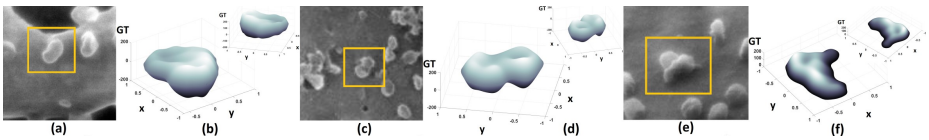

Fig. 3. In (a), (c) and (e), we show the i-LP (Arriaga et al. [2]) application, the Gerchberg-Saxton [7] modified in Arriaga et al. [4] and the isomorphism by Arriaga et al. [1], to obtain an object with a 3D relief, with a resolution of 1024×1024 pixels in (b), (d), and (f).

In Fig. 2 (c) and (d), we show the Gerchberg-Saxton algorithm application [7] modified with the 2D-LP [2], with a low-order in each iteration (degrees 3, 4, 5 and 6 of the 2D Legendre polynomials) [4], and in Figs. 2 (e) and (f), we show normalized images (in GT with magnitudes up to 1) of the application of the isomorphism in Arriaga et al. [1] to obtain the 3D profile (as a 3D object in Matlab ®) and, in the upper panel, we include an image rotation.

The heights identified by the isomorphism are an approximation to the 3D objects from the image GT, highly depending on the technique (HIM, SEM, or TEM), due to the illumination, and image scale, since from a longitudinal measurement, the GT is interpreted to provide an approximate height value. We analyze the images in Figs. 1 (b), (c), (f) of the results by Frese et al. [6] to apply the simple segmentation procedure and a more complex one by polygons or histograms in GT to segment particles and cells contaminated by COVID-19.

In Fig. 3, we apply i-LP by Arriaga et al. [2] to segment the images in Figs. 1 (c), (b), (f), respectively, and subsequently applied the Gerchberg-Saxton [7] modified with the 3th-degree 2D Legendre polynomials, as shown in Arriaga et al. [4]. As the following step, we apply the isomorphism by Arriaga et al. [1] to obtain an object as a 3D relief as we show in Figs. 3 (b), (d) and (f).

We highlight the objective of identifying the coupling or contamination due to COVID-19 in the cell culture in Figs. 3 (b) and (d), observing a superposition. However, in the case in Fig. 3 (f), we show more advanced contamination, where the COVID-19 is completely attached to the cell membrane, being an anomaly yet to be studied to determine the extent in the affected organism from its cellular structure.

3 Conclusions

In this work, we consider a set of techniques we have developed in medical image processing [8] with mathematical bases for the identification of sources as cell anomalies. Such techniques are the i-LP by Arriaga et al. [2], the Gerchberg-Saxton modified with the 2D Legendre polynomials by Arriaga et al. [4] and the isomorphism by Arriaga et al. [1], with the aim of segmenting, increasing the resolution, reducing noise and recovering the phase, obtaining 3D profiles of objects in flat images.

The main objective was recovering the 3D profiles, subsequently accomplished in Figs. 2 and 3, and sharing the objective in Frese et al. [6], we can determine if the COVID-19 particles are overlapped to the cell culture or represent a cell anomaly by deforming, feeding, consuming, mutating, and modifying the cell membrane. We resolve the latter in the objects in Figs. 3 (b), (d) and (f).

Acknowledgments. The authors want to thank Benemérita Universidad Autónoma de Puebla (BUAP) for the support given during this research work. We also thank CONACYT (Consejo Nacional de Ciencia y Tecnologia, México).

References

1. Arriaga-Hernández, J., Cuevas-Otahola, B., Jaramillo-Núñez, A., Oliveros-Oliveros, J., Morín-Castillo, M.: Optical-topological concepts in isomorphisms projecting bi-Ronchi masks to obtain 3D profiles from objects in 2d images. Applied Optics, vol. 59, no. 33, pp. 10464–10473 (2020) doi: 10.1364/AO.401316
2. Arriaga-Hernández, J., Cuevas-Otahola, B., Oliveros-Oliveros, J., Morín-Castillo, M.: Two-dimensional legendre polynomials as a basis for interpolation of data to optimize the solution of the irradiance transport equation analyzed as a boundary problem on surfaces testing. Applied Optics, vol. 58, no. 18, pp. 5057–5066 (2019) doi: 10.1364/AO.58.005057
3. Arriaga-Hernández, J., Cuevas-Otahola, B., Oliveros-Oliveros, J., Morín-Castillo, M.: Geometric aberrations in the 3D profile of microparticles observed in optical trapping using 2D legendre polynomials. Optik, vol. 23, no. 12, pp. 1–25 (2021) doi: 10.1016/j.ijleo.2021.168123
4. Arriaga-Hernández, J. A., Cuevas-Otahola, B., Oliveros-Oliveros, J., Morín-Castillo, M.: 3D mapping in optical trapping of polystyrene particles applying the Gerchberg-Saxton modified with 2D legendre polynomials. Journal of Optics, vol. 23, no. 12, pp. 1–11 (2021) doi: 10.1088/2040-8986/ac303c
5. Bazou, D., Behan, G., Reid, C., Boland, J. J., Zhang, H. Z.: Imaging of human colon cancer cells using He-Ion scanning microscopy. Journal of Microscopy, vol. 242, no. 3, pp. 290–294 (2011) doi: 10.1111/j.1365-2818.2010.03467.x
6. Frese, N., Schmerer, P., Wortmann, M., Schörmann, M., König, M., Westphal, M., Weber, F., Sudhoff, H., Gölzhäuser, A.: Imaging of SARS-CoV-2 infected vero E6 cells by helium ion microscopy. Beilstein Journal of Nanotechnology, vol. 12, no. 13, pp. 172–179 (2021) doi: 10.3762/bjnano.12.13
7. Gerchberg, R. W., Saxton, W. O.: A practical algorithm for the determination of the phase from image and diffraction plane pictures. Optik, vol. 35, no. 2, pp. 237–246 (1972)
8. Jaramillo-Núñez, A., Arriaga-Hernández, J., Cuevas-Otahola, B., Pérez-Meza, M., Sánchez-Rinza, B.: Diagnostic software proposal for bone scan follow-up using false color based on the gammagrams analysis from gray tone histograms. Biomedical Physics and Engineering Express, vol. 7, no. 3, pp. 1–11 (2021) doi: 10.1088/2057-1976/abe680
9. Leppänen, M., Sundberg, L. R., Laanto, E., de Freitas-Almeida, G., Papponen, P., Maasilta, I. J.: Imaging bacterial colonies and phage–bacterium interaction at sub-nanometer resolution using helium-ion microscopy. Advanced Biosystems, vol. 1, no. 8, pp. 1700070 (2017) doi: 10.1002/adbi.201700070
10. Schürmann, M., Frese, N., Beyer, A., Heimann, P., Widera, D., Mönkemöller, V., Huser, T., Kaltschmidt, B., Kaltschmidt, C., Gölzhöuser, A.: Helium ion microscopy visualizes lipid nanodomains in mammalian cells. Small, vol. 11, no. 43, pp. 5781–5789 (2015) doi: 10.1002/smll.201501540

ISSN 1870-4069

Fractal and Mathematical Inductive Diffraction Patterns in SLM

Jesús Arriaga-Hernandez[1], Bolivia Cuevas-Otahola[2], María Morín-Castillo[2], José Oliveros-Oliveros[1]

[1] Benemérita Universidad Autónoma de Puebla, Facultad de Ciencias Físico Matemáticas, Mexico

[2] Benemérita Universidad Autónoma de Puebla, Facultad de Ciencias de la Electrónica, Mexico

{jesus.arriagahernandez, bolivia.cuevasotahola}@viep.com.mx, maria.morin@correo.buap.mx, oliveros@fcfm.buap.mx

Abstract. We simulate diffraction patterns (fringes and square apertures) from a generating base and the necessary conditions to create an arbitrary fringes number and apertures. We study the mathematical properties of such construction and compared them with the properties of a fractal. Finally, from the fractal consideration and apertures size, we obtain that the Fraunhofer diffraction analysis for the LCD as a diffractive element is a mathematical inductible pattern.

Keywords: Diffraction patterns, liquid crystal spatial light modulator, fractal, Fraunhofer diffraction analysis, mathematical inductible pattern.

1 Introduction

In this work, we build an algorithm to simulate and LCSLM (Liquid Crystal Spatial Light Modulator-SLM, which we will refer to as LCD) without considering its chemistry and all the proper polarization elements corresponding to the arrays involving SLM [10, 16, 7, 1]. We idealized the LCD resembling a fractal [5, 17], from a base constituted by a square of transmission equal to 1 surrounded by 0-transmission squares. Subsequently, we validated the LCD from its diffractive features [1, 13]. We propose a mathematically inductible high-order diffractive process [8] to validate the $N \times N$ resolution of the simulated LCD.

2 Methodology

We do not consider the polarization effects for the sake of the LCD design as a simulated diffractive element since numerically, the wavefront can be built and visualized straightforwardly. We bear this in mind since it is a common practice to place the polarizer before and after the LCSLM, as in [1, 13].

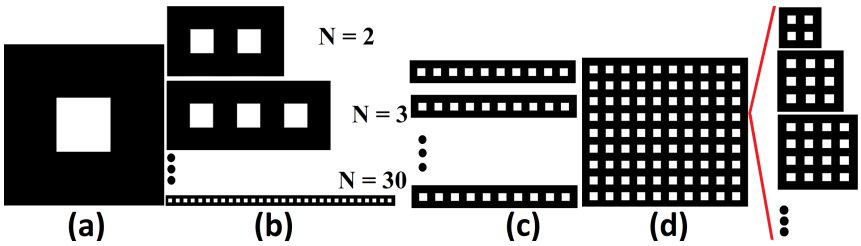

Fig. 1. We show the design and construction of our LCD, simulated from the base (a) with nine zero-valued squares surrounding a square with a value equal to 1. In (b), we show the base, generating pixels rows from square 1 by replicating it up to the desired number of pixels in a row. In (c), we show the replication of the row in (b) to generate similar rows coupling in (d), building the simulated LCD, followed by each pixel, previously described and resembling a fractal [5, 17].

On the other hand, we recall that fractals are generated from a base that can be replicated (by multiplying, summing, or joining it) in specific points and as many times as desired given the fractal, and due to the definition of the fractal symmetry and auto-similarity, which are essential fractal features [5, 17].

We show the LCD diffractive base in Fig. 1 (a), constituted by nine squares, eight black ones (opaque or with null transmission and total absorption without reflection, with zero intensity value), surrounding a white square (completely transmissible and non-absorbent, with an intensity equal to 1) resembling a window or an ideal pass-band filter (square-shaped window) [12].

We consider the squares in the base as pixels or matrix entries, as a simple conception to assign proper values simplifying the numerical simulation (completely performed in MATLAB ®in this case). The latter yields a minimum entry or pixel value equal to 1 (considering a square matrix), avoiding problems with the sampling Whittaker-Nyquist-Kotelnikov-Shannon theorem (widely-known as Nyquist-Shannon sampling theorem or Nyquist theorem) [14, 2].

In order to generate all the LCD pixels, we consider the base and integrate more elements to it, with the same features on the right side, up to a $1\times N$-pixels size [according to the desired pixels number N, see Fig. 1 (b)]. Subsequently, we build N replicas of the $1\times N$ row, with the following one placed right before the previous one, and each pixel abiding by the base and the square order 0 and 1 [see Fig. 1 (c)]. Hence, we obtain our $N\times N$-pixels LCD [see Fig. 1 (d)], built from the base [Fig. 1 (a)], resembling a fractal [5, 17].

3 Inductive Diffraction Patterns

We consider the LCD in Fig. 1 (d) as a diffractive object and with a fractal base (only the base) to analyze it by means of far field diffraction theory or Fraunhofer [11, 4, 6]. Hence, we validate the diffraction patterns simulating LCDs with different sizes 1×1 [Fig. 1 (a)], 2×2, 3×3 and 4×4 [Fig. 2 (a)-(c)]. Thus, we consider the diffractive field $U(x,y)$, from the following expression:

$$U(x,y)=\frac{e^{ikz}}{ikz}e^{i\frac{k}{2z}(x^2+y^2)}\iint_{-\infty}^{\infty}\widetilde{U_0}(\xi,\eta)e^{-i\frac{2\pi}{z\lambda}(x\xi+y\eta)}d\xi d\xi, \tag{1}$$

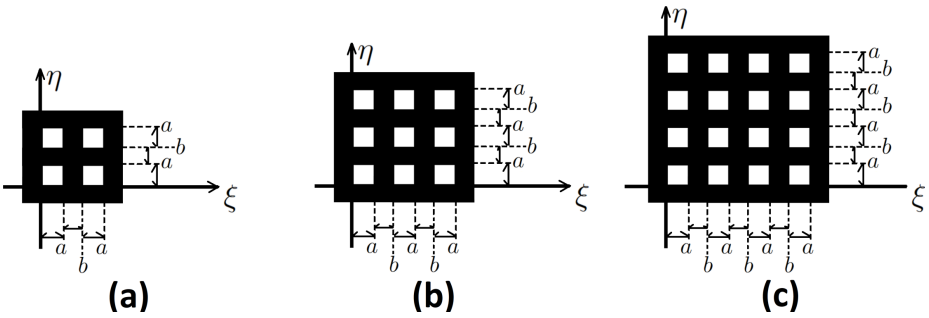

Fig. 2. We show the reference system origin position used to compute the diffractive field and the intensity for the simulated LCD of $N \times N$ pixels with $N = 1, 2, 3, ..., n$ in (a)-(c) and Fig. 1 (d), respectively.

where $\widetilde{U_0}(\xi, \eta)$ represent the diffractive object, with $\lambda = 632\,\text{nm}$ being the wavelength [11, 4, 6]. Define $A = \frac{e^{ikz}}{ikz} e^{i\frac{k}{2z}(x^2+y^2)}$ and $S_{a,b}(x) = e^{-i2\frac{\pi}{z\lambda}x(a+b)}$. By neglecting certain results in the diffraction area, such as $\text{rect}(z/a)$, and with $a = 6\,\mu\text{m}$ on the propagation axis z, we derive the intensities of the diffractive fields as $I(x, y) = \|U(x, y)\|^2$, from the arrays depicted in Fig. 1 (a), Figs. 2 (a)-(c), and Fig. 1 (d). The expressions for these intensities are as follows:

$$I(x,y) = I_{1x1} = \frac{a^4\lambda^2}{4\pi^2 z^2}\text{Sinc}^2\left(a\frac{\pi}{z\lambda}x\right)\text{Sinc}^2\left(a\frac{\pi}{z\lambda}y\right), \tag{2}$$

$$I_{2x2} = \frac{a^4\lambda^2}{4\pi^2 z^2}\text{Sinc}^2\left(a\frac{\pi}{z\lambda}x\right)\text{Sinc}^2\left(a\frac{\pi}{z\lambda}y\right)\left\|\sum_{i=0}^{1}\left[S_{a,b}(x)\right]^i\right\|^2\left\|\sum_{i=0}^{1}\left[S_{a,b}(y)\right]^i\right\|^2, \tag{3}$$

$$I_{3x3} = \frac{a^4\lambda^2}{4\pi^2 z^2}\text{Sinc}^2\left(a\frac{\pi}{z\lambda}x\right)\text{Sinc}^2\left(a\frac{\pi}{z\lambda}y\right)\left\|\sum_{i=0}^{2}\left[S_{a,b}(x)\right]^i\right\|^2\left\|\sum_{i=0}^{2}\left[S_{a,b}(y)\right]^i\right\|^2, \tag{4}$$

$$I_{4x4} = \frac{a^4\lambda^2}{4\pi^2 z^2}\text{Sinc}^2\left(a\frac{\pi}{z\lambda}x\right)\text{Sinc}^2\left(a\frac{\pi}{z\lambda}y\right)\left\|\sum_{i=0}^{3}\left[S_{a,b}(x)\right]^i\right\|^2\left\|\sum_{i=0}^{3}\left[S_{a,b}(y)\right]^i\right\|^2, \tag{5}$$

$$I_{NxN}(x,y) = \frac{a^4\lambda^2}{4\pi^2 z^2}\text{Sinc}^2\left(a\frac{\pi}{z\lambda}x\right)\text{Sinc}^2\left(a\frac{\pi}{z\lambda}y\right)\left\|\sum_{i=0}^{N-1}\left[S_{a,b}(x)\right]^i\right\|^2\left\|\sum_{i=0}^{N-1}\left[S_{a,b}(y)\right]^i\right\|^2. \tag{6}$$

Hence, from Eq. 6, we can show that the diffractive field intensity $I_{N\times N}$ is inductible, and we can extend the result for an $n \times n$-LCD with n an arbitrary integer, resembling a fractal. The latter is based on the Geometric Series [15], [3], [9], which is a converging series, considering the diffraction principles of the parameter A. Such a series is described by:

$$T^n = \sum_{i=0}^{n} z^i = z^0 + z^1 + z^2 + z^3 + ... + z^n = \sum_{i=0}^{n} z^i = \frac{1 - z^{n+1}}{1 - z}. \tag{7}$$

It is possible to generalize the diffractive field expression in terms of:

$$U_{N\times N}(x,y) = a^2 A A_a(x) A_a(y) \operatorname{Sinc}\left(a\frac{\pi x}{z\lambda}\right) \operatorname{Sinc}\left(a\frac{\pi y}{z\lambda}\right) \times \left\{\frac{1-\exp\left(-iNx\left(\frac{2\pi(a+b)}{z\lambda}\right)\right)}{1-\exp\left(-ix\left(\frac{2\pi(a+b)}{z\lambda}\right)\right)}\right\} \times \left\{\frac{1-\exp\left(-iNy\left(\frac{2\pi(a+b)}{z\lambda}\right)\right)}{1-\exp\left(-iy\left(\frac{2\pi(a+b)}{z\lambda}\right)\right)}\right\}, \tag{8}$$

$$I_{N\times N}(x,y) = \frac{a^4\lambda^2}{4\pi^2 z^2} \operatorname{Sinc}^2\left(a\frac{\pi x}{z\lambda}\right) \operatorname{Sinc}^2\left(a\frac{\pi y}{z\lambda}\right) \times \left\|\frac{1-\exp\left(-iNx\left(\frac{2\pi(a+b)}{z\lambda}\right)\right)}{1-\exp\left(-ix\left(\frac{2\pi(a+b)}{z\lambda}\right)\right)}\right\|^2 \times \left\|\frac{1-\exp\left(-iNy\left(\frac{2\pi(a+b)}{z\lambda}\right)\right)}{1-\exp\left(-iy\left(\frac{2\pi(a+b)}{z\lambda}\right)\right)}\right\|^2. \tag{9}$$

4 Conclusions

We have shown that it is possible to obtain a diffractive field resembling a fractal by considering a diffractive element with typical features of LCSLM or simply and LCD in an inductible diffraction set with its intensity reflecting the properties inherited from the diffractive construction element. In this context, it is not possible to stress the auto similarity of fractal dimension arguments. However, it is possible to analyze the diffractive field intensity, mathematically inductible, if there exists a diffractive element, meeting the periodicity conditions and features of an LCD.

Acknowledgments. The authors want to thank Benemérita Universidad Autónoma de Puebla (BUAP) for the support given during this research. We also thank CONACYT (Consejo Nacional de Ciencia y Tecnologia, México).

References

1. Agour, M., Kolenovic, E., Falldorf, C., von Kopylow, C.: Suppression of higher diffraction orders and intensity improvement of optically reconstructed holograms from a spatial light modulator. Journal of Optics A: Pure and Applied Optics, vol. 11, no. 10, pp. 1–7 (2009) doi: 10.1088/1464-4258/11/10/105405
2. Arendt, W., Schleich, W. P.: Mathematical analysis of evolution, information, and complexity. Wiley-VCH (2009) doi: 10.1002/9783527628025
3. Arfken, G., Weber, H., Harris, F. E.: Mathematical methods for physicists. Elsevier, Academic Press (2011) doi: 10.1016/C2009-0-30629-7
4. Born, M., Wolf, E.: Principles of optics: Electromagnetic theory of propagation, interference and diffraction of light. Cambridge University Press (2000) doi: 10.1017/CBO9781139644181
5. Frantz, M.: A fractal made of golden sets. Mathematics Magazine, vol. 82, no. 4, pp. 243–254 (2009) doi: 10.4169/193009809X468670
6. Goodman, J. W., Cox, M. E.: Introduction to Fourier optics. Physics Today, vol. 22, no. 4, pp. 97–101 (1969) doi: 10.1063/1.3035549

7. Hara, T.: A liquid crystal spatial light phase modulator and its applications. In: Proceedings of the International Society for Optics and Photonics International Society for Optics and Photonics/Chinese Optical Society Photonics Asia, vol. 5642, pp. 78–89 (2005) doi: 10.1117/12.577889
8. Henkin, L.: On mathematical induction. The American Mathematical Monthly, vol. 67, no. 4, pp. 323 (1960) doi: 10.2307/2308975
9. Hirst, K.: Numbers, sequences and series. Butterworth-Heinemann (1995)
10. Hornbeck, L. J.: Digital light processing for high-brightness high-resolution applications. In: Proceedings of the Projection Displays III / Electronic Imaging, vol. 3013, pp. 27–40 (1997) doi: 10.1117/12.273880
11. Mandel, L., Wolf, E.: Optical coherence and quantum optics. Cambridge University Press (1995) doi: 10.1017/CBO9781139644105
12. Najim, M.: Digital filters design for signal and image processing. Wiley-ISTE (2006) doi: 10.1002/9780470612064
13. Pérez-Cabré, E., Millán-Sagrario, M.: Liquid crystal spatial light modulator with optimized phase modulation ranges to display multiorder diffractive elements. Applied Sciences, vol. 9, no. 13, pp. 1–14 (2019) doi: 10.3390/app9132592
14. Pratt, W. K.: Digital image processing. John Wiley and Sons (2002) doi: 10.1002/0471221325.ch4
15. Roe, E. D.: Note on integral and integro-geometric series. The Annals of Mathematics, vol. 11, no. 1/6, pp. 184 (1896) doi: 10.2307/1967225
16. Slinger, C., Cameron, C., Stanley, M.: Computer-generated holography as a generic display technology. Computer, vol. 38, no. 8, pp. 46–53 (2005) doi: 10.1109/mc.2005.260
17. Wang, J., Zhang, W., Cui, Y., Teng, S.: Fresnel diffraction of fractal grating and self-imaging effect. Applied Optics, vol. 53, no. 10, pp. 2105 (2014) doi: 10.1364/ao.53.002105

ISSN 1870-4069

Interference Phenomena and Photon Statistics in a Cross Cavity

Ana Cristina Uribe-Chairez[1], José Manuel González-Vargas[1], Lizbeth Romero-Lira[1], José Javier Sánchez-Mondragón[2], Néstor Lozano-Crisóstomo[1], Julio César García-Melgarejo[1]

[1] Universidad Autónoma de Coahuila, Facultad de Ingeniería Mecánica y Eléctrica, Mexico

[2] Instituto Nacional de Astrofísica, Óptica y Electrónica, Departamento de Óptica, Mexico

julio.melgarejo@uadec.edu.mx

Abstract. We discuss the Jaynes-Cummings interactions of a two-level atom in a two-dimensional perfect cavity. Quantum superpositions in our cross-cavity configuration produce interference phenomena, which manifest as collapses and revivals in unforeseen cases by the Jaynes-Cummings Model. We also compute numerically the Mandel parameter and the second-order two-time correlation function and verify the existence of interference-improved sub-Poissonian light and photon antibunching.

Keywords: Jaynes and cummings model, novel cavity, quantum interference, antibunching.

1 Introduction

The Jaynes-Cummings Model (JCM) is one of the most important pillars of modern quantum optics, especially of the cavity quantum electrodynamics. The JCM describes the interactions between an atom and the quantized field of a perfect one-dimensional cavity [6, 2]. The study of the JCM interactions allowed the theoretical prediction of the so-called collapses and revivals that together with its experimental corroboration were a proof of the quantum nature of the light [4, 8]. Different aspects of the collapses and revivals have been discussed over the past decades; however, they are still interpreted as the result of interference between the interaction of the atom and each one of the occupation states of the cavity field.

2 Mathematical Model

Our model describes the interaction of a two-level atom with the cavity field of two perfect cavities oriented along x and y. The Hamiltonian of our system, under dipole and rotating wave approximation, is $H = H_0 + H_{\text{int}}$.

The free and the interaction components are given, respectively, by:

$$H_0 = \frac{1}{2}\hbar\omega_0\sigma_z + \hbar\omega\left(a^\dagger a + b^\dagger b\right), \tag{1}$$

$$H_{\text{int}} = \hbar\lambda_x\left(a\sigma_+ + a^\dagger\sigma_-\right) + \hbar\lambda_y\left(b\sigma_+ + b^\dagger\sigma_-\right). \tag{2}$$

In Equations (1)-(2), we denote the atomic transition frequency by ω_0 and assume that both cavities have the same frequency ω; in addition, λ_x and λ_y are the coupling constants along x and y that we will take as real quantities. The field operators a and b describe the field in our configuration, they satisfy the standard commutation rules of two independent quantum oscillators. On the other hand, the lowering $\sigma_- = |g\rangle\langle e|$ and raising $\sigma_+ = |e\rangle\langle g|$ operators govern the transitions between the excited $|e\rangle$ and the ground $|g\rangle$ states, and they satisfy the commutation rule $\sigma_z = [\sigma_+, \sigma_-]$.

The cross-cavity configuration provides the possibility of adjusting its coupling constants by changing geometrical parameters such as the geometrical orientation of the atomic dipole or the volume of each arm.

In the light of that, we define an effective coupling constant $\lambda_{\text{eff}} = \sqrt{\lambda_x^2 + \lambda_y^2}$ and the coupling parameter by $\theta = 2\arctan\left(\lambda_y/\lambda_x\right)$. The coupling constants can be conveniently written as $\lambda_x = \lambda_{\text{eff}}\cos(\theta/2)$ and $\lambda_y = \lambda_{\text{eff}}\sin(\theta/2)$. The coupling parameter is not only an important parameter that dictates how strongly the atomic dipole couples to each arm of the cross cavity, but also it allows defining the new field operators through $A = \cos(\theta/2)a + \sin(\theta/2)b$ and $B = -\sin(\theta/2)a + \cos(\theta/2)b$. The new field operators satisfy the algebra of two independent harmonic oscillators and the total number operator $a^\dagger a + b^\dagger b = A^\dagger A + B^\dagger B$ is preserved.

3 Quantum Superpositions in the Cross-Cavity

By rewriting the Hamiltonian in terms of A and B emerges a mathematical structure similar to the Jaynes-Cummings Hamiltonian, which allows us to describe the dynamics of the cross-cavity through the state:

$$\left|\psi(t)\right\rangle\rangle = \sum_{MN}\left[\phi_{MN,e}(t)\,|e\rangle\,|M,N\rangle\rangle + \phi_{MN,g}(t)\left|g\right\rangle\,|M+1,N\rangle\rangle\right]. \tag{3}$$

The analytical expression of the complex amplitudes $\phi_{MN,e}(t)$ and $\phi_{MN,g}(t)$ will be published elsewhere. A more interesting aspect of the state 3 is that it is given in terms of the two-quasi-mode Fock states (Denoted by double angle), they can be conveniently discussed in terms of the angular momentum formalism.

For that purpose, let us introduce the Schwinger rotation operator $S_y(\theta) = e^{-i\theta L_y}$ and the angular momentum operator $L_y = -i\left(a^\dagger b - b^\dagger a\right)/2$. By recognizing the equality $|0,0\rangle = |0,0\rangle\rangle$, the two-quasi-mode Fock states are obtained by a simple rotation $|M,N\rangle\rangle = S_y(\theta)\,|M,N\rangle$. Furthermore, the coefficients are obtained straightforwardly by:

$$\left|j,m\right\rangle\rangle = S_y(\theta)\left|j,m\right\rangle = \sum_{m'} d^j_{m',m}(\theta)\left|j,m'\right\rangle. \tag{4}$$

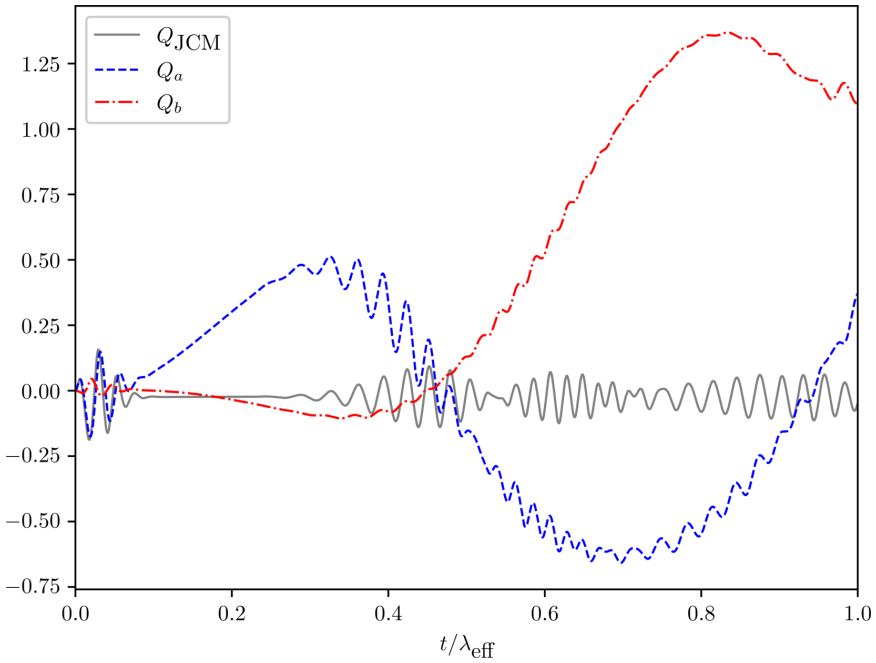

Fig. 1. Numerical computation of the Mandel parameter in the Jaynes-Cummings Model Q_{JCM} and in the horizontal Q_a and vertical Q_b arm of the cross-cavity. The initial state of the system is $|\alpha, 0, e\rangle$, with $|\alpha|^2 = 10$, and the coupling parameter is $\theta = \pi/4$. Notice that while the JCM predicts $Q_{\mathrm{JCM}} \sim -1/4|\alpha|^2$ in the regions between collapse and revival, the value of the Mandel parameter Q_a is considerably lower, i.e., it is considerabily more sub-Poissonian.

In Eq. 4 we identify the angular momentum states $\left|j, m\right\rangle$, with quantum numbers $j = (M+N)/2$ and $m = (M-N)/2$. Moreover, the coefficients of the expansion are the elements of the well known Wigner d-matrix $d^j_{m',m}(\theta) = \left\langle j, m'\right| S_y(\theta) \left|j, m\right\rangle$ [9]. According to Eq. 4, the transformed angular momentum can be interpreted as the superposition of angular momenta over all possible values of m, and a constant value of j.

The transformation that we introduced to define new field operators in the cross-cavity also can be found in the quantum mechanical theory of a lossless Beam Splitter (BS). The field at the output ports of the BS are related to the field at the input ports through a Schwinger transformation, and the photon statistics for notable inputs is well-known [1]. From the wave function, some important quantities can be analytically evaluated such as the atomic inversion and the average number of photons. Our previous research shows that collapses and revivals may occur in unforeseen cases by the JCM [5].

4 Sub-Poissonian Light and Photon Antibunching

To discuss the photon statistics of the field in the cross cavity, we compute numerically the Mandel parameter and the second-order normalized correlation function. These quantities are given by:

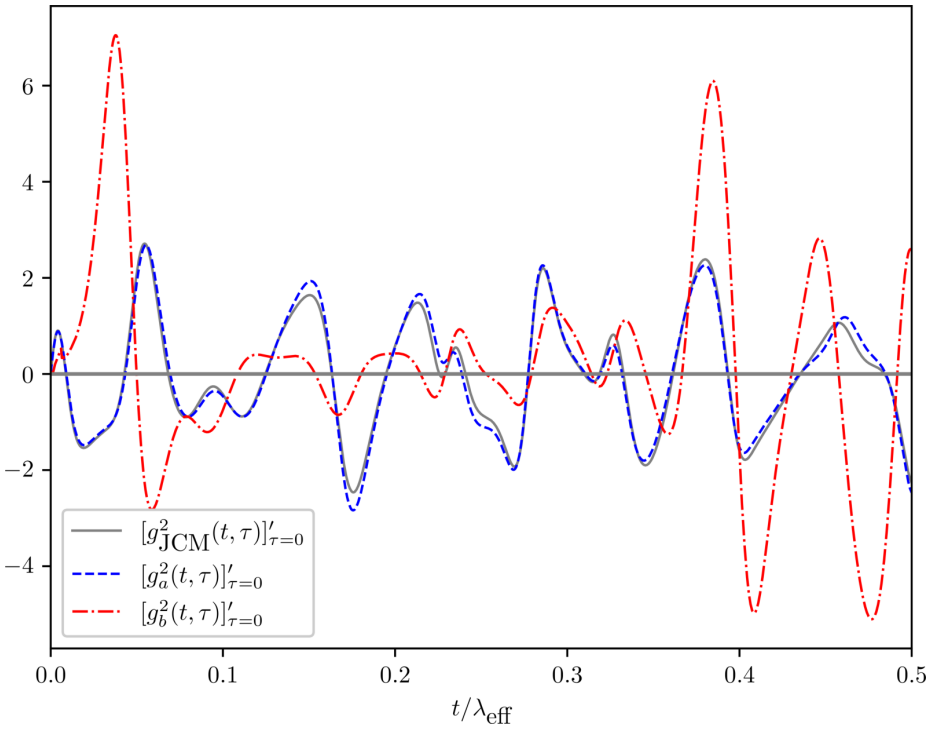

Fig. 2. Numerical computation of the derivative of the second-order correlation $g_O(t,\tau)$ as a function of τ in the Jaynes-Cummings Model and in the horizontal Q_a and vertical Q_b arm of the cross-cavity. The initial state of the system is $|\alpha,0,e\rangle$, with $|\alpha|^2 = 1$, and the coupling parameter is $\theta = \pi/8$. Notice that for this configuration, the antibunching properties of the JCM and the horizontal arm of the cross-cavity looks quite similar; on the other hand, there is a transference of photons towards the vertical arm with antibunching exhibiting an oscillatory behavior.

$$\begin{aligned} Q_O(t) &= \frac{\langle O^\dagger(t)\,O^\dagger(t)\,O(t)\,O(t)\rangle - \langle O^\dagger(t)\,O(t)\rangle^2}{\langle O^\dagger(t)\,O(t)\rangle}, \\ g^{(2)}_O(t,t+\tau) &= \frac{\langle O^\dagger(t)\,O^\dagger(t+\tau)\,O(t+\tau)\,O(t)\rangle}{\langle O^\dagger(t+\tau)\,O(t+\tau)\rangle\langle O^\dagger(t)\,O(t)\rangle}, \end{aligned} \tag{5}$$

where $O = a,\ b$. The numerical solutions were obtained withe the aid of the Python QuTiP Toolbox [7]. Let us recall that light whose photon number fluctuations are smaller than those of the Poisson distribution it is said sub-Poissonian and that a good measure of those fluctuations is the Q-parameter.

In figure 1, we show an striking numerical result of Mandel parameter in the cross cavity. Whereas the JCM predicts a value $Q_{\text{JCM}} \sim -1/4\bar{n}$ between collapse and revival ($\bar{n}$ indicates the average of the photon distribution), the cross-cavity produces Mandel parameters along x and y considerably more negative; however, it seems that there is no a quasi-steady behavior in the short-term regime.

Another interesting statistical feature of the light is the degree of second-order coherence, which plays a central role in the definition of photon-antibunching. A widely accepted definition of antibunching occurs when the derivative of the normalized function $g_O^{(2)}(t, t+\tau)$ as a function of the delay time τ at $\tau = 0$ is positive [3]. Our numerical simulation focuses on weak field $|\alpha|^2 = 1$, and the results are presented in the figure 2.

5 Conclusions

The cross-cavity configuration that we presented is a tripartite system that allows inquiring on quantum superposition effects unforeseen in the bipartite JCM.

Acknowledgments. Supported by Universidad Autónoma de Coahuila and by CONACyT through the scholarships assigned to L. Romero-Lira (CVU:1104357) and J. M. González-Vargas (CVU:972195).

References

1. Campos, R. A., Saleh, B. E. A., Teich, M. C.: Quantum-mechanical lossless beam splitter: SU(2) symmetry and photon statistics. Physical Review A, vol. 40, pp. 1371–1384 (1989) doi: 10.1103/PhysRevA.40.1371
2. Cummings, F. W.: Stimulated emission of radiation in a single mode. Physical Review, vol. 140, no. 4A, pp. A1051–A1056 (1965) doi: 10.1103/PhysRev.140.A1051
3. Dung, H. T., Shumovsky, A. S., Bogolubov, N. N.: Antibunching and sub-poissonian photon statistics in the Jaynes-Cummings model. Optics Communications, vol. 90, no. 4-6, pp. 322–328 (1992) doi: 10.1016/0030-4018(92)90285-y
4. Eberly, J. H., Narozhny, N. B., Sanchez-Mondragon, J. J.: Periodic spontaneous collapse and revival in a simple quantum model. Physical Review Letters, vol. 44, no. 20, pp. 1323–1326 (1980) doi: 10.1103/PhysRevLett.44.1323
5. Garcia-Melgarejo, J. C., Lozano-Crisostomo, N., Rodriguez-Montero, P., Sanchez-Mondragon, J. J.: Dynamics of a two-level atom in a double perpendicular cavity. Photonics Letters of Poland, vol. 7, no. 2, pp. 35–37 (2015) doi: 10.4302/photon.lett.pl.v7i2.553
6. Jaynes, E., Cummings, F.: Comparison of quantum and semiclassical radiation theories with application to the beam maser. In: Proceedings of the IEEE, vol. 51, pp. 89–109 (1963) doi: 10.1109/proc.1963.1664
7. Johansson, J. R., Nation, P. D., Franco, N.: QuTiP 2: A Python framework for the dynamics of open quantum systems. Computer Physics Communications, vol. 184, no. 4, pp. 1234–1240 (2013) doi: 10.1016/j.cpc.2012.11.019
8. Rempe, G., Walther, H., Klein, N.: Observation of quantum collapse and revival in a one-atom maser. Physical Review Letters, vol. 58, no. 4, pp. 353–356 (1987) doi: 10.1103/physrevlett.58.353
9. Wigner, E.: Group theory: And its application to the quantum mechanics of atomic spectra. Elsevier (1952)

ISSN 1870-4069

Characterization of Temperature-Induced Changes in Polarization-Maintaining Nonlinear Optical Fibers

Miguel A. Espiricueta-Ulloa[1], Javier Sánchez-Mondragón[2], Julio C. García-Melgarejo[1], Néstor Lozano-Crisóstomo[1]

[1] Universidad Autónoma de Coahuila, Facultad de Ingeniería Mecánica y Eléctrica, Mexico

[2] Instituto Nacional de Astrofísica, Óptica y Electrónica, Heroica Puebla de Zaragoza, Mexico

arturo_espiricueta@uadec.edu.mx

Abstract. We theoretically characterize the temperature-induced chan-ges in polarization-maintaining (PM) nonlinear optical fibers. Based on a linear model of the temperature-dependent birefringence, we compute the change of the output polarization state (PS) of light through the calculation of the Stokes parameters. Our treatment provides an important analysis for the implementation in nonlinear temperature sensors.

Keywords: Polarization-maintaining nonlinear optical fibers, temperature-dependent birefringence, nonlinear polarization conversion, optical fiber sensors.

1 Introduction

The theory for describing and controlling the nonlinear polarization conversion of circularly polarized (CP) light in nonlinear birefringent optical fibers (BOFs) (Low- and High-BOFs) is given in Ref. [4]. Through a nonlinear model, it was provided the conditions to obtain the most common continuous wave (CW) polarization states (PSs) at the BOF output. In that regard, all-optical nonlinear control of CP light was demonstrated by tailoring the nonlinear and birefringence fiber parameters.

Such results are very important because open new perspectives for all-optical fiber sensors and provide considerable physical insight on the all-optical polarization control with nonlinear BOFs. In this work, we characterize the temperature-induced changes in PM nonlinear optical fibers through the computing of the change of the output PS of light. For this purpose, we develop a theoretical model to show how the birefringence is affected by the temperature changes.

2 Temperature Sensing Mechanism

We begin by considering a CW CP light beam launched into a lossless PM fiber such that it excites the two orthogonally polarized modes.

The coupled-mode equations that describe the evolution of the two orthogonally polarized components are given by [1]:

$$\frac{\mathrm{d}U_x}{\mathrm{d}z} = i\frac{1}{L_{NL}}\left(|U_x|^2 + \frac{2}{3}|U_y|^2\right)U_x + i\frac{1}{3L_{NL}}U_x^* U_y^2 \mathrm{e}^{-i2\Delta\beta z}, \tag{1}$$

$$\frac{\mathrm{d}U_y}{\mathrm{d}z} = i\frac{1}{L_{NL}}\left(|U_y|^2 + \frac{2}{3}|U_x|^2)\right)U_y + i\frac{1}{3L_{NL}}U_y^* U_x^2 \mathrm{e}^{+i2\Delta\beta z}, \tag{2}$$

where $U_x(z)$ and $U_y(z)$ are the normalized slowly varying amplitudes of such orthogonal polarization components of the optical field. Here the factor $i = \sqrt{-1}$ represents the imaginary unit, z is the standard notation for the propagation distance, $L_{NL} = (\gamma P_0)^{-1}$ is the nonlinear length, P_0 is the input peak power, and γ is the nonlinear parameter.

The linear birefringence parameter is $\Delta\beta = 2\pi/L_B$, where $L_B = \lambda/B$ is the beat length, $B = |n_x - n_y|$ is the degree of modal birefringence, and λ is the wavelength of light. n_x and n_y are the effective refractive indices along the x- and y-polarization axes of the PM fiber, respectively. It is usually assumed that n_x along the x-polarization or slow axis is greater than n_y along the y-polarization or fast axis.

Solutions of Eqs. (1) and (2) can be given by the following matrix form representation which describes the evolution of the two normalized slowly varying amplitudes, $U_x(z)$ and $U_y(z)$, along a PM fiber [4]:

$$\begin{bmatrix} U_x(z) \\ U_y(z) \end{bmatrix} = \mathbf{M}(z) \begin{bmatrix} U_x(0) \\ U_y(0) \end{bmatrix}, \tag{3}$$

where $U_x(0)$ and $U_y(0)$ represent the normalized slowly varying amplitudes of the two orthogonally polarized modes of the input signal field. The propagation matrix $\mathbf{M}(z)$ given by:

$$\mathbf{M}(z) = \begin{bmatrix} t\, e^{i(\phi_{NL\pm} - \Delta\beta z/2)} & \pm\, i\, r\, e^{i(\phi_{NL\mp} - \Delta\beta z/2)} \\ \pm i\, r\, e^{i(\phi_{NL\mp} + \Delta\beta z/2)} & t\, e^{i(\phi_{NL\pm} + \Delta\beta z/2)} \end{bmatrix}. \tag{4}$$

Is satisfied when either right hand circular polarization (RHCP) or left hand circular polarization (LHCP) light is launched into the PM fiber. Here $\phi_{NL+}(z)$ and $\phi_{NL-}(z)$ are two nonlinear phase shifts, and $t(z) = \sqrt{1+u(z)}/\sqrt{2}$ and $r(z) = i\sqrt{1-u(z)}/\sqrt{2}$ are defined as the transmittance and reflectance, respectively. In general, before relations satisfy the conservation of energy conditions: $|t(z)|^2 + |r(z)|^2 = 1$ and $r(z)t^*(z) + t(z)r^*(z) = 0$. In Eq. (4), the upper and lower signs in $\pm$ and $\mp$ are considered to be associated with the RHCP and LHCP input light, respectively.

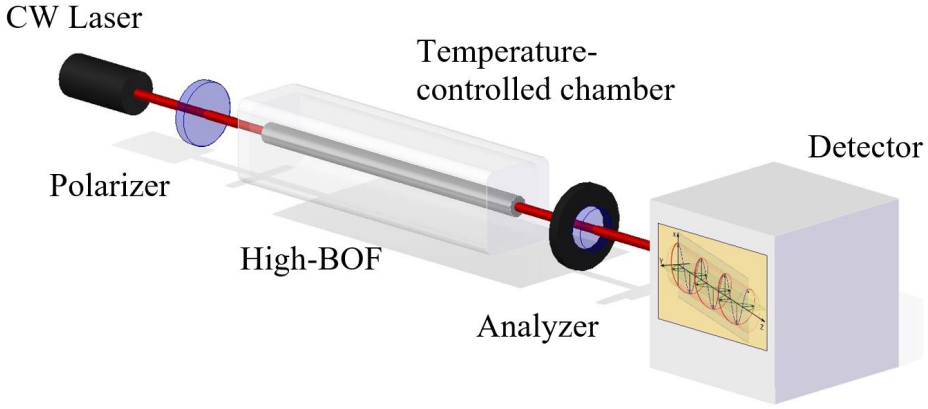

Fig. 1. A light beam traveling through a High-BOF (polarization-maintaining fiber) affected by a specific temperature, changing its physical proprieties and the polarization of light.

The $u(z)$, $\phi_{NL+}(z)$ and $\phi_{NL-}(z)$ functions are given by:

$$u = \text{cn}(\Delta\beta z|m), \tag{5}$$

$$\phi_{NL+}(z) = \frac{5}{6}z \mp \frac{1}{2}\arccos[\text{dn}(\Delta\beta z|m)], \tag{6}$$

$$\phi_{NL-}(z) = \frac{5}{6}z \pm \frac{1}{2}\arccos[\text{dn}(\Delta\beta z|m)], \tag{7}$$

where $\text{cn}(x|m)$ and $\text{dn}(x|m)$ are two Jacobi elliptic functions with argument x and modulus $m = k^2$. For any elliptic function, its modulus must lie between 0 and 1. In our case, the modulus $m = [\gamma P_0/(3\Delta\beta)]^2$; and therefore, $k = \gamma P_0/(3\Delta\beta)$.

2.1 Methodological Strategy

Power variations of the propagating light and physical parameters, such as temperature, stress, magnetic field, and torsion affect the birefringence of an optical fiber. Thereby some analytical models that relate such physical parameters with the birefringence of optical fibers have been developed [2, 3, 5].

In that regard, such intuitive relations can be used to implement such theoretical model [4] and develop high-sensitivity all-optical fiber sensors and new sensing methods that allow obtaining magnitudes of parameters more accurately. For our purposes, we implement the following approach given by [2, 5]:

$$B = B_0 + \gamma_b(T + T_0), \tag{8}$$

where T is the temperature of the fiber under test, T_0 is the room temperature, B_0 is the birefringence at room temperature, and γ_b is the thermal coefficient, which relates the birefringence with temperature in High-BOFs. Therefore, we can use such relation and introduce it in the developed theoretical model through the definition of the beat length given by $l_B = \lambda/B$.

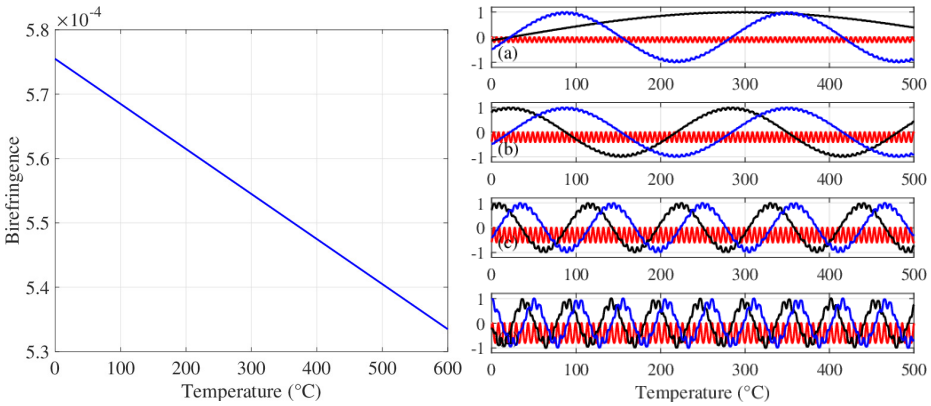

Fig. 2. The graph on the left shows the behavior of fiber's birefringence with increasing temperature, and the graph on the right shows how the Stokes parameters change as the temperature increases. S_1 (red solid line), S_2 (black solid line,) and S_3 (blue solid line). Output Stokes parameters for a High-BOF length $L = 2\,\mathrm{m}$, $\lambda = 1550\,\mathrm{nm}$, $\gamma_b = -7x10^{-8}\ °\mathrm{C}^{-1}$, $T_0 = 20\ °\mathrm{C}$, and $B_0 = 5.74x10^{-4}$ [3, 5]. Normalized input power for (a) $P_0/P_c = 0.2$, (b) $P_0/P_c = 0.4$, (c) $P_0/P_c = 0.6$ and (d) $P_0/P_c = 0.8$, when a right-handed circularly polarized light is launched into the PM fiber.

In this way, we can apply the theoretical model to analyze how the temperature affects the output polarization in optical fibers. For this purpose, the change of the output PS of initially CW CP light must be monitored after its transmission through a PM fiber.

3 Results

Using Eq. (8), it is possible to calculate the birefringence changes of the High-BOF due to the temperature increments or decrements. Therefore, applying the theory given in [4] and using Eq. (8), we obtain theoretically how the temperature changes affect the Stokes parameters of the output polarized light.

4 Conclusions

We have described and characterize theoretically the temperature-induced chan-ges in PM nonlinear optical fibers through the computing of the change of the output PS of light. We have developed a theoretical model to show how the birefringence is affected by the temperature changes. Our study creates a new possible way to measure temperature utilizing this kind of fibers that we know they are a good option because their properties.

Acknowledgments. M. A. Espiricueta-Ulloa, N. Lozano-Crisóstomo and J. C. García-Melgarejo thank to the UAdeC for its amazing support.

References

1. Agrawal, G. P.: Nonlinear fiber optics. In: Christiansen, P. L., Sørensen, M. P., Scott, A. C. (eds) Nonlinear Science at the Dawn of the 21st Century. Lecture Notes in Physics, Springer, Berlin, Heidelberg, Academic Press, vol. 542 (2000) doi: 10.1007/3-540-46629-09
2. Ding, Z., Meng, Z., Yao, X. S., Chen, X., Liu, T., Qin, M.: Accurate method for measuring the thermal coefficient of group birefringence of polarization-maintaining fibers. Optics Letters, vol. 36, no. 11, pp. 2173–2175 (2011) doi: 10.1364/ol.36.002173
3. Kim, D. H.: Analysis of temperature-dependent birefringence of a polarization-maintaining photonic crystal fiber. Optical Engineering, vol. 46, no. 7, pp. 75003 (2007) doi: 10.1117/1.2752177
4. Lozano-Crisóstomo, N., García-Melgarejo, J. C., González-Galicia, M. A., Baez-López, C. A., Hurtado-Carrazco, J. C., Sánchez-Mondragón, J. J.: All-optical nonlinear control of circularly polarized light in birefringent fiber. Journal of Lightwave Technology, vol. 39, no. 15, pp. 5118–5125 (2021) doi: 10.1109/JLT.2021.3082105
5. Thorlabs: Designer and manufacturer of photonics equipment for research (2021) www.thorlabs.com/navigation.cfm

ISSN 1870-4069

Propagation in Linear Arrangements of Optical Antennas with Non-Uniform Separation

Alejandro Padrón-Godínez, Venancio Gerardo Calva Olmos

Universidad Nacional Autónoma de México,
Instituto de Ciencias Aplicadas y Tecnología,
México

alejandro.padron@icat.unam.mx

Abstract. In this work, the propagation in linear arrays of optical antennas with non-uniform separation by directional resonators for the coupling of light waves on one element to another is presented. The dependence of the element coupling factor on the spacing can control the amount of coupling between the elements of the optical antenna. The electromagnetic radiation that propagates through the dielectric elements of the optical antenna has greater intensity concentrated within the cores and the electric field decays exponentially outside of the elements with distance. The medium where these dielectric elements of the antenna are immersed acts as the coating as cladding in the case of wave guides. The following separation distributions were used: uniform, geometric, sinusoidal, binomial, and Tschebysheff polynomial. Each of them with five elements and a wavelength $\lambda = 1550$ nm was used, which correspond to one of the intervals for optical communications, with a dielectric constant of $\varepsilon = 13.9876$ ($\cong$ GaAs), each element has a diameter of $d = 6.76$ μm and a spread of 4.2 mm along the z axis, the dielectric constant of the coating or cladding is 0.5% smaller than antenna elements.

Keywords: Optical antennas, coupling, non-uniform separation.

1 Introduction

The electromagnetic radiation that propagates through the dielectric elements of the optical antenna has greater intensity concentrated within the cores and the electric field decays exponentially outside of the elements with distance. The medium where these dielectric elements of the antenna are immersed acts as the coating, that´s it as cladding in the case of waveguides. The perturbances in the resonance modes of the antenna elements are produced by the proximity of the other elements.

The variation of the dielectric constants of the elements of the optical antenna is another way to control the amount of coupling between the resonators. The appearance of super modes oscillations shows that they are a solution to the propagation equation and when an element is perturbed, it propagates towards the other elements, but if more than one element of the antenna is perturbed, the modes may have destructive superposition. In the work, we analyze the relationship of the propagation

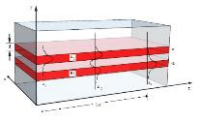

Fig. 1. Coupling between two flat waveguides.

optical antenna with the currents distribution in a radio frequency antenna through the Moment Method (MM).

2 Couplers Modes and Moment Methodology to Linear Arrays

2.1 Couplers Modes

Two optical devices that propagate radiation by approach can produce coupling phenomena; however, this can also occur if two similar waveguides are very close together, as in the case of coupled pendulums. With this, if you now have two waveguides very close to each other, in such a way that they exchange fields from one side to the other (electromagnetic radiation), the incident radiation will be able to propagate through the coupling of these guides. In other words, we can see that optical irradiance can be transfered between waveguides; we can take advantage of this phenomenon for the design and construction of optical couplers that can serve as switches or multiplexers.

To study this work case, there are five elements in the linear array and the coupling is governed by the sum of all the electric fields, that is:

$$E(r) = E_1 \exp(-\beta_1 z) + E_2 \exp(-\beta_2 z) + E_3 \exp(-\beta_3 z) + E_4 \exp(-\beta_4 z) + E_5 \exp(-\beta_5 z) \cdot \quad (1)$$

And the coupling of the arrangement can be expressed as:

$$\frac{dE(z)}{dz} = i \begin{pmatrix} n_1 & \alpha_{12} & 0 & 0 & 0 \\ \alpha_{21} & n_2 & \beta_{23} & 0 & 0 \\ 0 & \beta_{32} & n_3 & \gamma_{34} & 0 \\ 0 & 0 & \gamma_{43} & n_4 & \delta_{45} \\ 0 & 0 & 0 & \delta_{54} & n_5 \end{pmatrix} \begin{bmatrix} E_1(z) \\ E_2(z) \\ E_3(z) \\ E_4(z) \\ E_5(z) \end{bmatrix}, \quad (2)$$

where the refractive indexes of each element are $n_1=n_2=n_3=n_4=n_5=n$ and that α, β, γ, δ are the coupling coefficients, which would be the same if they were not dependent on the separation between each element array.

2.2 Moment Method

The moment method is a tool for the study of the operating properties of a linear arrangement of the resonator elements that make up an antenna [1]. The procedure for the currents approximation consists initially in dividing the conductor into a number N of segments, which may or may not have the same length. Each segment has its intrinsical impedance and a mutual impedance in each pair of them. The relationship of

voltage, current and mutual impedance of the segments in matrix form is represented by:

$$\begin{array}{l} V_1(z) = I_1 Z_{11} + I_2 Z_{12} \\ V_2(z) = I_1 Z_{21} + I_2 Z_{22} + I_3 Z_{23} \\ V_3(z) = I_2 Z_{32} + I_3 Z_{33} + I_4 Z_{34} \\ V_4(z) = I_3 Z_1 + I_4 Z_{44} + I_5 Z_{45} \\ V_5(z) = I_4 Z_{54} + I_5 Z_{55} \end{array} \quad , \; o \;\; bien \; V(z) = \begin{pmatrix} Z_{11} & Z_{12} & 0 & 0 & 0 \\ Z_{21} & Z_{22} & Z_{23} & 0 & 0 \\ 0 & Z_{32} & Z_{33} & Z_{34} & 0 \\ 0 & 0 & Z_{43} & Z_{44} & Z_{45} \\ 0 & 0 & 0 & Z_{54} & Z_{55} \end{pmatrix} \begin{bmatrix} I_1 \\ I_2 \\ I_3 \\ I_4 \\ I_5 \end{bmatrix}, \tag{3}$$

where ***[V]*** is the voltage matrix, ***[I]*** is the current matrix, both are arrays of MxN elements and ***[Z]*** is the antenna impedance matrix. The matrix ***[V]*** is formed by the feeding points of the antenna, namely if the antenna is power in a single point. If ***[V]*** and ***[Z]*** are known, it is possible to find the currents distribution ***[I]***. From equation (3) we have:

$$[I] = [Z]^{-1}[V], \tag{4}$$

where $[Z]^{-1}$ is an admittance matrix.

2.3 Linear Arrays with Non-Uniform Separation

The spacing configurations of antennas linear arrays with separation considered here are uniform and non-uniform geometric, sinusoidal, binomial and Tschebysheff. It also is considered an array of five elements (antennas) and a wavelength λ=1,5.

The current distribution is obtained according to the MM, for each spacing configuration [2-6]. If it is considered the geometric series $a+ar+ar^2+ar^3+ \ldots + ar^{n-1}$ and taking at elements of sum as distances between each antenna, with a=1 and r=2, then the configuration of Fig. (2a and 2b) is obtained. Now it is taking five elements array, with separation of 1, 2, 4, 8 and a wavelength λ=1,5 the current distribution is obtained according to the MM.

For this array an evaluation of the sine trigonometrical function is made according to a sampling that it assists at division of 90º among the number of antennas array and with this the spacing between them is obtained as the Fig. (2c and 2d) it shows. Now if it is considered an array of five elements, with spacing of 1, 0.92, 0.7, 0.38 and a wavelength λ = 1.5 the current distribution is obtained according to the MM. In order to determine the configuration of a binomial array, it suggested that the function $(1+x)^{m-1}$ be written in a series, using the binomial expansion, as:

$$(1+x)^{m-1} = 1 + (m-1)x + \frac{(m-1)(m-2)}{2!}x^2 + \frac{(m-1)(m-2)(m-3)}{3!}x^3 + \ldots \tag{5}$$

For different values of m the results of series expansion give it the spacing configurations showed in Fig. (2e and 2f), this figure represents Pascal's triangle. If the values of *m* are used to represent the number of elements of the array, then the coefficients of the expansion represent the relative amplitudes of elements.

Taking *m*=5, it is had five elements array, with separation of 1, 3, 3, 1 and taking a wavelength λ=1.5 the current distribution is obtained according to the MM. In order to find the spacing of this configuration it is used de Euler's formula, in other words the distances between elements array. Since:

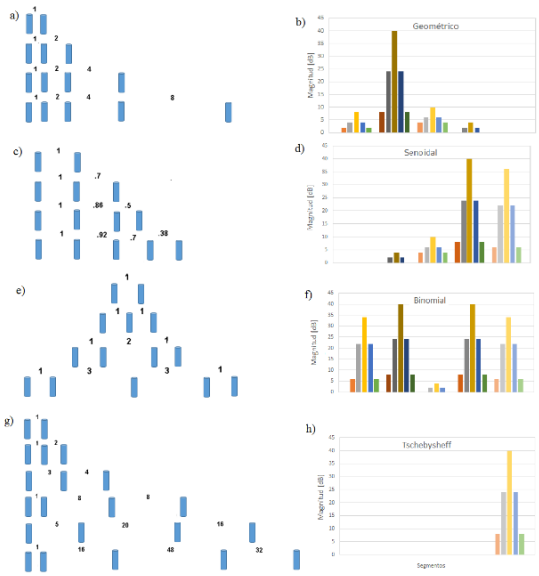

Fig. 2. Geometric spacing (left) and current distribution for 5-elements array (right).

$$[e^{ju}]^m = (\cos u + jsinu)^m = e^{jmu} = \cos(mu) + jsin(mu)\,. \tag{6}$$

Using the trigonometric identity $sin^2\ u=1\ -\ cos^2\ u$, and with $z\ =\ cos\ u$, the Tschebyscheff configuration is given as:

$$T_0(z) = 1,$$

$$T_1(z) = z,$$

$$T_2(z) = 2z^2 - 1\ ,$$

$$T_3(z) = 4z^3 - 3z,$$

$$T_4(z) = 8z^4 - 8z^2 + 1,$$

$$T_5(z) = 16z^5 - 20z^3 + 5z,$$

$$T_6(z) = 32z^6 - 48z^4 + 18z^2 - 1,$$

$$T_7(z) = 64z^7 - 112z^5 + 56z^3 - 7z.$$

And each is related to Tschebyscheff polynomial $T_m(z)$, according to this the spacing array is shown in the Fig. (2g and 2h). If it is considered an array of five elements, with spacing of 1, 16, 48, 32 and a wavelength $\lambda\ =\ 1{,}5$ the current distribution is obtained according to the MM.

3 Results

The results that are presented is when in each arrangement of five linear resonators the electric field propagation is made along the z axis, by means finite element simulation with separation according to how the distribution of currents in the linear arrangements

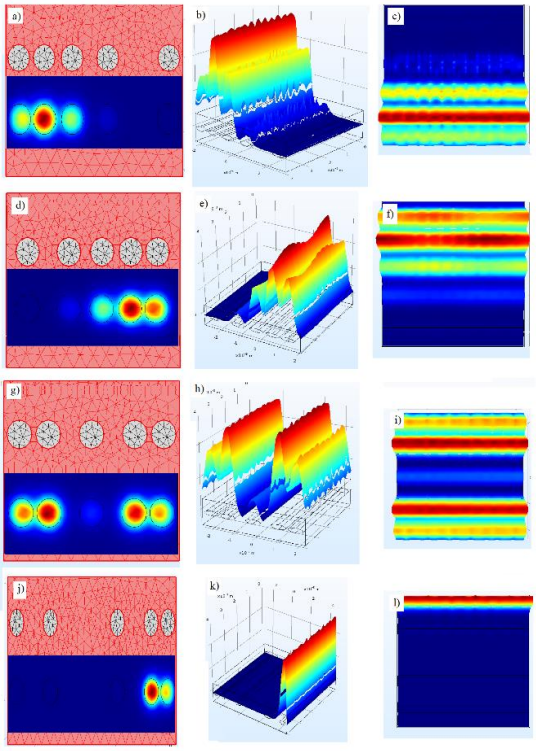

Fig. 3. Linear array of five elements with a) geometric, d) sinusoidal, g) binomial and j) Tschebysheff separation, b), e), h), k) propagation on optical antenna and c), f), i) l) modes of propagation.

was obtained. Recall that we use antenna elements with 6,76 μm of diameter, a wavelength of λ = 1550 nm, along 4.2 mm propagation distance, refractive indexes n_{cladd} = 3,74 in the coating and n_{ker} = 3,745 in the elements of GaAs.The displacements are multiples of a distance d = 3,88 μm according to uniform, geometric, sinusoidal, binomial and polynomial arrangement of Tschebysheff separation.

The radiation propagation over a five elements array with non-uniform spacing Fig. (3a), shows the non-uniform geometric separation, we observe here that the separation (1, 2, 4, 8) for five elements decouples the distant elements and there is only propagation in the nearby (1, 2, 3) elements. Fig. (3d), illustrates the sinusoidal separation, with a separation of (1; 0.92; 0.7; 0.38) for five elements, in this case there is decouples on first elements and there is a bit coupling in 4 and 5 elements on high amplitudes.

Fig. (3g), shows the binomial separation, with a separation of (1; 3; 3; 1) for five elements. Here there is little coupling in (1, 2) and (4, 5) elements, while in 3 element it propagates with lower amplitude than others as channel separation. Fig. (3j), shows the Tschebysheff polynomial separation, with a separation of (1; 16; 48; 32) for five elements. In this case, the (1, 2, 3, 4) elements are completely without propagation, zero amplitude and propagation is only observed in 5 elements of the linear array.

4 Conclusions

We have shown the obtaining of distribution currents for five elements with different arrangements with uniform and non-uniform separation by the method of moments.

We have also shown the radiation propagation in the elements of optical antenna for the same non-uniform separations of the linear arrays, using the finite element method. Both methods show some analogy between the coupling coefficients and the measurement of the own and mutual impedances, where the solutions to the analytical models are similar.

This can be observed in the forms of the propagations and the current distributions in the different analyzed arrangements. On the other hand, the graphs of the radiation propagation obtained by the EFM can show the resonance amplitudes along the *z*-axis, the separation between the elements and if there are coupled modes.

Further, the analogy between the methods occurs at the beginning of propagation by FEM. The wavelength for optical communications in 1,5 μm, leaves us, in perspective, the motivation to work with optical antennas resonators in biometric recognition sensors, opto-electrical switches and light multiplexers to mention a few topics.

References

1. Neri-Vela, R.: Análisis de antenas lineales por el método de momentos. Ingeniería Investigación y Tecnología. vol. 1, no. 2, pp. 73–83 (1999) doi: 10.22201/fi.25940732e. 1999.01n2.009
2. Padrón, A., Garduño, J. I., Herrera, A., Prieto, R.: Antennas array adjust with adaptive neuronal system. Journal of Applied Research and Technology, vol. 2 no. 3. pp. 189–198 (2004)
3. Padrón, A., Garduño, J. I.: Current distribution interpolation for antennas linear arrays with nonuniform spacing. Instrumentation & Development. vol. 5, no. 2, pp. 74–82 (2001)
4. Balanis, C. A.: Antenna theory analysis and design. New York: John Wiley & Sons, Inc., (1997)
5. Garduño, J. I. Padrón. A.: Análisis de antenas lineales empleando redes neuronales artificiales. X Congreso Internacional de Electrónica, Comunicaciones y Computadoras, CONIELECOMP´00, pp. 393–397 (2000)

ISSN 1870-4069

Corneal Topography Using a Null-Screen Target in a Quadrangular Prism Configuration

Martín Isaías Rodríguez-Rodríguez[1], A. Abril Suarez-Ajoleza[1], Daniel Aguirre-Aguirre[2], Dulce González-Utrera[2], Rufino Díaz-Uribe[2], Allesaandra Carmichael-Martins[3], Brian Vohnsen[4], Óscar Antonio Ramos-Montes[1]

[1] Universidad Nacional Autónoma de México, Facultad de Estudios Superiores Iztacala, Mexico

[2] Universidad Nacional Autónoma de México, Instituto de Ciencias Aplicadas y Tecnología, Mexico

[3] Indiana University School of Optometry, Ireland

[4] University College Dublin, Advanced Optical Imaging Group, School of Physics, Ireland

martin.isaias.rodriguez@iztacala.unam.mx

Abstract. In previous works, three reflective calibration spheres of different radius of curvature (7.7 mm, 9.42 mm, and 6.20 mm) were evaluated using an experimental setup based on specular reflection. To build this system; we use four identical null-screens into a quadrangular acrylic prism. The aim of this work is to show that the same setup is suitable as a corneal topographer instead of the traditional commercial topographers based in Placido disk. To achieve this purpose, experimental images of a volunteer´s cornea were obtained from the reflection of an adaptable Hartmann-pattern. With the experimental parameters of the elements involved in the setup and the spot centroid data obtained by image processing, the local normals of the surface at sampled points were found. Accurate reconstruction of the surface shape of a human cornea is obtained by numerical integration of the normals. By fitting the recovered data to a spherical model, the corresponding elevation map and radius of curvature 7.84 mm were found. This is the first report of the evaluation of a corneal surface using a null-screen target in a quadrangular prism configuration.

Keywords: Null-Screens, Hartmann-pattern, numeric integration method, corneal topography.

1 Introduction

It is well known that the anterior corneal surface provides about three-quarters parts of the total dioptric power of the human eye. On the other hand, refractive corrections and monitoring of corneal ectasias and keratoconus are all measured by corneal topography. Thus, quantifying corneal parameters such as radius of curvature, refractive power and elevation maps are of great research value and essential for vision and diagnostics.

The studies about corneal topography have typically made use of a Placido disc or Scheimpflug ophthalmology [1]. However, a possible limitation of Placido system due to data ambiguity in azimuthal direction was reported in 1998 by Schwiegerling et al. [2], what's more; "Axial curvature and the skew ray error in corneal topography" was reported in 1997 by S.A. Klein [3-4].

Consequently, new generations of topographers were developed making use of different principles with a geometrical pattern of spots printed on null-screens and in a modified Hartmann test to measure corneal topography [5-7]. These recent advances have been successful in testing, because modifying the geometry it can overcome the skew ray error.

The null-screen method has been used to test different types of optical surfaces as; spherical, aspherical fast convex and recently freeform surfaces [5-9]. For this reason, we have been working on a method for testing the corneal surface with four flat null-screens in a quadrangular prism setup, based on the null-screen principles.

In a previous work, we have demonstrated quantitatively that three reflective calibration spheres of different radius of curvature; 7.7 mm, 9.42 mm, and 6.20 mm can be evaluated using the same experimental setup based on specular reflection [10]. This work aims to show that the same setup is suitable as a corneal topographer.

In Section 2, the proposed method is briefly described; then, the design parameters of the null-screen are shown and the experimental setup is fully explained in Sections 3 and 4, respectively. Later, in Section 5, experimental results of the corneal surface reconstruction of a human volunteer are presented. Finally, the conclusions are presented in Section 6.

2 Proposed Setup and Method

As mentioned before, we use four identical null-screens type Hartmann into a quadrangular acrylic prism. The corneal surface of a human volunteer is placed just in

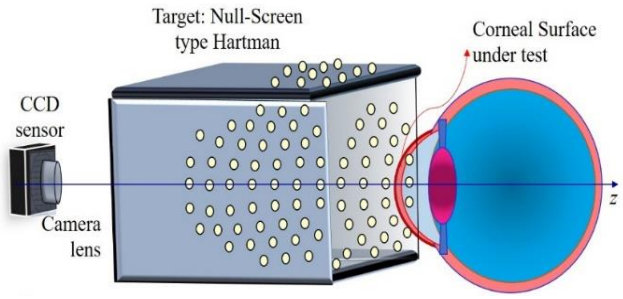

Fig. 1. Schematic setup of a quadrangular prism configuration [10].

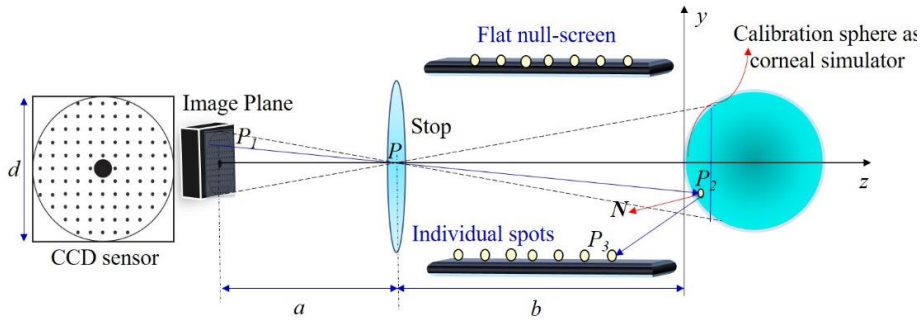

Fig. 2. Variables involved in the calculation of flat null-screen.

front of the quadrangular prism, as shown in Fig. 1. The essential idea consists of designing an array of null screens with a set of spots in such a way that the image reflected by the corneal surface gives a perfectly ordered arrangement type Hartmann, if the test surface is perfect.

Null-screen testing has the advantage that this technique does not need any additional optical element with a specific design to correct the aberrations of the system under test and the spots of the screen can be easily computed [8].

3 Parameters to the Design of Flat Null-Screen

To determine the points on the null-screen belonging to a square array of spots on the CCD sensor, we performed a reverse exact ray-tracing calculation, similarly as they have been obtained in previous work [6]; we use the same expression to get z_3, the calculation only differs in the use of four flat null-screens (parallel to the x and y axes), instead of three.

In null-screen method is used to find the coordinates of the points on screen $P_3=(x_3, y_3, z_3)$ that yield a perfect square array on the CCD; then, we start at the CCD plane. The variables involved in the design of the flat null-screen are shown in Fig. 2; in addition, a calibration sphere is placed as a corneal simulator.

The point $P_1=(x_1, y_1,-a-b)$ and the point $P_2=(x_2, y_2, z_2)$ are the cartesian coordinates on the CCD sensor and in the optical surface respectively, *a* and *b* are distances obtained by the *Gauss thin lens equation* and by the *magnification of the lens used*, these equations can be seen in detail in ref. [6]. The parameters *a* and *b* can be recalculated using the proposal developed by Aguirre-Aguirre et al., ref. [11]. The numerical values of the parameters used in this case are shown in Table 1.

4 Experimental Setup

To build the practical system, we used four identical flat screens, their dimensions are: 260 mm (height) × 180 mm (width) per side correspondingly. The screens were put side by side to form a quadrangular prism. To classify each null-screen-colored marking

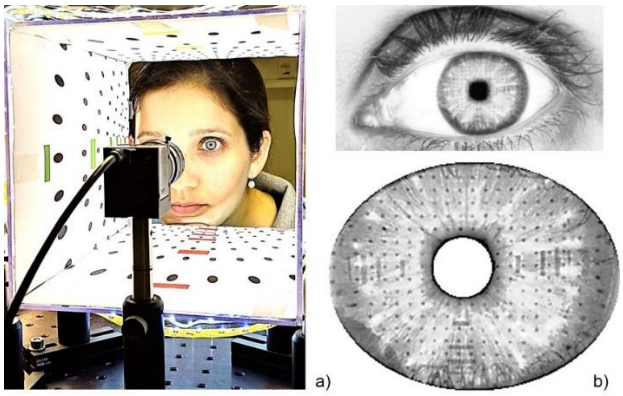

Fig. 3. (a) Experimental setup of corneal Topographer, (b) Detail of the reflected pattern.

Table 1. Parameters used for calculating the coordinates of flat null-screens.

Element	**Description**	**Symbol**	**Value (*mm*)**
CCD sensor	Thorlabs Model (**DCU223M**)	*d*	3.6 active area
Camera lens	Thorlabs Model (**MVL25M23**)	*f*	25
Parameter	Distance between CCD sensor and camera lens	*a*	29.61
Parameter	Distance between vertex surface and camera lens	*b*	266.07

(R, G, B and Y) have been designed, which, help to distinguish each side of null-screens inserted in the rectangular prism.

As a proof of this principle, Fig. 3. (a) shows a low-cost experimental setup based on specular reflection. The image of the light reflected by the human cornea is nearly seen as a square array of dots captured by the CCD sensor, as is shown in Fig. 3. (b). The reflection of the adaptable Hartmann pattern provides data allowing accurate reconstruction of the surface profile of the corneal surface.

It can be seen that at some points of the null-screen, we paint strategic marks of color following the next basic rules: Six colored spots are set along the *x*-axis, while six spots are positioned along the *y*-axis. For example, in Fig. 3 (a), we can see six red spots in the experimental setup along the *z*-axis, just to be redundant, in the orthogonal side, it is easy to see six green spots along the *z*-axis. This set of colored spots allows relating "*x*" and "*y*" directions on the screens even if one-or two-colored spots are missing.

Due to the sticking of null-screens on edges of the square prism some spots on the image are missing; that, complicates the final correspondence between centroids and coordinates of the null-screens. For this, the same reference color marks designed in null-screens (R, G, B and Y) helps to the correspondence during the quantitative evaluation of optical surfaces [Fig. 3. (b)].

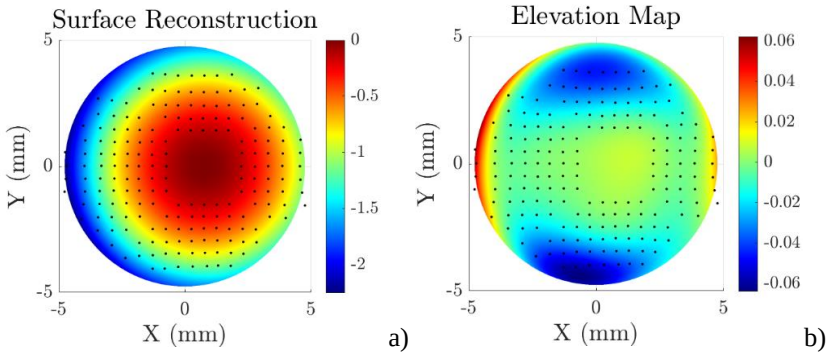

Fig. 4. Results: a) Shape surface reconstruction obtained by Zonal integration method, b) Elevation Color Map represented by Zernike standard Polynomial, (in mm units).

Zonal Integration

Having the information of the positions of the centroids and the knowledge coordinate to the flat null-screens, normal components to the surface are calculated, according to procedures proposed in [5-6, 9-11]. To evaluate the normals ***N***, to the test surface, we perform a three-dimensional ray trace procedure, which consists of finding directions of the rays that join actual positions, P_1, of centroids of the experimental image, and the corresponding coordinates P_3 of null-screen. According to reflection law, normal ***N*** to the test surface can be evaluated as:

$$N = \frac{R - I}{|R - I|}, \tag{1}$$

where ***I*** and ***R*** are the directions of the incident and reflected rays on the surface, respectively. The direction of the reflected ray ***R*** is known because after reflection on the test surface it passes through the center of the lens stop at ***P*** and arrives at the CCD image plane at $\boldsymbol{P}_1$, so that, we have two points along this ray, which are enough to know its direction (see Fig. 2).

In contrast, for incident ray ***I***, we know only the point $\boldsymbol{P}_3$ at null-screen, so, we need to have an approximate second point to obtain the direction of the incident ray; this is done by intersecting the reflected ray with a *reference surface*.

The shape of the surface is obtained by using the equation originally proposed by Díaz-Uribe [12] and first used in [8]:

$$z - z_1 = \int_{\wp(x_1, y_1)}^{(x,y)} \left[\frac{N_x}{N_z} dx + \frac{N_y}{N_z} dy \right], \tag{2}$$

where; $\boldsymbol{N}_x$, $\boldsymbol{N}_y$, and $\boldsymbol{N}_z$ are the cartesian components of the normal vector, C is the integration path, z_1 is the initial point in the integration path. Eq. (2) is exact, evaluating normals and performing the numerical integration, however, are approximate, so they introduce some errors that must be reduced. Thus, the errors involved during the determination of the normals are minimal if the reference surface differs only slightly from the test surface.

Table 2. Principal Coefficients of the Zernike Standard Polynomial**.**

Zernike Standard Polynomial	Coefficient (μm)	Zernike Standard Polynomial	Coefficient (μm)
Vertical Astigmatism (Z_6)	14.0357	Vertical Coma (Z_7)	5.4472
Primary Spherical (Z_{11})	7.4266	Horizontal Coma (Z_8)	-3.2004

The numerical evaluation of Eq. (3) can be performed by zonal or modal procedures. A simple zonal evaluation of the integral is the trapezoidal rule for nonequally spaced data [12-13], as:

$$z_M = -\sum_{i=1}^{M-1}\left\{\left(\frac{N_{x_i}}{N_{z_i}}+\frac{N_{x_{i+1}}}{N_{z_{i+1}}}\right)\left(\frac{x_{i+1}-x_i}{2}\right)+\left(\frac{N_{y_i}}{N_{z_i}}+\frac{N_{y_{i+1}}}{N_{z_{i+1}}}\right)\left(\frac{y_{i+1}-y_i}{2}\right)+z_0\right\}, \quad (3)$$

where M is the number of points along some integration path.

Consequently, the integration obtained with Eq. (3) and different paths covering all the centroids, the spatial position of every incidence point on the surface is obtained, and the shape surface equation is calculated as described in Refs. [5, 6].

5 Experimental Results

Corneal surface reconstruction obtained by the zonal integration method is shown in Fig 4(a). In addition, we obtained the elevation map (Fig. 4(b)) by taking the differences between the best spherical model and the data obtained by zonal integration. The differences were fitted into a Zernike standard polynomial with 37 terms [14].

In this first evaluation, we found that the radius of curvature of the best fitted sphere was $r_c = 7.84\ mm$. Analyzing the elevation color map, the peak-valley (P–V) value in sagitta differences is $\delta z_{p-v} = 120\mu m$, while the *RMS* value is $\delta z_{rms} = 18\ \mu m$. Table 2 lists the dominating Zernike components from the best fitted sphere. Results show that the dominated component is vertical astigmatism (Z_6).

6 Conclusions

In this paper, a quadrangular prism configuration based on null-screens has been proposed. This aimed at the measurement of corneal topography, so experimental results obtained for a human corneal have been presented.

The radius of curvature becomes closer to the real value; on the other hand, the RMS difference in sagitta which represent the elevation color map is within the range of commercial topographers, with $\delta z_{RMS} = 18\ mm$. Finally, we notice that the dominating components of the Zernike standard polynomials are Astigmatism (Z_6, Z_8), Primary Spherical (Z_{11}), Vertical Coma (Z_7) and Horizontal Coma (Z_8). The results obtained do not represent a fundamental limit; they can be improved with better alignment of the quadrangular setup of the surface or by improving the numerical routines.

Acknowledgment. The corresponding author thanks to the projects DGAPA-PAPIIT: TA101620, IT100321, IT102520, IA106823, IT103823N and IT100321, Dulce Gonzalez-Utrera acknowledges to postdoctoral research grant from CONACyT México.

References

1. Rand, R., Applegate, R. A., Howland, H. C.: A mathematical model of Placido disk keratometer and its implication for recovery of corneal topography. In Vision Science and its Applications, Technical Digest Series: Optical Society of America (1997) doi: 10.1364/VSIA.1997.FC.4
2. Schwiegerling, J., Miller, J. M.: A videokeratoscope using a distorted checkerboard target. Oral presentation at the Vision Science and Its Applications (OSA) Annual Meeting (1998) doi: 10.1364/VSIA.1998.MA.4
3. Klein, S. A.: Axial curvature and the skew ray error in corneal topography. Optometry and Vision Science: Official Publication of the American Academy of Optometry, vol. 74, pp. 931–994 (1997) doi: 10.1097/00006324-199711000-00027
4. Klein, S. A.: Corneal topography reconstruction algorithm that avoids the skew ray ambiguity and the skew error. Optometry and Vision Science: Official Publication of the American Academy of Optometry, vol. 74, pp 945–962 (1997) doi: 10.1097/00006324-199711000-00028
5. Campos-García, M., Cossio-Guerrero, C., Moreno-Oliva, V. I., Huerta-Carranza, O.: Surface shape evaluation with a corneal topographer based on a conical null-screen with a novel radial point distribution. Applied Optics, vol. 54, no. 17, pp. 5411–5419 (2015) doi: 10.1364/AO.54.005411
6. Rodriguez-Rodríguez, M. I., Jaramillo-Nuñez, A., Díaz-Uribe, R.: Dynamic point shifting with null screen using three LCDs as targets for corneal topography. Applied Optics, vol. 54, no. 22, pp. 6698–6710 (2015) doi: 10.1364/AO.54.006698
7. Mejía-Barbosa, Y., Malacara-Hernández, D.: Object surface for applying a modified Hartmann test to measure corneal topography. Applied Optics, vol. 40, no. 31, pp. 5778–5786 (2001) doi: 10.1364/AO.40.005778
8. Díaz-Uribe, R., Campos-García, M.: Null-screen testing of fast convex aspheric surfaces. Applied Optics, vol. 39, no. 16, pp. 2670–2677 (2000) doi: 10.1364/AO.39.002670
9. Gonzalez-Utrera, D., Aguirre-Aguirre, D., Rodríguez-Rodríguez, M. I., Díaz-Uribe, R.: Null-screen testing of the complementary freeform surfaces of an adjustable focus lens. Optics Express, vol. 29, no. 14, pp. 21698–21710 (2021) doi: 10.1364/OE.430320
10. Aguirre-Aguirre, D., Diaz-Uribe, R., Campos-García, M., Villalobos-Mendoza, B., Izazaga-Pérez, R., Huerta-Carranza, O.: Fast conical surfaces evaluation with null-screen and randomized algorithms. Applied Optics, vol. 56, no. 5, pp. 1370–1382 (2017) doi: 10.1364/AO.56.001370
11. Díaz-Uribe, R.: Medium precision null screen testing of off-axis parabolic mirrors for segmented primary telescope optics; the case of the Large Millimetric Telescope. Applied Optics, vol. 39, no. 16, pp. 2790–2804 (2000) doi: 10.1364/AO.39.002790
12. Noll, R. J.: Zernike polynomials and atmospheric turbulence. Journal of the Optical Society of America, vol. 66, no. 3, pp. 207–211 (1976) doi: 10.1364/JOSA.66.000207

ISSN 1870-4069

Numerical Modeling of Field Patterns in a Photonic Crystal Waveguide with Metamaterial Cylindrical Inclusions

Alejandro Bucio-Gutiérrez[1], Karla Serrano-Arévalo[1], Gabriel Arroyo-Correa[1], Hugo Alva-Medrano[2], Héctor Pérez-Aguilar[1]

[1] Universidad Michoacana de San Nicolás de Hidalgo, Facultad de Ciencias Físico Matemáticas, Mexico

[2] Instituto Tecnológico de Morelia, Departamento de Ciencias Básicas, Mexico

hiperezag@yahoo.com

Abstract. The study of photonic crystal waveguides (PCWs) is of current interest from the theoretical and applied point of view of optics, telecommunications and even in the area of medicine in the monitoring of biomolecules. In this work we consider an electromagnetic system composed of two flat conductive plates and a periodic array of circular cylindrical metamaterial (LHM) inclusions forming a PCW. A numerical integral method was applied to determine the dispersion relation that allows us to characterize eigenmodes of the system and the intensity of field of its electromagnetic modes. The results show ordered and disordered patterns of field intensities in a dispersive LHM medium. Although the presence of a disordered pattern is not enough to affirm the presence of electromagnetic chaos phenomenon, this behavior can be evidenced through an analysis of the field in terms of spatial statistics and correlations, which allows us to show numerically that the correlation length of the field autocorrelation function approaches zero. These wave chaos properties in a PCW involving LHM could have various applications in modern communication technology.

Keywords: Photonic crystal waveguide, metamaterial, electromagnetic chaos, correlation length.

1 Introduction

The study of photonic crystal waveguides (PCWs) is of current interest from the theoretical and applied point of view of optics, telecommunications and even in the area of medicine in the monitoring of biomolecules [1]. A particularly important issue in this field is the attempt to identify evidence of chaos phenomenon in the transport properties of ballistic systems. As matter of fact, the magnetoresistance has been measured in chaotic and regular cavities showing clear distinctions in quantum transport [2].

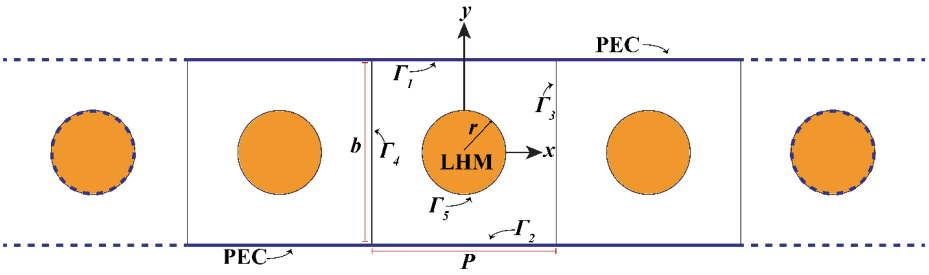

Fig. 1. Diagram of the PCW formed by two PEC flat surfaces and a periodic array of circular cylindrical inclusions of LHM in the x-direction.

The signature of chaos in classical transport through waveguides has also been investigated, and shows a completely different behavior on the resistivity when the system is regular or chaotic [4]. In this paper, the Integral Equation Method (IEM) [5] was applied to calculate and examine the electromagnetic field intensities of a PCW, formed by two perfect electric conductor (PEC) flat surfaces and a periodic array of circular cylindrical metamaterial (LHM) inclusions, which presents disordered patterns.

Despite the fact that the presence of a disordered pattern is not enough to confirm the presence of the electromagnetic chaos phenomenon, the corresponding classical channel, such as the Sinai billiards obviously exhibit chaotic behavior [7]. Thus, this behavior can be evidenced through an analysis of the field in terms of spatial statistics and correlations, which allows us to show numerically that the correlation length of the field autocorrelation function approaches zero.

A validation of this assumption has been provided by the investigations on the spatial autocorrelation functions that are much more sensitive to the nature of eigenmodes [3]. This paper is organized as follows. In Sec. 2 we introduce an integral method to calculate the field intensity in the unit cell of our system that includes LHM dispersive media associated with electromagnetic modes, based on the ideas outlined elsewhere [5, 6]. Section 3 shows numerical results for a wide range of frequencies, which present disordered patterns. Finally, Sec. 4 presents our conclusions.

2 Theoretical Approach

We consider an infinite two-dimensional system composed of two PEC flat surfaces with circular cylindrical LHM inclusions as shown in Fig. 1. Assuming a harmonic time dependence for TM polarized electromagnetic field, $\mathbf{H} = H(\mathbf{r}, t)\exp(-i\,\omega\,t)\hat{\mathbf{k}}$, the wave equation for medium j becomes the Helmholtz equation:

$$\left[\nabla^2 + k_j^2\right] H_j(\mathbf{r}) = 0, \tag{1}$$

where $\mathbf{r}$ is the position vector in the xy-plane, and we define $k_j = n_j(\omega)(\omega/c)$ with $n_j(\omega) = \pm\sqrt{\varepsilon_j(\omega)\mu_j(\omega)}$ the refractive index of the j-th medium involving the optical properties of the material. The sign of the refractive index will be positive for a dielectric or real conductive medium and negative for LHM inclusions, which is given in terms of magnetic permeability an electric permittivity given by [5] $\varepsilon(\omega) = 1 - \omega_p^2/\omega^2$ and

$\mu(\omega) = 1 - f\omega_p^2/\left(\omega^2 - \omega_0^2\right)$, where ω_0 is the resonance frequency, ω_p is the plasma frequency and f is the filling fraction of the unit cell. The region where this LHM has a negative refractive index value is within the frequency range $\omega_0 << \omega << \omega_{LH}$ with $\omega_{LH} = \omega_0/\sqrt{1-f}$. Equation (1) can be represented in integral form for the medium j, considering as a solution the two-dimensional Green's function $G(\mathbf{r}, \mathbf{r}')$ of the equation:

$$\left[\nabla^2 + k_j^2\right] G_j(\mathbf{r}, \mathbf{r}') = -\delta(\mathbf{r}, \mathbf{r}'). \tag{2}$$

And the Green's integral theorem [5, 6]. Thus, the general form of the Helmholtz integral equation is obtained for the j-th medium:

$$\frac{1}{4\pi} \oint_{\Gamma_j} \left[G_j(\mathbf{r}, \mathbf{r}') \frac{\partial H_j(\mathbf{r})}{\partial n'} - H_j(\mathbf{r}') \frac{\partial G(\mathbf{r}, \mathbf{r}')}{\partial n'} \right] ds' = H_j(\mathbf{r}) \Theta(\mathbf{r}), \tag{3}$$

Being $G(R) = (i/4)H_0^1(kR)$, where $H_0^1(\zeta)$ is the Hankel function of the first kind and zero order, $R = |\mathbf{r} - \mathbf{r}'|$ and $\Theta(\mathbf{r}) = 1$ if $\mathbf{r}$ is inside the region j and $\Theta(\mathbf{r}) = 0$ otherwise. Due to the geometry of the study problem (see Fig. 1), we have the boundary conditions for the TM polarization on the contour Γ_j, $H_j = H_{j+1}$ and $1/\varepsilon_j \partial H_j/\partial n = 1/\varepsilon_{j+1}\partial H_{j+1}/\partial n$.

And by translational symmetry through a PCW, based on Bloch's theorem, we can state that $H(x - P, y) = H(x, y)\exp(-iKP)$ where K is the one-dimensional Bloch vector. In order to solve Eq. (3) numerically, it is necessary to make a discretization by dividing the curve Γ_j that defines the j-th region into curve segments of arc length Δs small enough so that the field and its normal derivative are constant. Therefore, the integrals of Eq. (3) for the j-th region can be approximated and converted into a system of linear equations [5, 6] for the linearly polarized magnetic field.

Then, the linear system can be represented by $F(K, \omega)\ M(K, \omega) = 0$, where M is the representative matrix associated with the system, which depends on frequency ω and the Bloch vector K. Since the system of equations is homogeneous, a non-trivial solution can be obtained if the determinant of this matrix is zero. Thus it is possible to determine the band structure by finding the dispersion relation $\omega = \omega(K)$. For this, we define the determinant function:

$$D(K, \omega) = \ln(|\det(M(K, \omega))|). \tag{4}$$

Which presents local minimum points that allow to determine the eigenmodes of the system for a specific frequency.

3 Results

In numerical simulations it is common to introduce dimensionless values, so our results are expressed in terms of the a reduced Bloch vector given by $K_r = (P/2\pi)K$ and the reduced frequency $\omega_r = (P/2\pi)\,\omega$. Below we present some results of a PCW with an array of circular cylindrical inclusions involving a metamaterial under TM polarization (see Fig. 1). The following geometric values of the unit cell were taken into account: $b = 4\,\pi$, $P = 2\,\pi$ and $r = 0.1\,b$.

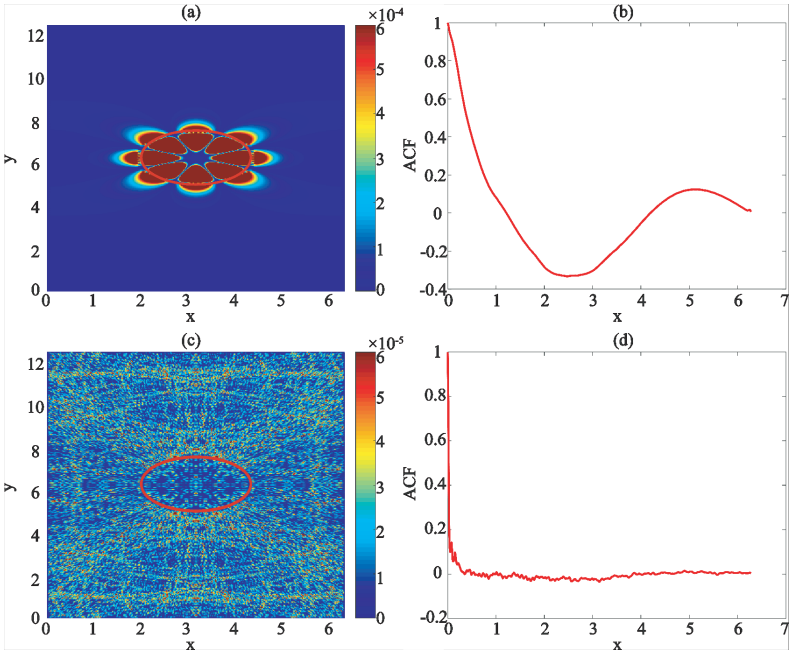

Fig. 2. TM-polarized electromagnetic intensity patterns in a unit cell of the PCW with LHM circular inclusions at the reduced frequencies (a) $\omega_r = 0.6488$ and (c) $\omega_r = 87.1359$. The solid circular curve represents the contour of the inclusion. The corresponding autocorrelation functions are shown in (b) and (d) with correlation lengths $\sigma = 0.2743$ and $\sigma = 0.0584$, respectively.

Figs. 2 (a) and (c), show the intensity of the magnetic field within the unit cell for the LHM inclusion for reduced frequencies $\omega_r = 0.6488$ and $\omega_r = 87.1359$, respectively. Each one with its respective natural frequency $\omega_0 = 0.6366$ and $\omega_0 = 63.6619$. For both cases, the corresponding autocorrelation functions (ACFs) were calculated (Figs. 2(b) and (d)) and their correlation lengths σ defined as the standard deviation of the autocorrelation function. For the lowest frequency, the correlation length obtained is $\sigma = 0.2743$ and for the highest frequency, a lower value $\sigma = 0.0584$.

We observe that the correlation length decreases as the field pattern is more disordered as the frequency increases. Furthermore, we believe this is a manifestation of electromagnetic wave chaos, since in this regime it led us to think that the intensity of the eigenmode is an uncorrelated random variable as a function of a point $(x,\ y)$ in the unit cell [3]. On the other hand, some classical systems with similar geometry, such the Sinai billiards [7] exhibit chaotic behavior.

4 Conclusions

An IEM was applied to study a PCW composed by two PEC flat surfaces and a periodic array of circular cylindrical inclusions of dispersive LHM. For certain conditions, disordered patterns of field intensities were obtained in our system.

In general, disordered patterns are associated with disordered systems, so this result, together with the fact that the corresponding classical model of our electromagnetic system presents a chaotic behavior, are our main arguments in terms of interpreting some of our results as manifestations of electromagnetic wave chaos in LHM media.

In addition, the signature of classical chaotic behavior can be seen in the spatial statistical properties of the system such as the correlation length. This assumption has been demonstrated in our results since the value of the correlation length is smaller when the frequency is high. These electromagnetic wave chaos properties in a PCW that include dispersive LHM media could have various applications in modern communication technology.

Acknowledgments. Héctor Pérez-Aguilar and Gabriel Arroyo-Correa express their gratitude to the Coordinación de la Investigación Científica of the Universidad Michoacana de San Nicolás de Hidalgo for the financial support granted for the development of this research project.

References

1. Alivisatos, P.: The use of nanocrystals in biological detection. Nature Biotechnology, vol. 22, no. 1, pp. 47–52 (2003) doi: 10.1038/nbt927
2. Chang, A. M., Baranger, H. U., Pfeiffer, L. N., West, K. W.: Weak localization in chaotic versus nonchaotic cavities: a striking difference in the line shape. Physical Review Letters, vol. 73, no. 15, pp. 2111–2114 (1994) doi: 10.1103/physrevlett.73.2111
3. Doya, V., Legrand, O., Mortessagne, F., Miniatura, C.: Speckle statistics in a chaotic multimode fiber. Physical Review E, vol. 65, no. 5 (2002) doi: 10.1103/physreve.65.056223
4. Herrera-González, I. F., Arroyo-Correa, G., Mendoza-Suárez, A., Tututi, E. S.: Study of the resistivity in a channel with dephased ripples. International Journal of Modern Physics B, vol. 25, no. 5, pp. 683–698 (2011) doi: 10.1142/s0217979211057943
5. Mendoza-Suárez, A., Pérez-Aguilar, H.: Numerical integral methods to study plasmonic modes in a photonic crystal waveguide with circular inclusions that involve a metamaterial. Photonics and Nanostructures - Fundamentals and Applications, vol. 21, pp. 1–12 (2016) doi: 10.1016/j.photonics.2016.04.003
6. Pérez-Aguilar, H., Mendoza-Suárez, A., Tututi, E., Herrera-González, I.: Chaotic behavior of a quantum waveguide. Physica B: Condensed Matter, vol. 411, pp. 93–98 (2013) doi: 10.1016/j.physb.2012.11.039
7. Suppes, P., de-Barros, J. A.: Photons, billiards and chaos. Law and Prediction in the Light of Chaos Research, pp. 189–201 (2007) doi: 10.1007/bfb0101878

ISSN 1870-4069

Band Structures of a Photonic Crystal Waveguide with Koch Snowflake Fractal Structures

Eduardo Mellado-Villaseñor[1], Hugo Alva-Medrano[2], Héctor Pérez-Aguilar[1]

[1] Universidad Michoacana de San Nicolás de Hidalgo, Facultad de Ciencias Físico Matemáticas, Mexico

[2] Instituto Tecnológico de Morelia, Departamento de Ciencias Básicas, Mexico

hiperezag@yahoo.com

Abstract. Many applications used today are based on the study of certain geometric tools; for example, a peculiar geometry known as fractals. In this work an integral method was developed to calculate the band structures of a photonic crystal waveguide, formed by two parallel conducting plates and an array of inclusions involving Koch snowflake fractal structures. The numerical technique is known as the Integral Equation Method, which starts from Green's second identity to solve the two-dimensional Helmholtz equation. We found that varying the inclusion size for several iterations of the Koch fractal structure allows us to control the band structure of the system. The results show the appearance of several band gaps that substantially modify the photonic band structure. Furthermore, it is possible to obtain discrete modes for a certain frequency range and then the periodic photonic crystal waveguide acts as an unimodal filter. These optical properties exhibit some interest from a technological point of view.

Keywords: Photonic band structures, Koch snowflake, band gaps, integral equation method.

1 Introducción

By analyzing certain geometric tools with the aim of being used in many research methods, this leads to the discovery of applications of great interest [2]. For example, a very peculiar geometry known as fractals, these appear both in nature and in the exact sciences [1]. Scattering of light by fractal surfaces has attracted some attention over the years, with the research reported so far being based on approximate approaches to the scattering equations or with reentrant fractals [4].

On the other hand, the determination of the band structure, reflectance, and transmittance of one- and two-dimensional photonic crystals with a complex unit cell structure, such as fractal geometries, has been developed based on the solution of integral equations [3]. In this context, we present a theoretical and numerical study of the electromagnetic response of a photonic crystal waveguide (PCW) based on the adoption Koch snowflake fractal structures.

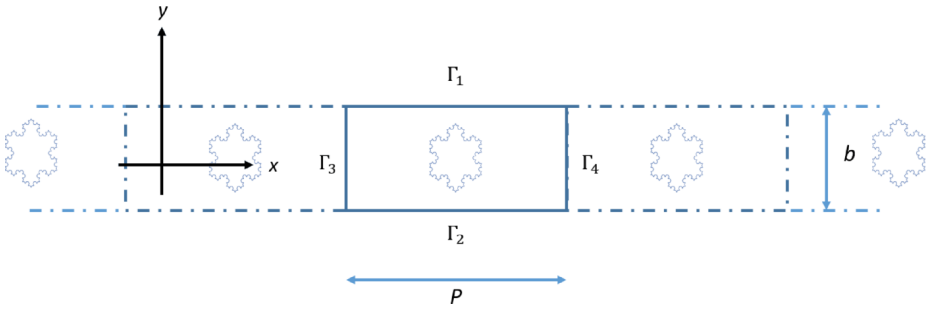

Fig. 1. Schematic description of a periodic waveguide with inclusions formed with perfectly-conductive Koch fractal structures.

To solve this problem, it was done using a numerical technique known as the Integral Equation Method (IEM) [3, 5], which starts from Green's second identity to solve the two-dimensional Helmholtz equation. This paper is organized as follows. In Sec. 2 we introduce an integral method for calculating the dispersion relation to determine the band structures of PCW with Koch snowflake fractal structures, based on ideas described in [3, 5]. Sec. 3 shows the numerial results of band structures of the considered system for different inclusion sizes with several iterations of the Koch fractal structures. Finally, Sec. 4 presents our conclusions.

2 Theoretical Approach

We consider a two-dimensional PCW, formed by two flat internal walls that enclose an array of Koch snowflake fractal structures. The surfaces involved are perfectly-conductive materials and the medium between the walls and the inclusions is vacuum. The geometry of the system is sketched in Fig. 1. In PCW we consider a period P in the flat profiles, a separation between the plates of the waveguide plates given by b and the Koch fractal inclusions for a given iteration, which can be in terms of the side length L of the original triangle.

2.1 Integral Equation Method

Assuming a time dependency $e^{-i\omega t}$ for electromagnetic fields, the wave equation can be transformed into the Helmholtz equation:

$$\nabla^2 \Psi_j(\mathbf{r}) + n_j^2(\omega)\frac{\omega^2}{c^2}\Psi_j(\mathbf{r}) = 0, \tag{1}$$

where j indicates the j-th medium with refractive index $n_j = \sqrt{\varepsilon_j}$ forming the system under study begin ε_j the electric permittivity, which is shown in Fig. 1. In Eq. (1) ω is the frequency of the electromagnetic wave, c is the speed of light in vacuum, and $\mathbf{r} = x\hat{\mathbf{i}} + y\hat{\mathbf{j}}$ is independent of z.

The function Ψ^j represents the electric or magnetic field and the polarization TE is considered in this work. To solve Eq. (1), we introduce a Green function $G(\mathbf{r}, \mathbf{r}')$, as the solution of the equation given by:

$$\nabla^2 G_j(\mathbf{r}, \mathbf{r}') + n_j^2(\omega)\frac{\omega^2}{c^2}G_j(\mathbf{r}, \mathbf{r}') = -4\pi\delta(\mathbf{r} - \mathbf{r}'), \tag{2}$$

where $\delta(\mathbf{r} - \mathbf{r}')$ is the Dirac delta. A Green function that is a solution of Eq. (2) is given by:

$$G_j(\mathbf{r}, \mathbf{r}') = i\pi H_0^1 n_j \left(\frac{\omega|\mathbf{r} - \mathbf{r}'|}{c}\right), \tag{3}$$

With $H_0^1(z)$ the Hankel function of the first kind and zero order. Applying Green's second integral theorem [3, 5] for the functions Ψ and G in each region corresponding to the j-th medium:

$$\Psi_j(\mathbf{r})\theta_j(\mathbf{r}) = \frac{1}{4\pi}\int_{\Gamma_j}\left[G_j(\mathbf{r}, \mathbf{r}')\frac{\partial\Psi_j(\mathbf{r}')}{\partial n'} - \Psi_j(\mathbf{r}')\frac{G_j(\mathbf{r}, \mathbf{r}')}{\partial n'}\right]ds', \tag{4}$$

where $\theta_j(r)$ is a step function whose values is one for all points in the medium j-th and zero otherwise. In Eq. (4) the surface is bounded by the corresponding closed boundary Γ_j and the normal derivative $\partial/\partial n'$ goes outside the boundary Γ_j. To solve Eq. (4) it is necessary to convert the integro-differential equations into matrix equations by means of a rectangle approximation to evaluate the integrals in small intervals.

Under this consideration, Eq. (4) is transformed into the system of linear equations where matrix elements L_{mn}^j and N_{mn}^j [3]. The property of periodicity that the system has in the x-direction direction is a condition of symmetry that is especially considered. Due to this property and the form of Eq. (1), Bloch's theorem establishes a periodicity condition as $\Psi(x - P, y) = \Psi(x, y)\mathrm{e}^{-iKP}$ with K the Bloch vector.

On the other hand, we have that the boundary conditions along the contours Γ_j are given by $\Psi_n^{(j)} = \Psi_n^{(j+1)} = 0$ and $\partial\Psi_n^{(j)}/\partial n = \partial\Psi_n^{(j+1)}/\partial n$, for TE polarization, where $j = 1$ y 2. With these considerations we find a matrix equations $M(\omega)\ F(\omega) = 0$, which has a representative matrix M and F the source vector, and both depend on the frequency ω and the Bloch vector K. To determine the frequency ω we define the determinant function:

$$D(K, \omega) = \ln|\det(K, \omega)|. \tag{5}$$

Which numerically presents local minimum points that will give us the numerical dispersion relatio, $\omega = \omega(K)$.

3 Photonic Band Structures

In this work we are going to introduce dimensionless values, so our results are expressed in terms of the reduced Bloch vector given by $K_r = (P/2\pi)K$ and the reduced frequency $\omega_r = (P/2\pi)\omega$. The photonic band structures of a PCW with an array of perfectly conducting inclusions involving Koch snowflake fractal structures (see Fig. 1) are shown below.

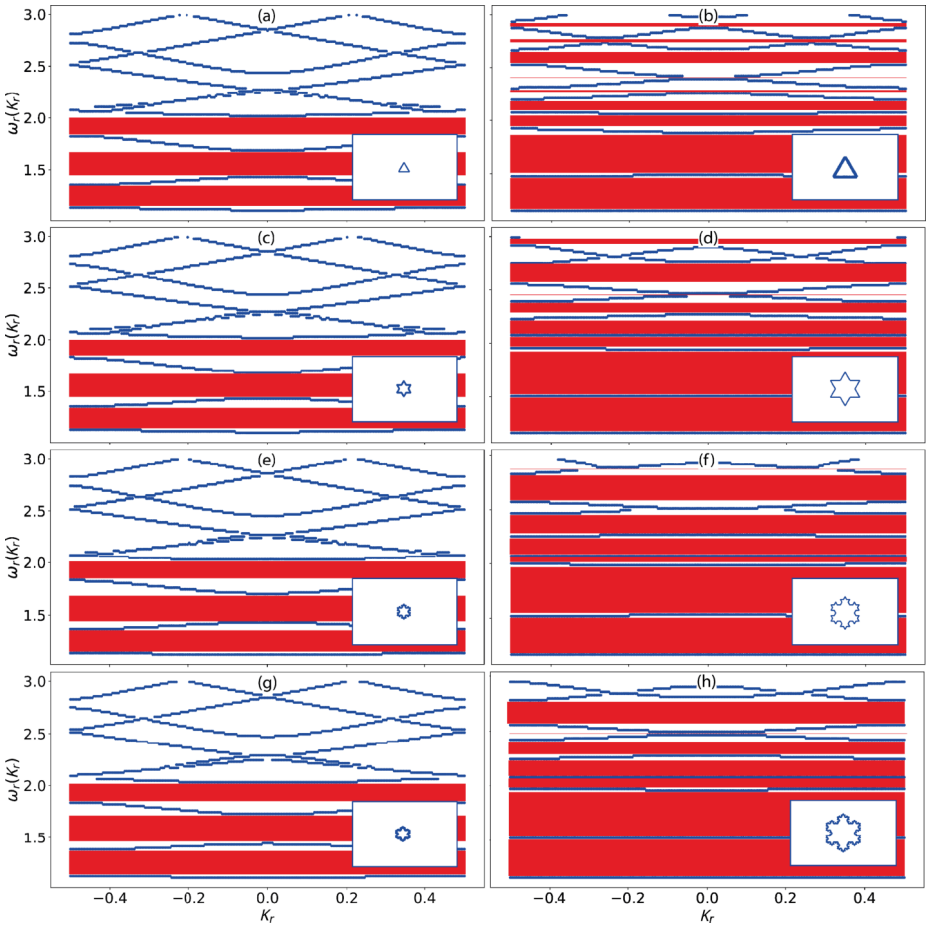

Fig. 2. Photonic band structures of the perfectly conducting PCW that is formed with an array of Koch fractal inclusions of (a) and (b) 0, (c) and (d) 1, (e) and (f) 2, (g) and (h) 3 iterations for the side lengths $L = 1/3$ (first column) and $L = 1$ (second column) of the original triangle. The band gaps are represented by the red stripes. The insets on the right show unit cells in real space whose cross sections of inclusions are made up of Koch snowflake fractals of various orders.

The geometrical values of the waveguide taken into account were: $b = \pi\,\mu$ m and $P = 2\pi\,\mu$ m. Figure 2 shows the band structures of the rectangular lattice with Koch snowflake fractals of $n = 0$, 1, 2 and 3 iterations for the side lengths $L = 1/3$ [Figs. 2(a), (c), (e) and (g)] and $L = 1$ [Figs. 2 (b), (d), (f) and (h)] of the original triangle, respectively.

The results show the appearance of several band gaps (red stripes) as the size of the inclusions and the order of fractal iterations increases, which substantially modify the photonic band structure. Furthermore, it is possible to obtain discrete modes [Figs. 2(d), (f) and (h)] for a given frequency range and then the PCW with Koch fractal structures can act as a unimodal filter.

4 Conclusions

We applied an integral numerical method to calculate the photonic band structures of a PCW formed by two perfectly conducting parallel plates and an array of of inclusions involving Koch snowflake fractal structures. The numerical results obtained show good accuracy and efficiency of the numerical method applied. In addition, it was found that varying the inclusion size for several iterations of the Koch snowflake fractal allows to control the band structure of the system to some extent.

The results show the appearance of several band gaps that substantially modify the photonic band structure. Moreover, it is possible to obtain discrete modes for a certain range of frequencies and then the PCW acts as an unimodal filter. This system is considered as a photonic crystal whose band structures correspond in many respects as a conventional photonic crystal, but using only one material. Therefore, the results of the optical response of a periodic PCW with Koch fractal structures promise excellent and interesting optical applications such as filtering and coding of optical signals.

Acknowledgments. This research was supported by Consejo Nacional de Ciencia y Tecnología through a scholarship for Eduardo Mellado-Villaseñor. Likewise, Héctor Pérez-Aguilar expresses his gratitude to the Coordinación de la Investigación Científica of the Universidad Michoacana de San Nicolás de Hidalgo for the financial support grantedfor the development of this research project.

References

1. Cannon, J. W., Mandelbrot, B. B.: The fractal geometry of nature. The American Mathematical Monthly, vol. 91, no. 9, pp. 594 (1984) doi: 10.2307/2323761
2. Fisher, Y.: Fractal image compression: Theory and application. Fractals, 2nd Edition, pp. 347–361 (1994) doi: 10.1007/978-1-4612-2472-3
3. Mendoza-Suárez, A., Villa-Villa, F., Gaspar-Armenta, J. A.: Numerical method based on the solution of integral equations for the calculation of the band structure and reflectance of one and two-dimensional photonic crystals. Journal of the Optical Society of America, vol. 23, no. 10, pp. 2249–2256 (2006) doi: 10.1364/JOSAB.23.002249
4. Mendoza-Suárez, A., Méndez, E. R.: Light scattering by a reentrant fractal surface. Applied Optics, vol. 36, no. 15, pp. 3521 (1997) doi: 10.1364/ao.36.003521
5. Mendoza-Suárez, A., Pérez-Aguilar, H.: Numerical integral methods to study plasmonic modes in a photonic crystal waveguide with circular inclusions that involve a metamaterial. Photonics and Nanostructures - Fundamentals and Applications, vol. 21, pp. 1–12 (2016) doi: 10.1016/j.photonics.2016.04.003

ISSN 1870-4069

Propagation of a Light Ray in a Sinai Billard-Shaped Cavity: Entropic Characterization of Quasi-Regular and Chaotic Trajectories

Karla Ivonne Serrano-Arévalo, Alejandro Bucio-Gutiérrez,
Gabriel Arroyo-Correa, Héctor Pérez-Aguilar

Universidad Michoacana de San Nicolás de Hidalgo,
Facultad de Ciencias Físico Matemáticas,
Mexico

hiperezag@yahoo.com

Abstract. Billiard dynamics has been widely studied in the literature due to its applications to model real processes. Regular behaviors (as occurs in rectangular and elliptic billiards) and disordered or chaotic behaviors (as occurs in the cases of Sinai and Bunimovich billiards, to mention just a few), have been analyzed in the literature from different approaches. In this paper we analyze the propagation of a light ray in a Sinai billiard-shaped cavity using an entropic approach that consists of calculating the image entropy in the phase space of the trajectories followed by the light ray in the billiard. The entropic difference between quasi-periodic and chaotic trajectories is studied. A one-dimensional Lorentz map is also constructed based on the distances between the initial point and the subsequent collision points at the boundaries of the billiard. The results obtained allow differentiating quasi-regular and chaotic states according to their entropic characteristics and their Lorentz maps.

Keywords: Light ray, cavity, Sinai billiard, order, chaos, entropy.

1 Introduction

Dynamics is the science that studies the variation in time of different magnitudes, i.e. their motion. There are basically three types of movements: stationary and equilibrium movements; periodic and quasi-periodic movements; and chaotic movements, the latter being those in which the prediction of the movement in a sufficiently long time is almost impossible. The word chaos and the adjective chaotic are used to describe a system that apparently has an irregular behavior and is sensitive to small changes in its initial conditions.

A clear example of this is the so-called butterfly effect, which is perhaps the most publicized analogy to imply that in chaotic dynamical systems small variations in the initial conditions can lead to unexpected results [1]. Many interesting examples of dynamical systems of problems in classical mechanics, quantum mechanics, statistics, acoustics and optics (especially those in which the interaction between particles involves elastic collisions) can be reduced to billiard systems [2].

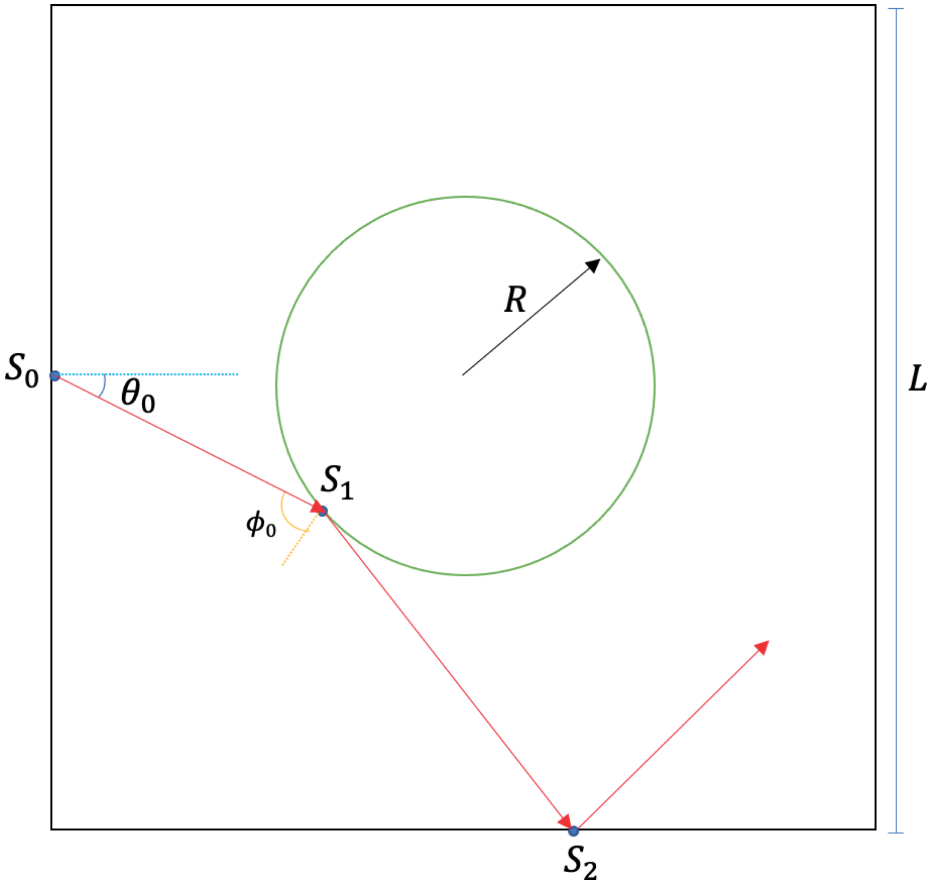

Fig. 1. The Sinai billiard consists of a square and a circular inclusion at its center. The particle moves classically experiencing only elastic collisions with the walls.

To speak of billiard systems will mean to speak of point particles moving over some region (the "billiard table") that may or may not contain smooth convex obstacles and undergoing elastic collisions against them.

2 Theory

A dynamical system representing the motion of a free particle within a bounded region of space, with elastic reflections at the boundaries, is known as a billiard [2]. The dynamical properties of billiards are determined by the shape of the boundary and can vary from totally regular to totally disordered or chaotic behaviors, similar in many respects to that of randomly evolving systems [3]. In this paper we study, in the light of classical mechanics, the Sinai billiard which is a relatively simple system presenting a strongly chaotic behavior [3].

Table 1. Table of geometries for trajectory analysis.

G_n	S_0	θ_0	$E_i(TN)$	$E_i(TC)$
G_1	$(-0,5,0.374)$	$\arctan(1)$	1.47511	5.17524
G_2	$(-0,5,0)$	$\arctan(3.5)$	4.06182	5.0533
G_3	$(-0,5,0)$	$\arctan(13.5)$	5.78356	5.0464
G_4	$(-0,5,0)$	$\arctan(32)$	5.02251	5.13676
G_5	$(-0,5,0)$	$\arctan(\sqrt{2}/2)$	5.03952	4.98736
G_6	$(-0,5,0)$	$\arctan(\sqrt{7}/2)$	2.00555	5.1196

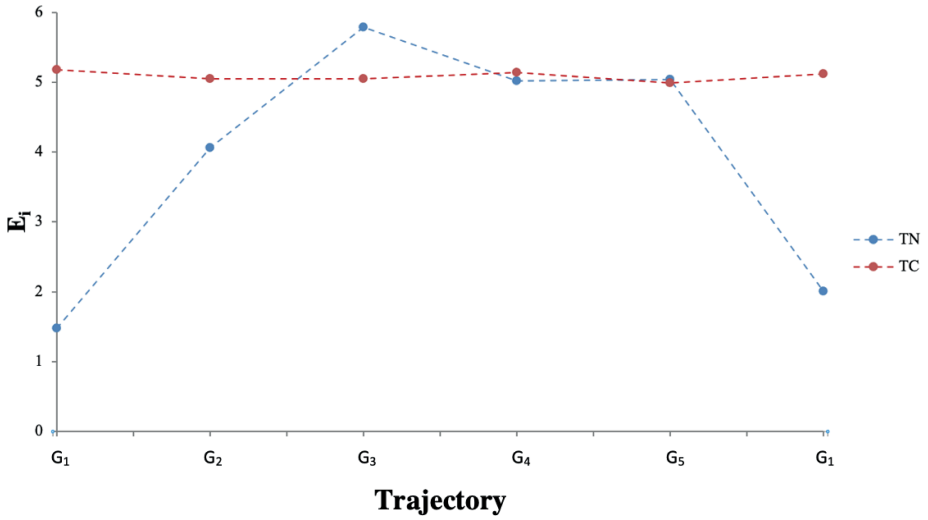

Fig. 2. Image entropy (E_i) for TN y TC.

The system consists of a particle moving in the plane inside a square (side L), at the center of which is placed a circular inclusion (radius R), as shown in Fig. 1. The particle (mass m) is assumed to obey the laws of classical mechanics and only undergoes elastic collisions against the walls of the square and the perimeter of the circular obstacle. That is, between collisions the particle moves freely following a rectilinear trajectory.

The collisions of the particle against the billiard walls are numbered consecutively by means of the index n which takes integer values, $n = 0, 1, 2, 3, \cdots$. At each collision (say, the nth) two variables are specified, namely: the position of the point where the collision occurs (variable S_n) and the angle that the direction of the movement forms with the wall immediately after the collision (angle θ_n).

We identify the position S with the parameterized distance along the perimeter measured from the lower right corner of the square. At the initial time the particle is in the state (S_0, θ_0), i.e., the particle undergoes a collision with the left wall at point S_0 and emerges from the collision forming an angle θ_0, as shown in Fig. 1. Knowing (S_0, θ_0) we want to predict the state (S_1, θ_1) corresponding to the next collision of the particle against a wall of the square or possibly against the circular object, whose existence depends on the values (S_0, θ_0) and the radius R of the disk.

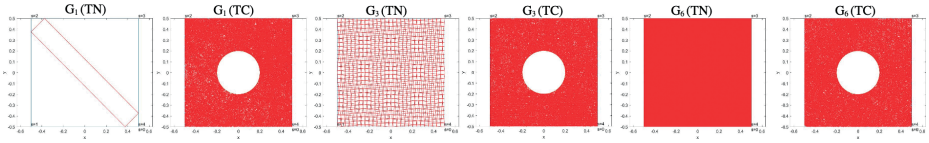

Fig. 3. Trajectories without inclusion (NT) and with inclusion (CT), for the cases G_1, G_3 and G_6 of Table 1.

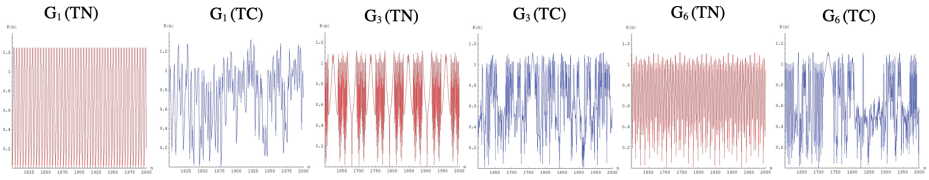

Fig. 4. Series for the trajectories without inclusion (TN) and with inclusion (TC), for the cases G_1, G_3 and G_6 of Table 1.

Once $(S_1,\ \theta_1)$ is determined, one follows with the prediction of the state $(S_2,\ \theta_2)$ and so on [4]. In the present work the point $(S_0,\ \theta_0)$ identifies the point of emission of the light ray inside the cavity. In this work, the program developed by Lansel and Porter [5] to simulate the dynamics of classical billards was used.

Given the position and direction of the previous collision, the program calculates the position and direction of the point particle after its subsequent collision with the billiard boundary. To find the location of the next collision, the program looks for an intersection between the line describing the path of the point particle and each of the collisions against the billiard walls.

Given all these intersections, the point with the minimum distance traveled is the next intersection point. To find the direction in which the point particle travels after the collision, the angle at the normal to the boundary is calculated from the derivative of the parametric equations of the billiard at the intersection point. This process leads to the mapping [4]:

$$\theta_n = 2\arctan\left(\frac{dy}{dt}\Big/\frac{dx}{dt}\right)\Bigg|_{t_n} - \theta_{n-1}, \tag{1}$$

$$\phi_n = \arctan\left(\frac{dy}{dt}\Big/\frac{dx}{dt}\right)\Bigg|_{t_n} - \theta_{n-1} + \frac{\pi}{2}, \tag{2}$$

where θ_n represents the angle with respect to the horizontal of the nth iteration, ϕ_n represents the incident angle of the nth iteration, $y(t)$ and $x(t)$ are the parametric equations of the billiard boundary, and t_n is the value of t that gives the location of the nth intersection with the boundary. The entropy is a statistical measure of randomness that can be used to characterize the texture of the input image.

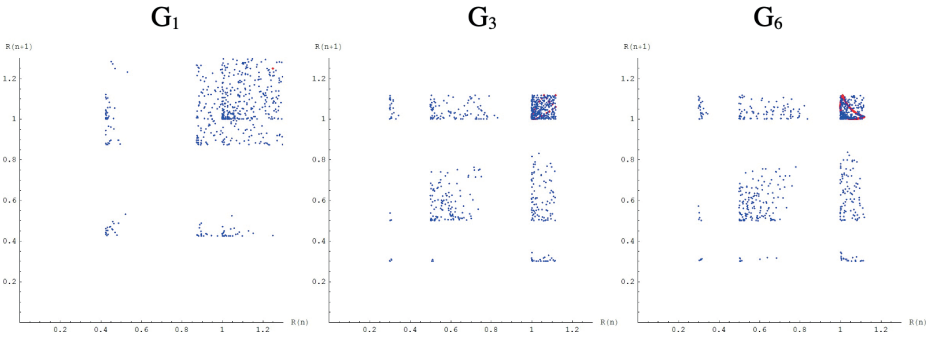

Fig. 5. Comparative plots of the Lorentz maps for G_1, G_2 and G_3. The red and blue points correspond to the maps for the cases TN and TC, respectively.

We use the Mathematica program to calculate the image entropy E_i, defined by:

$$E_i = -\sum_{k=1}^{N} p_k \log_2 (p_k) , \tag{3}$$

where N is the total number of pixels of the image and p_k is the probability value associated with the grayscale level of the kth pixel. The distances between the emission point S_0 and the collision points S_n $(n = 1, 2, 3, ...)$ are the parameters that define a series as a function of the collision number as follows:

$$R_n = \overline{S_0\, S_n}. \tag{4}$$

Lorentz maps are constructed for the R_n series of Eq. (3).

3 Results

Table 1 shows the analyzed trajectories G_n, where 2000 iterations were taken in each case. The characteristics of the light rays, initial position S_0 and initial angle θ_0, as well as the image entropies E_i, both for the trajectories with absence (TN) and presence (TC) of circular inclusion, are shown in the table. Figure 2 shows the entropic behavior. In Fig. 3 the TN and TC trajectories for a circular inclusion of $R = 0.2$ are shown, for some of the cases in Table 1 (G_1, G_3 and G_6). Figure 4 presents the series associated with the distances between the light ray emission point and the collision points as a function of the collision number. Figure 5 shows the Lorentz maps for the TN and TC trajectories, for some of the cases presented in Table 1.

4 Conclusions

The dynamics of the propagation of a light ray in a Sinai billiard-shaped cavity for the TN and TC trajectories was studied. The calculation of the image entropies E_i and the construction of Lorentz maps allowed us to identify characteristics of the dynamics for

the TN and TC trajectories. In particular, the Lorentz maps graphically showed regions where the quasi-regular and chaotic nature of the TN and TC trajectories can be easily recognized. The results of this work can be applied in the design and construction of two-dimensional light traps.

Acknowledgments. This research was supported by Consejo Nacional de Ciencia y Tecnología through a scholarship for Karla Ivonne Serrano-Arévalo and Alejandro Bucio-Gutiérrez. Likewise, Héctor Pérez-Aguilar and Gabriel Arroyo-Correa express their gratitude to the Coordinación de la Investigación Científica of the Universidad Michoacana de San Nicolás de Hidalgo for the financial support granted for the development of this research project.

References

1. Mullin, T.: The nature of chaos. Oxford Science Publications (1993)
2. Birkhoff, G. D.: On the periodic motions of dynamical systems. Acta Mathematica, vol. 50, pp. 359–379 (1927) doi: 10.1007/bf02421325
3. Sinai, Y. G.: Dynamical systems with elastic reflections. Russian Mathematical Surveys, vol. 25, no. 2, pp. 137–189 (1970) doi: 10.1070/rm1970v025n02abeh003794
4. Triana-Ándres, S., Campos, D.: El billar de Sinai clásico. Revista de la Academia Colombiana de Ciencias Exactas, Físicas y Naturales, vol. 23, no. 86, pp. 61–71 (1999)
5. Lansel, S., Porter, M. A.: Graphical user interface to simulate classical billiard systems. School of Mathematics and Center for Nonlinear Science, School of Physics (2004) doi: 10.48550/arXiv.nlin/0405003

ISSN 1870-4069

Numerical Study of Surface Plasmon Resonance in Rough Thin Films under the Kretschmann Configuration

Sergio Sánchez-López, Eric Galván-Navarro,
José Medina-Magallón, Mary Carmen Peña-Gomar,
Héctor Pérez-Aguilar

Universidad Michoacana de San Nicolás de Hidalgo,
Facultad de Ciencias Físico Matemáticas,
Mexico

hiperezag@yahoo.com

Abstract. Despite the existence of a developed technology, there are still defects in the manufacture of surfaces for different optical components with optimal performance. In this work we present a numerical analysis of the effects of roughness on surface plasmon resonance (SPR) excitation in a multilayer system under the Kretschmann configuration that is formed by rough conducting and dielectric thin films. To numerically model the optical response of the system, we have used the Integral Equation Method and the Lorentz-Drude model. Furthermore, rough surface profiles are generated by a random Gaussian correlation process that obeys an exponential probability density function, whose parameters are the standard deviation of heights σ and the correlation length δ. In this study we have calculated the reflectance as a function of incidence angle for a normalized Gaussian beam. The results obtained indicate that the SPR angles for the smooth thin films had an angular displacement due to the influence of roughness. Therefore, roughness in surfaces can modify substantially the location of the SPR. These optical properties allow it to have a large number of applications in various fields of science and technology, such as plasmonic sensing.

Keywords: Surface plasmon resonance, Kretschmann configuration, rough thin films, integral equation method.

1 Introduction

The study of multilayer systems are of great interest due to their special optical properties as the absorbance and SPR [3]. The latter, it is based on the confinement of electromagnetic waves on the surface of a metal strongly coupled to collective oscillations of free electrons. The strong confinement of these resonances in the metal surface explains their exceptional sensitivity to changes in the dielectric environment and constitutes the detection mechanism for the development of new technological devices such as solar cells, biosensors or detectors [2, 5]. These surface plasmon oscillations can be excited by electrical or optical stimulation.

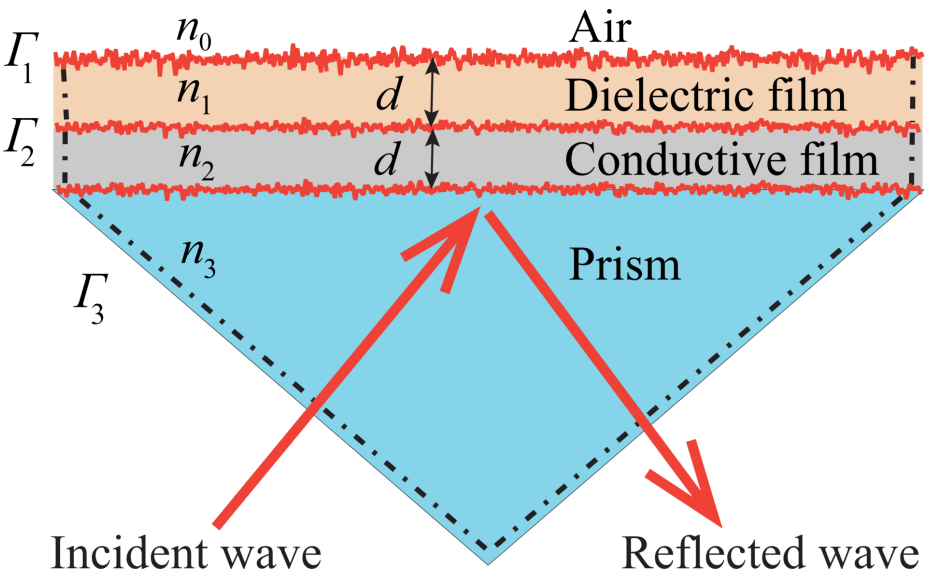

Fig. 1. Diagram of the Kretschmann system formed with rough conductive and dielectric thin films with thicknesses d, characterized by the refractive index n_j for each medium and Γ_j are the contours of the surfaces.

However, excitation cannot be performed by directly incident light on the metal surface because the wave vector of photons is always smaller than that of plasmons. Different techniques have been used to solve this problem, the most important of which is the coupling with a prism called Kretschmann configuration [1]. In this configuration, the metal film evaporates on the prism.

Thus, light illuminates the prism and an evanescent wave penetrates through the metal film, allowing plasmons to be excited on the outer side of the film. This paper is organized as follows. In section 2 we present the system under study and the description of the Integral Equation Method we have used to solve the problem. Section 3 shows the results of the optical response of the system. Finally, in section 4 we present the conclusions of this work.

2 Theoretical Approach

In the present work we will numerically model the SPR in a multilayer system using the Integral Equation Method (IEM) [7, 8] described in this section. The system is shown in Fig. 1. Which is formed of rough conducting and dielectric thin films immersed in an incident medium and a transmission medium with thicknesses d, whose optical properties are given by the refractive index n_j. The rough profile is defined by a random Gaussian correlation process that obeys a negative exponential probability density function, whose parameters are the standard deviation of heights σ and the correlation length δ [4].

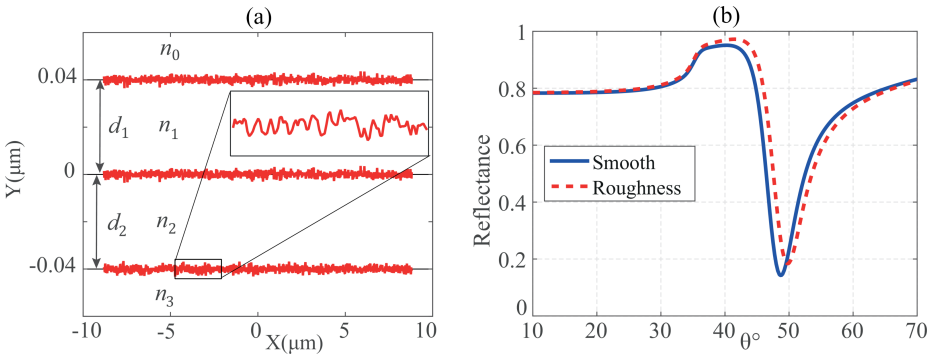

Fig. 2. (a) Profile of the multilayer system under the Kretschmann configuration, which is formed by three interfaces with roughness and four media with refractive indices $n_0 = 1.0$ (air), $n_1 = 1.767$ (Al_2O_3), $n_2 = 0.14316 + i3.7792$ (silver) and $n_3 = 1.723$ (prism) at $\lambda = 629$ nm; layer thicknesses: $d_1 = d_2 = 40$ nm and roughness parameters: $\sigma = 0.001\lambda$ and $\delta = 0.009\lambda$. (b) Reflectances of system formed by rough conductive and dielectric thin films with smooth (solid curve) and rough (dashed curve) surfaces.

2.1 Integral Equation Method

The IEM is based on the numerical solution of the Helmholtz equation which is given by:

$$\nabla^2 \Psi_j(\mathbf{r}) + k_j^2 \Psi_j(\mathbf{r}) = 0, \tag{1}$$

where j indicates the j-th medium, $\mathbf{r} = x\hat{\mathbf{i}} + y\hat{\mathbf{j}}$ is the position vector of the observation point and $\Psi_j(\mathbf{r})$ represents the electric field in the case of TE polarization or the magnetic field in the case of the TM polarization. The magnitude of the wave vector is given by $k_j = n_j(\omega)(\omega/c)$, where the refractive index $n_j(\omega)$ involves material properties and c is the speed of light in vacuum.

To solve equation Ec. (1) let us consider a Green function of the form $G_j(\mathbf{r}, \mathbf{r}') = i\pi H_0^{(1)}(k_j|\mathbf{r} - \mathbf{r}'|)$, where $H_0^{(1)}(z)$ is a Hankel function of the first kind and order zero. Applying the two-dimensional Green second identity to $\Psi_j(\mathbf{r})$ and $G_j(\mathbf{r}, \mathbf{r}')$ to the incident region considered with the prism ($j = 3$) with an incident wave (see Fig. 1), we obtain the scattered field:

$$\Psi(\mathbf{r}) - \Psi_{\text{inc}}(\mathbf{r}) = \frac{1}{4\pi} \int_{\Gamma_3} \left[\frac{G_3(\mathbf{r},\ \mathbf{r}')}{\partial n} \Psi_3(\mathbf{r}) - G_3(\mathbf{r},\ \mathbf{r}') \frac{\partial \Psi_3(\mathbf{r})}{\partial n} \right] ds, \tag{2}$$

where $\Psi_{\text{inc}}(\mathbf{r})$ is the incident field and $G_3(\mathbf{r}, \mathbf{r}')$ is the Green's function in the prism. The source functions $\Psi_3(\mathbf{r})$ y $\partial\Psi_3(\mathbf{r})/\partial n$, represent the values of the electric or magnetic field and its normal derivative evaluated on the Γ_3 contour. For values ($j < 3$) we have:

$$\Psi(\mathbf{r})\Theta(\mathbf{r}) = \frac{1}{4\pi} \int_{\Gamma_j} \left[\frac{G_j(\mathbf{r}, \mathbf{r}')}{\partial n} \Psi_j(\mathbf{r}) - G_j(\mathbf{r},\ \mathbf{r}') \frac{\partial \Psi_j(\mathbf{r})}{\partial n} \right] ds, \tag{3}$$

where $\Theta(\mathbf{r})$ is a function, whose value is one for points in the medium j and zero otherwise.

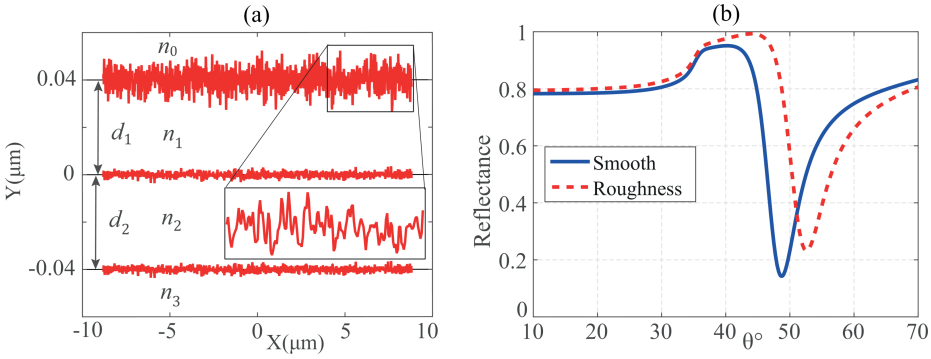

Fig. 3. (a) Profile of the multilayer system under the Kretschmann configuration, which is formed by three interfaces with roughness and four media with $n_0 = 1.0$ (air), $n_1 = 1.767$ (Al_2O_3), $n_2 = 0.14316 + i3.7792$ (silver) and $n_3 = 1.723$ (prism) with roughness parameters: $\sigma_1 = 0.004\lambda$, $\delta_1 = 0.01\lambda$, for the first interfaz and $\sigma_2 = 0.001\lambda$ and $\delta_2 = 0.009\lambda$ for the second and third interfaces. (b) Reflectances of system formed by conductive and dielectric thin films with smooth (solid curve) and rough (dashed curve) surfaces.

Equations (2) and (3) form a system of integro-differential equations with which the total field in the incident and scattering medium can be obtained. To solve them, it is necessary to convert them into matrix equations using a rectangle approximation to evaluate the integrals in small intervals. The details of the discretization of these equations can be consulted in [8, 6]. Once the system of integro-differential equations has been solved, we obtain the values of the source functions with which we can calculate the field at any point. Thus, reflectance can be written as:

$$R(\omega) = \int_{-\pi/2}^{\pi/2} \frac{\partial R}{\partial \theta_s} d\theta_s = \int_{-\pi/2}^{\pi/2} h|A(\theta_s,\, \omega|^2 d\theta_s, \tag{4}$$

where h is a normalization factor that depends on the incident wave and the length of the Γ_3 profile, and $A(\theta_s,\, \omega)$ is the far-field amplitude is given by:

$$A(\theta_s,\, \omega) = \int_{\Gamma_a} \left[-i\frac{\omega}{c}(\mathbf{n}'_a \cdot \hat{\mathbf{r}})\Psi_a(\mathbf{r}') - \frac{\partial \Psi_a(\mathbf{r}')}{\partial n'_a} \right] \times \exp\left(-i\frac{\omega}{c}(\mathbf{r}' \cdot \hat{\mathbf{r}}) \right) ds'. \tag{5}$$

With: $\hat{\mathbf{r}} = (-\cos\theta_s,\, \sin\theta_s)$ and θ_s the angle of scattering.

3 SPR in Rough Thin Films

We analyze the SPR by calculating the reflectance as a function of the angle of incidence for a light beam with $\lambda = 629$ nm. For the excitation of SPR we have used the Kretschmann configuration which is formed by two rough thin films with refractive indices $n_1 = 1.767$ (Al_2O_3) and $n_2 = 0.14316 + i3.7792$ (silver). The mediums surrounding the films are considered with refractive indices $n_0 = 1.0$ (air) y $n_3 = 1.723$ (prism).

In the case of silver, the refractive index was obtained from the Lorentz-Drude model [9]. In Figure 2(a) shows the profile of the multilayer system formed by two rough thin films with thicknesses $d_1 = d_2 = 40$ nm, whose roughness parameters are $\sigma = 0.001\lambda$ and $\delta = 0.009\lambda$. In Fig. 2(b), reflectance of system with rough thin films is shown in comparison with a system consisting of smooth thin films.

Figure 3(a) shows the profile of the multilayer system formed by two rough thin films with thicknesses equal to the previous case. The roughness parameters are $\sigma_1 = 0.004\lambda$, $\delta_1 = 0.01\lambda$, for the first interfaz and $\sigma_2 = 0.001\lambda$ and $\delta_2 = 0.009\lambda$ for the second and third interfaces. In Fig. 3(b) the corresponding reflectances of the system with smooth and rough thin films are shown.

The results obtained in Fig. 2 show that the SPR angle for the smooth case is $\theta = 48.75^\circ$ and for the rough case is $\theta = 49.75^\circ$. In contrast, in Fig. 3, the SPR angle for the rough case is $\theta = 52.5^\circ$ which corresponds to an angular displacement of 3.75 degrees with respect to the smooth case.

4 Conclusions

We have applied the IEM to study the effects of roughness on SPR in Kretschmann configuration. The results obtained show that when considering thin films with small roughnesses, we obtain a slight angular displacement of the minimum value with respect to a system with smooth films. On the other hand, if we consider a combination of films with small and large roughness, we obtain an angular displacement of 3.75 degrees. Also, when considering the two films with large roughness, we obtain a large angular displacement and a higher reflectance with respect to the smooth system.

Therefore, roughness in surfaces can modify substantially the location of the SPR. In general, we have observed that the original position of SPR gradually moves as the roughness parameter δ is increased. Finally, it is worth mentioning that the numerical method used has proven to be reliable for solving problems of this type. This allows this study system to have a large number of applications in various fields of science and technology, such as plasmonic detection.

Acknowledgments. Héctor Pérez-Aguilar and Mary Carmen Peña-Gomar express their gratitude to the Coordinación de la Investigación Científica of the Universidad Michoacana de San Nicolás de Hidalgo for the financial support granted for the development of this research project.

References

1. Agranovich, V. M., Mills, D. L.: Surface polaritons: Electromagnetic waves at surfaces and interfaces. North-Holland Publishing Company, Amsterdam, vol. 1, pp. 33–717 (1982)
2. Dahlin, A. B.: Plasmonic biosensors: An integrated view of refractometric detection. IOS Press (2012)
3. Maier, S. A.: Plasmonics: Fundamentals and applications. Springer Science Business Media LLC (2007)

4. Maradudin, A., Michel, T., McGurn, A., Méndez, E.: Enhanced backscattering of light from a random grating. Annals of Physics, vol. 203, no. 2, pp. 255–307 (1990) doi: 10.1016/0003-4916(90)90172-k
5. Masson, J. F.: Surface plasmon resonance clinical biosensors for medical diagnostics. American Chemical Society Sensors, vol. 2, no. 1, pp. 16–30 (2017) doi: 10.1021/acssensors.6b00763
6. Mendoza-Suárez, A., Villa-Villa, F., Gaspar-Armenta, J. A.: Band structure of two-dimensional photonic crystals that include dispersive left-handed materials and dielectrics in the unit cell. Journal of the Optical Society of America B, vol. 24, no. 12, pp. 3091 (2007) doi: 10.1364/josab.24.003091
7. Mendoza-Suárez, A., Villa-Villa, F., Gaspar-Armenta, J. A.: Numerical method based on the solution of integral equations for the calculation of the band structure and reflectance of one and two-dimensional photonic crystals. Journal of the Optical Society of America B, vol. 23, no. 10, pp. 2249 (2006) doi: 10.1364/josab.23.002249
8. Pérez, H. I., Valencia, C. I., Méndez, E. R., Sánchez-Gil, J. A.: On the transmission of diffuse light through thick slits. Journal of the Optical Society of America A, vol. 26, no. 4, pp. 909 (2009) doi: 10.1364/josaa.26.000909
9. Rakić, A. D., Djurišić, A. B., Elazar, J. M., Majewski, M. L.: Optical properties of metallic films for vertical-cavity optoelectronic devices. Applied Optics, vol. 37, no. 22, pp. 5271–5283 (1998) doi: 10.1364/ao.37.005271

ISSN 1870-4069

Coupling of Light to Plasmonic Modes on Metal Surfaces through the Local Density of States

Rodolfo Cortés-Martínez[1], Félix Humberto Maldonado-Villamizar[2]

[1] Centro de Investigación Científica y
de Educación Superior de Ensenada,
Unidad Monterrey,
Mexico

[2] Consejo Nacional de Ciencia y Tecnología,
Instituto Nacional de Astrofísica, Óptica y Electrónica,
México

rcortes@cicese.mx, fmaldonado@inaoep.mx

Abstract. We study the behaviour of the coupling between a radiating source and a metallic interface, for several geometric and physical configurations. To do this we study the LDOS for the configurations under study and perform analysis for the possible implications of the response of the media to the source.

Keywords: Nanooptics, density of states, plasmonics, quantum optics, purcell enhacement.

1 Introduction

The β-factor is a figure of merit in nano-optics. It describes electromagnetic field enhancement properties to plasmonics modes, such as the NV-color center nanodiamond as emitters with plasmonic nanostructures [3, 5]. Surface polariton plasmons (SPPs) are electromagnetic waves that travel along with a metal–dielectric or metal–air interface, guiding light efficiently in nanoscale elements [5].

They play an essential role in nanophotonics by near-field enhancement and short wavelength. When the separation falls below 20 nm, the classical theory deteriorates progressively due to its neglect of quantum effects. Remarkably, there is an enhancement near material interfaces [8] . The NV color centers in diamonds are of great interest in fields such as quantum information processing. Their use in these applications involves optimizing the lifetime and emission properties of the centers.

However, now, we understand that the interaction between an emitter and its electromagnetic environment by changing this environment can thus modify spontaneous emission. The spontaneous emission decay rate is calculated through the local density of states (LDOS), $\rho(\mathbf{x}, \omega)$, i.e., $\Gamma \sim \rho(\mathbf{x}, \omega)$ [9]. Thus, the modification of the decay rate of an emitter into a plasmonic mode is calculated with the help of the β-factor, which is defined as $\beta = \Gamma/\Gamma_0$.

1.1 The Electromagnetic Field Equations

The behaviour of the electromagnetic fields is ruled by the well-known Maxwell equations:

$$\nabla \cdot \mathbf{D} = \rho, \tag{1}$$

$$\nabla \cdot \mathbf{B} = 0, \tag{2}$$

$$\nabla \times \mathbf{E} = i\omega \mathbf{B}, \tag{3}$$

$$\nabla \times \mathbf{H} = \mathbf{J} - i\omega \mathbf{D}. \tag{4}$$

Along with the respective boundary conditions. Each physical configuration has its own solution. In particular, for the electric field we have the solution:

$$\mathbf{E} = 4\pi \, i \, \omega \, \mu \int \mathbf{G}_0 \cdot \mathbf{J} d^3\mathbf{x}', \tag{5}$$

where the function $\mathbf{G}_0$ satisfies the equation:

$$\nabla \times \nabla \times \mathbf{G}_0 - \omega^2 \, \mu \, \epsilon \, \mathbf{G}_0 = 4\pi \delta(\mathbf{x} - \mathbf{x}')\mathbf{I}, \tag{6}$$

where $\mathbf{G}_0$ is the Green's dyadic and $\mathbf{I}$ is the unit dyadic. We can resolve this equation, i.e. represent it in terms of some basis.

1.2 The Local Density of States (LDOS)

The local density of states is defined as the number of states with energy between k and $k + dk$, in terms of the modes of the electromagnetic field its is proportional to $\sum_n |\psi_{k_n}(\mathbf{x})|^2$. We can prove there is a relation between the imaginary part of the Green's function and the density of states as follow:

$$\rho(\mathbf{x}) = \frac{2\omega}{\pi c^2} \Im \operatorname{Tr} \mathbf{G}_0(\mathbf{x}, \mathbf{x}). \tag{7}$$

The contribution to the density of states from electric and magnetic terms is given by [2]:

$$\rho(\mathbf{x}, \omega) = \frac{1}{2} \left[\rho_E(\mathbf{x}, \omega) + \rho_M(\mathbf{x}, \omega) \right], \tag{8}$$

where the indices E, M stand for the electric and magnetic contribution respectively. Thus, the evident task to perform is the calculation of the Green's function for the appropriate configuration.

1.3 The Coupling to Different Surfaces

The presence of materials, metals dielectrics and different kind of non transparent nature for light to the optical wavelengths are of importance, because depending of the specific nature of them the electromagnetic properties of the quantum emitter or classical radiating dipole will be modified and is our task here to show how this happen.

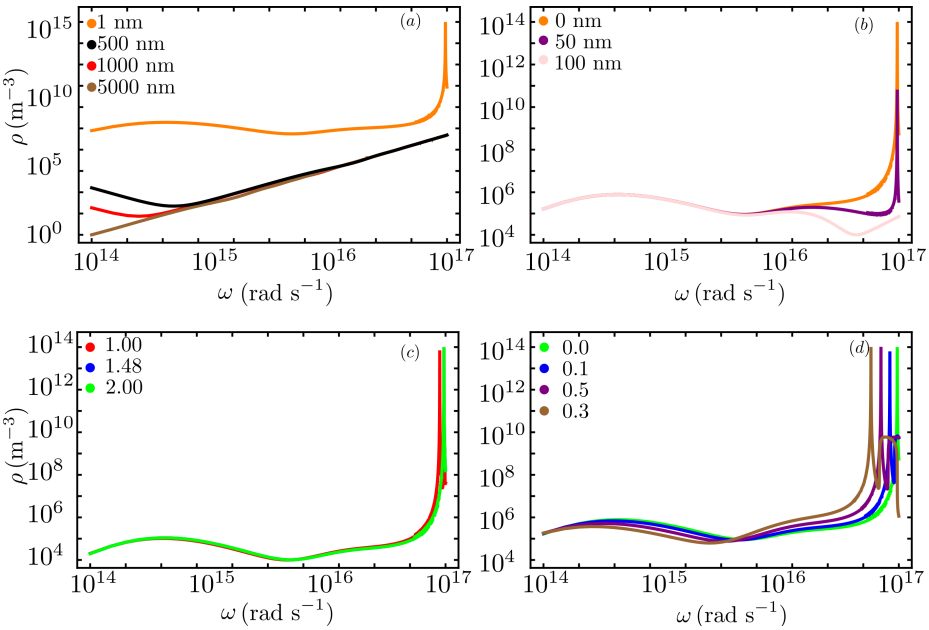

Fig. 1. The figure shows the local density of states for several configurations, for the parameters involved in the coupling of electromagnetic waves to a metallic surface: (a) an emitter at different distances z above the surface, (b) in the roughness of the surface, expressed in terms of the parameter σ, (c) in function of the refraction index n of the neighbor dielectric, (d) as a function of the packed fraction f.

The general case of a dipole placed at a distance z near a semi infinite slab of material is given by [9]:

$$\rho(z,\omega) = \frac{\rho_0}{2}\left\{\int_0^1 \frac{\omega}{c}\frac{dk^2}{2k_{0z}}\left[2 + k^2\Re\left((r_s + r_p)e^{2ik_0 z}\right)\right] + \int_1^\infty \frac{dk^4}{4|k_0|}\Im\left(r_s + r_p\right)e^{-2k_0 z}\right\}, \quad (9)$$

where $k_{0z} = \sqrt{1-k^2}\omega/c$, r_s and r_p are the Fresnel coefficients for the polarization s and p defined as:

$$r_s = \frac{\sqrt{1-k^2} - \sqrt{\epsilon^p - k^2}}{\sqrt{1-k^2} + \sqrt{\epsilon^p - k^2}} e^{-2\left(\frac{2\pi\sigma}{\lambda}\right)^2}, \quad (10)$$

$$r_p = \frac{\epsilon^p\sqrt{1-k^2} - \sqrt{\epsilon^p - \frac{\epsilon^p}{\epsilon^s}k^2}}{\epsilon^p\sqrt{1-k^2} + \sqrt{\epsilon^p - \frac{\epsilon^p}{\epsilon^s}k^2}} e^{-2\left(\frac{2\pi\sigma}{\lambda}\right)^2}, \quad (11)$$

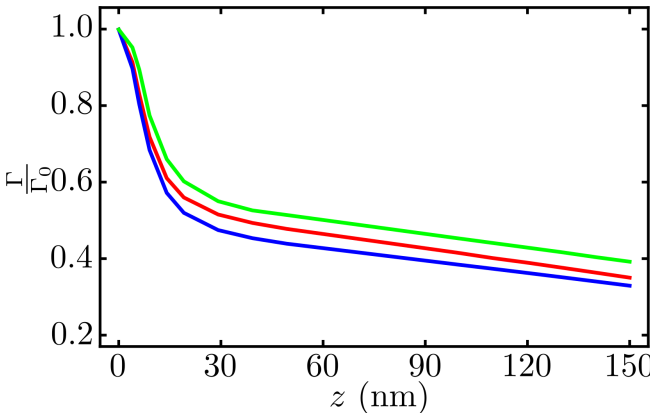

Fig. 2. The Purcell factor β as a function of the distance z over the interface air-material for perfect bulk metal (green), metamaterial $f = 0.1$ (red) and metal with roughness $\sigma = 10$ nm.

where $\epsilon^{s,p}$ are effective permitivity functions which are different for the different cases we are dealing with, and σ is the parameter characterizing the roughness of the surface, being $\sigma = 0$ the perfect surface.

Coupling to Perfect Metal Surfaces: As we know, the behavior of the light when it reaches a metal interface is described very well in terms of the dispersion relations of the Drude model $\epsilon(\omega)$. Which is introduced in the Fresnel coefficients by replacing $\epsilon^p = \epsilon^s = \epsilon(\omega)$ and $\sigma = 0$ in the expression Eq. (10).

Coupling to Non-Perfect Surfaces: In the case of nonuniform surfaces some changes in the Fresnel coefficients must be modified in order to have these effects into account [4, 6]. Here we use the dependence $\epsilon^p = \epsilon^s = \epsilon(\omega)$ and $\sigma \neq 0$.

Coupling to Metasurfaces: The vast majority of materials existing in nature has well-behaved properties,as we refer to their permeability and permitivity. If we can, by some mean, to put several small volumes, of the order of sub-wavelength, of a material inside another, and allow them to be distributed in any way inside the host, we can claim we have constructed metamaterial [1]. In this case we must replace in Eq. (10), the coefficients:

$$\epsilon^s = \epsilon(\omega)(1 - f) + f, \tag{12}$$

$$\epsilon^p = \epsilon(\omega)\frac{1 + f + \epsilon(\omega)(1 - f)}{1 - f + \epsilon(\omega)(1 + f)}. \tag{13}$$

Which depends on the packing fraction f, i.e. the volume fraction of material respect to the volume of the host. In Fig.1 we can se how the resonance in the LDOS for a metamaterial moves from right to left as the packed fraction f increases. This could be used to perform operations with multiple frequencies.

1.4 The Purcell Factor

The Purcell factor gives account for the decay rate enhancement or suppression for a nuclear magnetic dipole in the presence of different boundary conditions [7] and is defined by:

$$\beta = \frac{\Gamma}{\Gamma_0}. \tag{14}$$

Being the index 0 related to the decay rate in vacuum.

2 Conclusions

In summary, we use the concept of LDOS to extract the β-factor to evaluate the enhancement or suppression of the decay rate of an emitter into a plasmonic mode, and we investigate the LDOS variations versus the distance to interface at the resonance frequency condition.

Acknowledgments. The authors thank CONACYT for partial financial support R. C. thanks Basic Scientific Research, Grant No. A1-S-13587 and F. H. M. V. Cátedra CONACYT # 551.

References

1. Bukhari, S. S., Vardaxoglou, J., Whittow, W.: A metasurfaces review: definitions and applications. Applied Sciences, vol. 9, no. 13, pp. 2727 (2019) doi: 10.3390/app9132727
2. Carminati, R., Cazé, A., Cao, D., Peragut, F., Krachmalnicoff, V., Pierrat, R., Wilde, Y. D.: Electromagnetic density of states in complex plasmonic systems. Surface Science Reports, vol. 70, no. 1, pp. 1–41 (2015) doi: 10.1016/j.surfrep.2014.11.001
3. Chen, H., Chan, C. T., Sheng, P.: Transformation optics and metamaterials. Nature Materials, vol. 9, no. 5, pp. 387–396 (2010) doi: 10.1038/nmat2743
4. Davies, H.: The reflection of electromagnetic waves from a rough surface. In: Proceedings of the IEE - Part IV: Institution Monographs, vol. 101, no. 7, pp. 209–214 (1954) doi: 10.1049/pi-4.1954.0025
5. Khalid, A., Chung, K., Rajasekharan, R., Lau, D. W., Karle, T. J., Gibson, B. C., Tomljenovic-Hanic, S.: Lifetime reduction and enhanced emission of single photon color centers in nanodiamond via surrounding refractive index modification. Scientific Reports, vol. 5, no. 1 (2015) doi: 10.1038/srep11179
6. Lérondel, G., Romestain, R.: Fresnel coefficients of a rough interface. Applied Physics Letters, vol. 74, no. 19, pp. 2740–2742 (1999) doi: 10.1063/1.123999
7. Purcell, E. M., Torrey, H. C., Pound, R. V.: Resonance absorption by nuclear magnetic moments in a solid. Physical Review, vol. 69, no. 1-2, pp. 37–38 (1946) doi: 10.1103/physrev.69.37
8. Raether, H.: Surface plasmons on smooth and rough surfaces and on gratings. Springer Tracts in Modern Physics, vol. 111, pp 91–116 (1988) doi: 10.1007/bfb0048317
9. Shchegrov, A. V., Joulain, K., Carminati, R., Greffet, J. J.: Near-field spectral effects due to electromagnetic surface excitations. Physical Review Letters, vol. 85, no. 7, pp. 1548–1551 (2000) doi: 10.1103/physrevlett.85.1548

ISSN 1870-4069

Corneal Topography based on The Compact Conical Null-Screen for a Mobile Device and Single Board Computer

Luis Angel Pantoja-Arredondo[1], Manuel Campos-García[2], Juan Salvador Pérez-Lomelí[2], José Antonio Lechuga-Núñez[1], Oliver Huerta-Carranza[2], Víctor de Emanuel Armengol-Cruz[2]

[1] Universidad Nacional Autónoma de México, Facultad de Ciencias, Mexico

[2] Universidad Nacional Autónoma de México, Instituto de Ciencias Aplicadas y Tecnología, Mexico

langelpa@ciencias.unam.mx

Abstract. We evaluate a spherical reference surface, with a compact null-screen corneal topographer, which is powered by a coupled mobile device. Alternatively, it is shown that the corneal topographer can be designed by using a camera module and a single board computer.

Keywords: Corneal topography, null-screens, optical metrology, aspherical surfaces.

1 Null-Screen Test

To obtain the shape of human corneas we use a compact null-screen placed in front of the eye formed by an array of spots at $\mathbf{P}_1$ where light rays travel to the surface at $\mathbf{P}_2$ to be reflected by the cornea, the rays pass through an aperture and lens at **P** to finally arrive at the image plane on $\mathbf{P}_3$ (see Fig. 1) by a CCD/CMOS sensor. The optical system at **P** is used to focus the light rays on the sensor, the diaphragm is large enough for the test to be in the geometrical optics regime. Additionally, the lens can create some distortion at the obtained image that can be corrected.

1.1 Corneal Topography

To measure the cornea, we obtain an approximated normal field to the surface by joining the points on the null-screen and on the sensor with the incident and reflected rays:

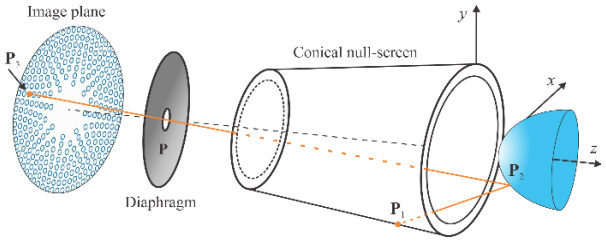

Fig. 1. Null-screen test for a surface.

$$\mathbf{N}_a = \frac{\mathbf{R}-\mathbf{I}}{|\mathbf{R}-\mathbf{I}|}. \tag{1}$$

The direction of the reflected vector is known $\mathbf{R}=\mathbf{P}_1-\mathbf{P}$ (see Fig. 2) and to obtain the incident vector we use a decentered and tilted reference surface such as:

$$z = \frac{r-\{r^2-Q[(x-x_0)^2+(y-y_0)^2]\}^{1/2}}{Q} + A(x-x_0)+B(y-y_0)+z_0, \tag{2}$$

where r is the radius of curvature, $Q=k+1$ where k is the conic constant, x_0, y_0 and z_0 are the decentering coordinates of the surface, A and B are the tilt.

The shape of the test surface can be obtained with the formula:

$$z - z_i = \int_{P_i}^{P_f} \sqrt{\left(\frac{n_x}{n_z}\right)^2 + \left(\frac{n_y}{n_z}\right)^2}\, d\rho, \tag{3}$$

where z_i is the sagitta for one point of the surface, and n_i ($i=x,y,z$) are the components of the normal field that was obtained in advance. This is an exact expression, and it is discretized using the trapezoidal rule for non-equally spaced data.

With the normal field we can obtain geometric parameters of the surface such as the radius of curvature and the conic constant by fitting the data to:

$$\eta \equiv \left(\frac{n_x}{n_z}\right)^2 + \left(\frac{n_y}{n_z}\right)^2 = \frac{x^2+y^2}{\left\{r_{fit}^2 - (k_{fit}+1)(x^2+y^2)\right\}^{\frac{1}{2}}}, \tag{4}$$

where r_{fit} is the vertex radius of curvature, k_{fit} is the conic constant.

2 Results

2.1 Calibration of the System

We used a compact conical null-screen powered by a mobile device's camera that captures the reflected pattern. The design parameters are given in table 1. We consider a spherical reference surface, a CMOS sensor with a sensitive area of 5.64 mm x 4.23

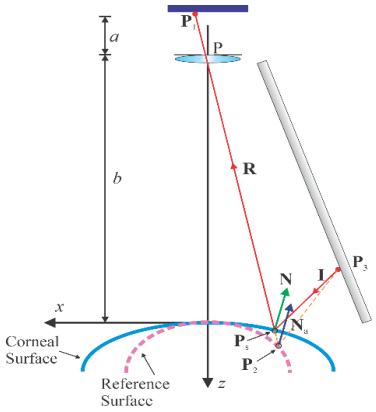

Fig. 2. Approximation of the normal field.

Table 1. Conical null-screen design parameters.

Element	Symbol	Size (mm)
Surface radii of curvature	*r*	7.8
Surface diameter	*D*	12
Camera lens focal length	*f*	4.2
Image diameter length	*d*	0.86
Diaphragm-Sensor distance	*a*	5.2
Diaphragm-Surface vertex distance	*b*	70
Cone height	*h*	85.50
Cone radius	*s*	16

mm (4032x3024 pixels) with a 4.2 mm focal length lens attached, and the morphology of the human face.

The alignment of the camera, corneal topographer, and test surface at the optical axis of the entire system is important to obtain reliable results.

To calibrate the system, we use a spherical reference surface with radius of curvature r=7.8 mm and effective diameter D=12 mm and calculate the center of mass for each detected spot on the sensor with an image-processing program (see Fig. 3).

Then, we placed a grid distortion test targets at 3.69 mm from the conical null-screen, i.e., where the reflected image is formed to measure their radial distances on the grid and on the sensor to obtain the transverse magnification and radial distortion of the lens by fitting (see Fig. 4):

$$\rho_o = \frac{\rho_d}{M_T} - \frac{E}{M_T^4}, \tag{5}$$

where ρ_o is the object radial size, ρ_d is the radial distorted image, M_T is the transverse magnification and E is the lens radial distortion. This last parameter allows to correct the image and obtain more accurate data.

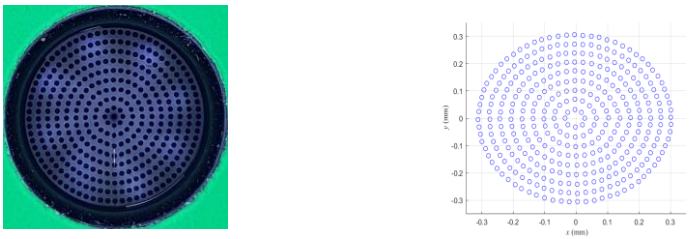

(a) (b)

Fig. 3. a) Reflected null-screen on the reference surface, b) calculated centroids.

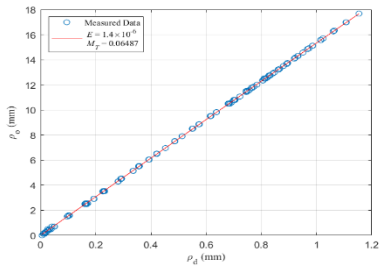

Fig. 4. Fit of the lens radial distortion.

Table 2. Values recovered analyzing the corneas as aspherical surfaces.

Surface	*r* (mm)	*k*	x_o (mm)	y_o (mm)	z_o (mm)	*A*	*B*
Reference Sphere	7.81	0.02	0.13	0.04	2.62	0.0145	0.0036
Right Cornea	7.84	-0.76	-2.18	1.74	2.57	-0.1593	0.2484
Left Cornea	7.89	-0.91	1.50	4.68	4.40	0.0561	0.5796

After distortion correct the data, we obtain the elevation map for a reference surface with the best fit surface (see Fig. 5a) and obtained its geometrical parameters using Eq. 2 (see Table 2 first row) where we notice the radius of curvature to be *r*=7.81 mm that has an error of 0.13% compared to the design value.

After calibration, we obtained the same map (see Fig. 5b and 5c) and parameters for two human corneas, and the *rms* difference of sagitta. In Table 2 we show the recovered radius of curvature and conic constant for each surface.

We notice that for every map the *rms* difference un sagitta is about some μm which can be compared to those of commercial topographers of about 5-10 μm.

2.2 Corneal Topography with a Single Board Computer

The compact corneal topographer can be adapted to couple a camera module of a Single Board Computer (SBC) and obtain high quality images (see Fig. 6). The camera has a 3.68 mm x 2.76 mm (3280 x 2464 pixels) sensor image area, and a 3.60 mm focal length. Due to its small size and focal length it has to be focused manually which makes it hard to focus at the required distance.

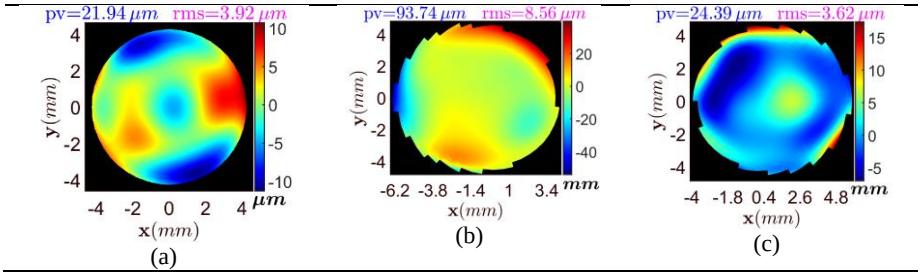

Fig. 5. Elevation maps for: a) reference surface, b) right cornea, c) left cornea.

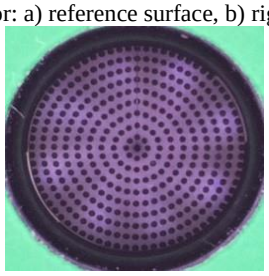

Fig. 6. Reflected pattern detected by the camera module.

The same methodology mentioned before can be applied for this device, and the lens radial distortion can be measured to correct the reflected image and obtain the corneal topography.

3 Conclusions

The compact corneal topographer can be used by any small device. We recovered some geometrical parameters with high accuracy of a reference surface and two human corneas. We need to calibrate this device by aligning the entire system, measuring the lens radial distortion and by obtaining the shape of a reference surface, in our case we used a sphere with radius of curvature r=7.8 mm and recovered a value with 0.13% error. The use of an SBC for a compact conical null-screen corneal topographer can improve the design of a new device due to its portability and easy programming.

References

1. Campos-García, M., Aguirre-Aguirre, D., Pérez-Lomelí, J. S., Peña-Conzuelo, A.: Design of a compact corneal topographer to characterize the shape of the cornea. In: Proceedings of Volume 11352, Optics and Photonics for Advanced Dimensional Metrology, vol. 113521A (2020) doi: 10.1117/12.2556052
2. Campos-García, M., Aguirre-Aguirre, D., Lechuga-Núñez, J. A., Peña-Conzuelo, A.: Design of a null-screen compact corneal topographer. Modeling Aspects in Optical Metrology VII, vol. 110570I (2019) doi: 10.1117/12.2526241
3. Huerta-Carranza, O.: Desarrollo de un algoritmo para corregir los errores en topografía corneal debido a desalineaciones. Master's Thesis, Universidad Nacional Autónoma de México (2017)

ISSN 1870-4069

Optical Device for Liquid Injection into Skin Phantoms based on Thermocavitation

Doris Giovanna Mitre-Martínez[1], Rafael Zaca-Morán[2], Placido Zaca-Morán[1], Juan Castillo-Mixcóatl[2], Carolina Morán-Raya[1], Julio César Ramírez-San-Juan[3], Rubén Ramos-García[3], Juan Pablo Padilla-Martínez[1]

[1] Benemérita Universidad Autónoma de Puebla, Instituto de Ciencias, Mexico

[3] Instituto Nacional de Astrofísica, Óptica y Electrónica, Departamento de Óptica, Mexico

juan.padilla@correo.buap.mx, giovanna.dgmm17@gmail.com

Abstract. In this work, an optical device was developed for the injection of liquids jets into skin phantoms based on the phenomenon of thermocavitation. Vapor bubbles were generated by a continuous wave laser inside a truncated elliptical cavity (12 mm major axis and 6 mm minor axis), which contains a highly absorbent solution (α=135 cm^{-1}) at the laser operating wavelength (980 nm). The cavity was designed in SolidWorks and manufactured on a 3D printer with a polymeric material. The generated bubble grows inside the cavity and later it collapses emitting an intense acoustic wave, which is concentrated in the upper part of the cavity, expelling a liquid jet at a velocity of ~85 m/s, through an exit channel (250 µm of radio and 200 µm of height). Penetration tests were performed on agar gels at a concentration of 1.0% and visualized using a fast camera (35000 fps). The maximum penetration depth was ~2.9 mm, after 6 liquid jets hit the sample.

Keywords: Thermocavitation, injection, needle free.

1 Introduction

According to the World Health Organization (WHO), it is estimated that around 12 billion injections are administered per year, and it is calculated that of all the waste (syringes/needles) generated by these activities, approximately 85% is non-hazardous waste, but they require special protocols for their correct disposal [1]. Situation that has become even more complex in recent years, caused by the global vaccination campaign against COVID-19.

Due to the above, there is a greater interest in the research and development of technology related to the generation of liquid jets for the administration of drugs

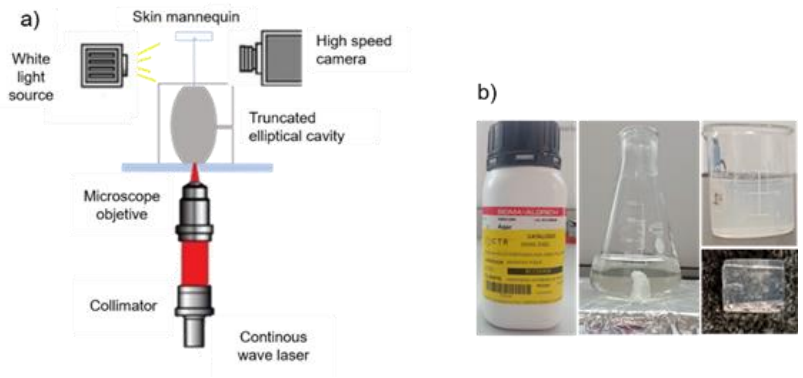

Fig. 1. a) Experimental setup. b) Images of the steps to obtain the agar gel.

without the use of a conventional needle. In recent years, high speed liquid jet injection has been studied through optical methods, using pulsed lasers (optical cavitation) [2] and continuous wave lasers (thermocavitation) [3, 4].

Thermocavitation is defined as the process of formation, growth and collapse of a vapor bubble within a highly absorbent solution [3]. The generation and expulsion of liquid jets from the phenomenon of thermocavitation is usually carried out due to the expansion and collapse of a thermocavitation bubble [5]. In this work a new optimized device was designed (SolidWorks), built (3D printer) and validated for the injection of liquid jets into agar gels, usually used as skin phantoms due to their biomechanical properties like human skin.

2 Experimental Setup

A beam from a continuous wave laser (λ=980 nm) is focused down with a microscope objective with optical distance of 8 mm (beam waist of 480 µm at focus) into an elliptical cavity filled with a saturated solution of copper nitrate (13.78 g of $Cu(NO_3)_2$ per 10 ml of water). The absorption coefficient of the solution is α=135 cm^{-1} In order to record the formation and evolution of an individual bubble, the was illuminated using a white light source to project the bubble´s shadow on a high-speed video camera (Phantom VEO 710L), which was used to capture 35,000 images in one second at a resolution of 320 x 504 pixels (See Fig. 1a).

Skin phantoms were placed 5 mm from the device's ejection channel. All the videos obtained were analyzed in the "Phantom Camara Control Application" software. For the preparation of the skin phantoms, agar gel (Sigma Aldrich,) was used at a concentration of 1.0%. That is, 1 g of agar powder is dissolved in 100 ml of water. After solidification, pieces of agar were obtained with an approximate size of 3 cm long by 3 cm wide and 0.5 cm thick, as observed in Fig. 1b.

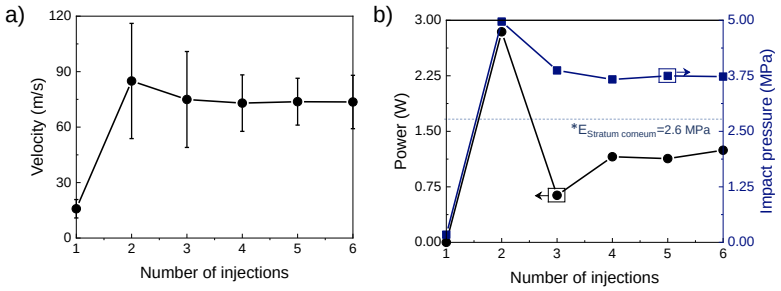

Fig. 2. a) Average speed, b) Power and impact pressure of the 6 ejected jets.

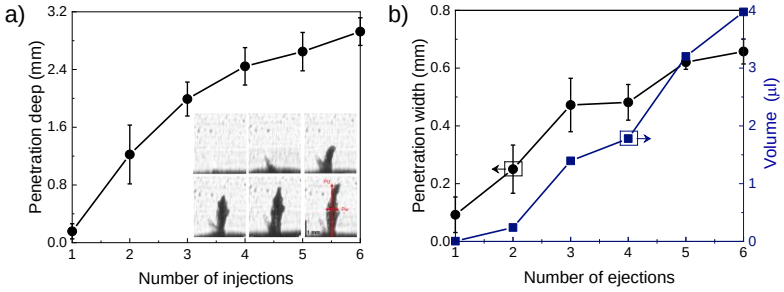

Fig.3. a) Penetration depth, b) Penetration width and volume delivered by the 6 liquid jets.

3 Results

In this work, penetration tests were carried out under the same experimental conditions in triplicate. Initially, the solution is irradiated at a power of 400 mW for a time of approximately 1s. With the help of the fast camera, it was possible to study the dynamics of the first 6 ejected liquid jets, as shown in Fig. 2. Maximum velocity (~85 m/s), power (~2.84 W) and impact pressure (~ 4.97 MPa) are presented in the second ejected jet.

In Fig. 2b shows the impact pressure of the ejected liquid jet when it hits the surface of the gel, value that indicates if the liquid jet has sufficient capacity to penetrate the different layers of the skin. According to the literature, it has been reported that the pressure required to break the stratum corneum is ~2.6 MPa, while only a value of ~1.1 MPa is required to break the epidermis [6].

In Fig. 3a it is shown the penetration depth reached after each ejected liquid jets, reaching the depth of ~2.9 mm at the sixth shot. Fig. 3b shows the value of the estimates of the penetration width and the volume of liquid injected by the device (approximately ~ 4 µl), as a function of the number of shots.

Fig. 4a shows the evolution of penetration of the 6 liquid jets inside the skin phantom at a concentration of 1.0%. The liquid injected into the sample occurs until the second shot (Fig. 4b), hence the penetration depth is progressive as the number of shots increases, until reaching a maximum penetration distance (see Fig. 4f).

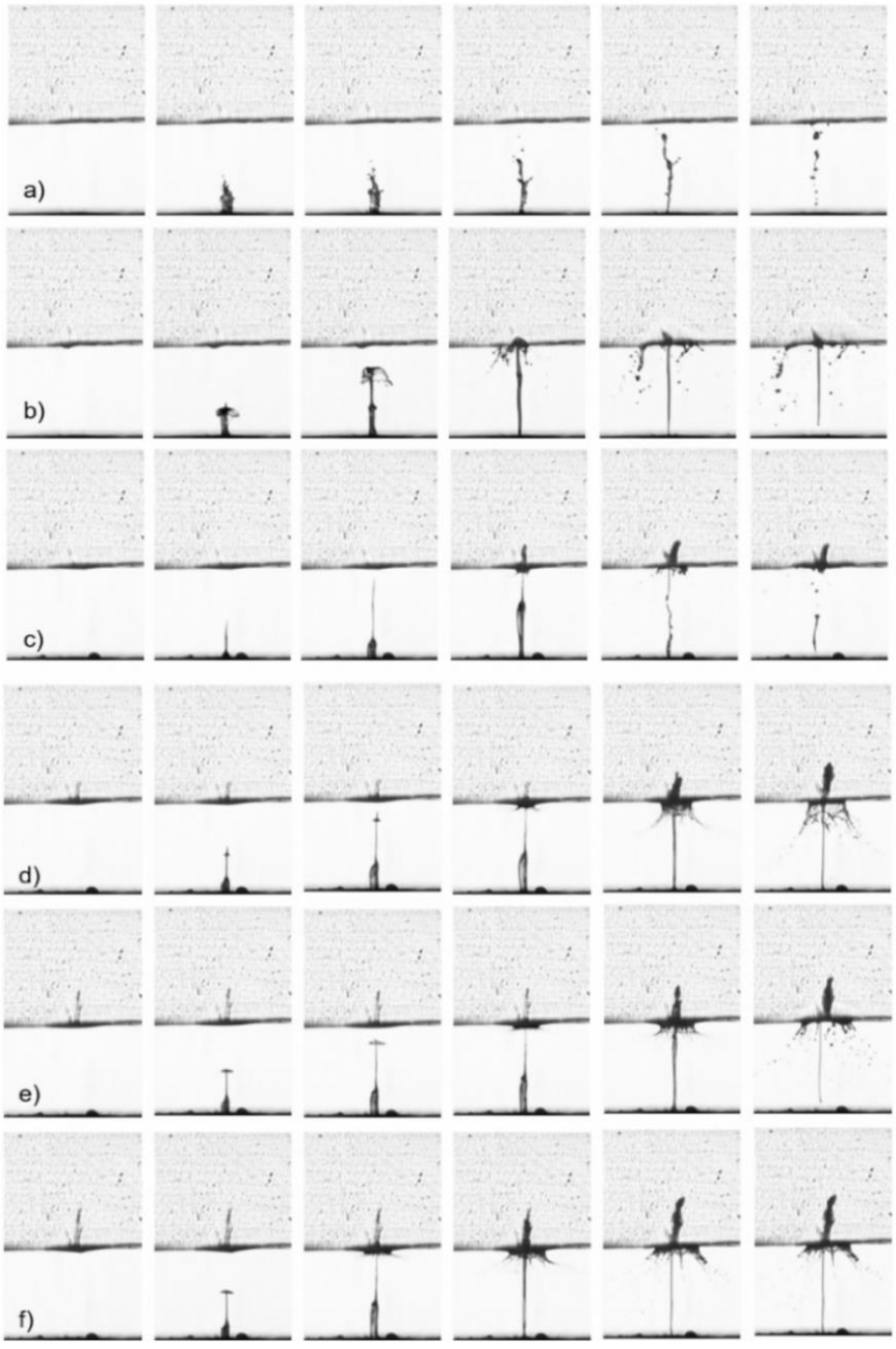

Fig. 4. Evolution of the penetration dynamics of liquid jets in agar gel at 1.0%. a) first shot, b) second, c) third, d) fourth, e) fifth and f) sixth shot.

4 Conclusions

A microfluidic device was developed with the ability to eject liquid jets at high speeds that can reach and exceed 85 m/s, caused by the high concentration of the kinematic energy of an acoustic wave emitted after the collapse of the thermocavitation bubble. The liquid jets generated can penetrate skin phantoms made from agar gel at a concentration of 1.0%, achieving a penetration distance of ∼2.9 mm and a delivered volume of ~ 4 µl at the sixth shot. It is also reported that the maximum power (2.84 W) and impact pressure (4.97 MPa), a value that allows us to compare the efficacy of the microfluidic device with those already reported in the literature, this being a good option for the administration of drugs free of needles.

References

1. Mitragotri, S.: Current status and future prospects of needle-free liquid jet injectors. Nature Reviews Drug Discovery, vol. 5, no. 7, pp. 543–548 (2006) doi: 10.1038/nrd2076
2. Han, T. H., Yoh, J. J.: A laser based reusable microjet injector for transdermal drug delivery. Journal of Applied Physics, vol. 107, no. 10, pp. 1–4 (2010) doi: 10.1063/1.3430989
3. Padilla-Martinez, J. P., Berrospe-Rodriguez, C., Aguilar, G., Ramirez-San-Juan, J. C., Ramos-Garcia, R.: Optic cavitation with CW lasers: A review. Physics of Fluids, vol. 26, no. 12, pp. 16–20 (2014) doi: 10.1063/1.4904718
4. Cu, K., Bansal, R., Mitragotri, S., Fernandez-Rivas, D.: Delivery strategies for skin: comparison of nanoliter jets, needles and topical solutions. Annals of Biomedical Engineering, vol. 48, no. 7, pp. 2028–2039 (2020) doi: 10.1007/s10439-019-02383-1
5. Zaca-Morán, R., Castillo-Mixcóatl, J., Sierra-González, N. E., Pérez-Corte, J. M., Zaca-Morán, P., Ramírez-San-Juan, J. C., Ramos-García, R., Padilla-Martínez, J. P.: Theoretical and experimental study of acoustic waves generated by thermocavitation and its application in the generation of liquid jets. Optics Express, vol. 28, no. 4, pp. 4928–4937 (2020) doi: 10.1364/OE.375900
6. Geerligs, M., van Breemen, L., Peters, G., Ackermans, P., Baaijens, F., Oomens, C.: In vitro indentation to determine the mechanical properties of epidermis. Journal of Biomechanics, vol. 44, no. 6, pp. 1176–1181 (2011) doi: 10.1016/j.jbiomech.2011.01.015

ISSN 1870-4069

Optical Switching by Thermocavitation for the Implementation of an All-Fiber Pulsed Laser

Rafael Zaca-Morán[1], Placido Zaca-Morán[2], César Amaxal-Cuatetl[2], Juan Castillo-Mixcóatl[1], Rubén Ramos-García[3], Juan Pablo Padilla-Martínez[2]

[1] Benemérita Universidad Autónoma de Puebla, FCFM, Mexico

[2] Benemérita Universidad Autónoma de Puebla, Instituto de Ciencias, Mexico

[3] Instituto Nacional de Astrofísica, Óptica y Electrónica, Departamento de óptica, Mexico

juan.padilla@correo.buap.mx

Abstract. A new optical switching for the generation of laser pulses based on the phenomenon of thermocavitation is reported. Thermocavitation bubbles were induced within a glass cuvette filled with a saturated solution of copper nitrate dissolved in water. Two optical fibers were submerged into the solution, very close to the region where the vapor bubble was generated. Once the bubble is generated it expands rapidly and the incoming laser light transmitted through the optical fiber is reflected at the vapor-solution interface and reflected into the fiber, which is coupled to an erbium-doped fiber ring laser and the laser pulse was extracted from the ring cavity and detected by a fast photodetector. The generation of the laser pulses is based on the change of the optical reflection coefficient at the end surface of the glass fiber by the expansion and collapse of the bubble, which behaves like a mirror with variable reflectivity. For both pulses, the repetition rate obtained was in a range of 118 Hz to 2 kHz at 1560 nm, with a pulse width ranging from 64 to 57 μs, which can be controlled by adjusting the laser power to in-duce thermocavitation bubbles.

Keywords: Optical switch, thermocavitation bubbles, pulsed laser.

1 Introduction

The basic scheme of a resonator for a fiber optic laser is the linear scheme, where the mirrors are deposited at the ends of the fiber [1]. But there are also resonators in ring configuration without mirrors, instead a coupler is used as the output port to extract the light emitted [2]. The modulation techniques for the generation of light pulses can be carried out in two different ways: i) Q-switching [2] and ii) Mode-Locking switching [3] which are divided in active and passive methods. In active methods the losses are

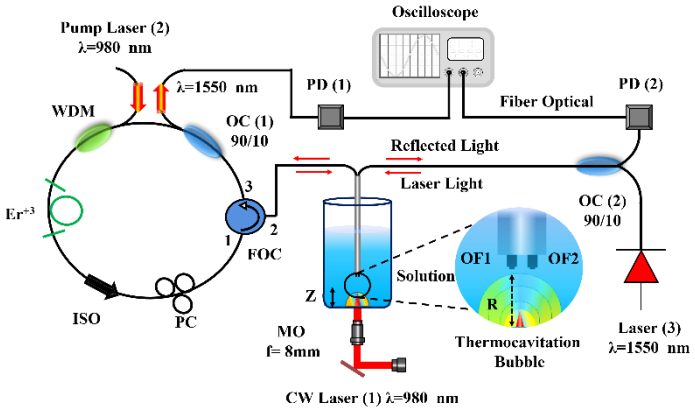

Fig.1. Scheme of the thermocavitation-based pulsed laser and experimental setup known as a fiber optic hydrophone (FOH).

modulated with elements external to the cavity with a control element [4] and passive methods, referring to internal elements that automatically modulate losses [5].

The phenomenon of thermocavitation is present when a highly absorbent solution is irradiated with a continuous wave (CW) laser. Where the absorbed light heats the solution to its critical limit, that is, the temperature at which an explosive liquid-gas phase transition occurs [6,7].

The precise moment when superheated water explosively turns into steam, producing a rapidly expanding bubble, which finally collapses, emitting an acoustic wave. In this work, it is precisely the growth dynamics of the thermocavitation bubble the main factor that causes the losses and the control of the laser cavity, acting as a mirror of variable reflectivity in time.

2 Experimental Setup

The thermocavitation is generated by a CW near infrared laser with λ = 980 nm (Laser (1)) where the output beam is collimated, reflected, and focused with a microscope objective (f = 8 mm) into the saturated solution of copper nitrate (13.78 g per 10 ml of water) which is contained inside a glass cuvette as shown in Fig. 1.

To carry out the generation of light pulses, the experimental setup of a pulsed all-fiber laser in a ring configuration with a total length of ~ 42 meters was used, see Fig. 1 (left section). The system was pumped by an LDC 205C laser with a wavelength λ = 980 nm (Laser 2), used 12 m of single-mode optical fiber doped with erbium as active medium, an WDM (NPM07000165), isolator (M11 / 81202003), polarization controller (FPC030) and an circulator (FOC) (S/N: A8038188), where the Port 1 of the FOC is connected to the laser cavity, while the optical fiber coming from port 2 was cleaned, cut, and introduced into a metal tube and subsequently, immersed in the working solution, close to the region where thermocavitation is created.

Consequently, the light reflected inside the fiber enters the circulator again through the same port 2 and exits through port 3, which is connected to a 90/10 optical coupler

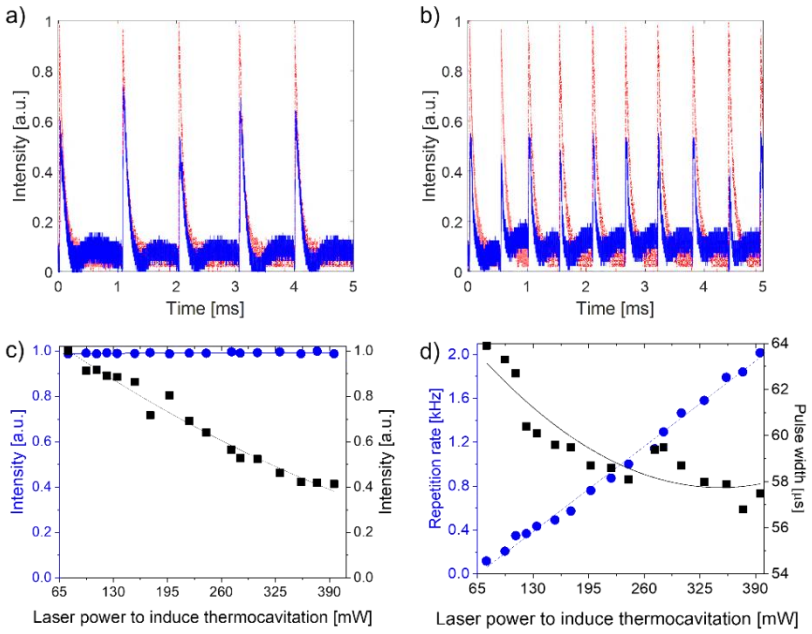

Fig. 2. Light pulses at the exit of the laser cavity (Red-Dotted) and the acoustic hydrophone (Blue-Continuous) varying the power to induce thermocavitation bubbles. a) 282 mW and b) 375 mW. c) Variation of intensities of the pulses extracted from the laser cavity (Blue-Circles) and those from the FOH (Black-Square), as well as in d) The repetition frequency (Blue-Circles) and the temporal width of the pulse (Square-Black) varying the power to induce thermocavitation.

(CWD07014557) (OC (1)) to close the laser cavity, where only 10% of the energy is extracted in the form of pulses, which were analyzed with the help of a photodetector (PD (1)) and observed with an oscilloscope.

The right section of the experimental setup corresponds to the well-known fiber optic hydrophone (FOH) see Fig. 1 [8], which was implemented in this work in order to verify that each pulse at the output of the pulsed all-fiber laser corresponded to a single thermocavitation event. The experimental setup uses an infrared laser with a wavelength of λ = 1550 nm (Laser 3), sending the light beam to a 90/10 coupler (CWD07014557) (OC (2)) where 90% of the light is sent to port one.

Simultaneously both fibers (OF1 and OF2) detect the change in refractive index due to the glass-vapor interface caused by the growth of the thermocavitation bubble, which expands rapidly, causing the laser light to incoming transmitted through it is reflected.

3 Results

Figure 2 (a, b) shows the temporal characteristics of pulses, here the optic fiber laser (Red-Dotted) and the pulses detected by the fiber optic hydrophone (Blue-Continuous), were measured as a function of the laser power to induce thermocavitation (282 y 375 mW), using a power pump 235 mW to the laser ring.

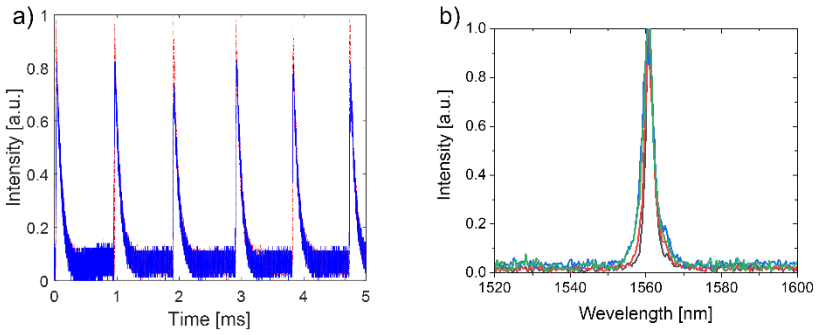

Fig. 3. a) Pulses at the output of the fiber optic laser (Red-Dotted) and the FOH (Blue-Continuous) at the pumping power of 272 mW. b) Spectra of the pulses at the exit of the cavity.

Both signals were observed simultaneously on the same oscilloscope, each pulse captured by the photodetector corresponds to a single thermocavitation event.

In the Fig. 2c shows the variation of normalized intensities captured by the oscilloscope of the pulses at the exit of the laser cavity (Blue-Circles), which remain practically constant. As well as the signals captured by FOH (Black-Boxes) which tend to decay, both signals detected as a function of the variation of the power to induce thermocavitation from 75 mW to 395 mW.

In Fig. 2d the repetition rate of the light pulses detected by the PD (1) that corresponds to the output of the laser cavity, which increases from 118 Hz to 2 kHz (Circles-Blue). while the temporal width decreases moderately from 64 to 57 μs (Squares-Black) both characteristics depending on the laser to induce thermocavitation.

To observe the variation of the temporal characteristics of the cavity output pulses when the pumping power is varied, the laser power to induce thermocavitation was set at 272 mW, as well the focusing distance $Z = 30$ μm.

Fig. 3a shows the temporary traces of the pulses at the exit of the cavity (Red-Dotted) and those detected by FOH (Blue-Continuous) at a pumping power of 199 mW, it was noted that the amplitude and the frequency is practically constant to the changes of variation in the bass drum power, so there is no need to show more sequences of pulses, the only alteration that the pulses present is in the temporal width with a decrease from 69 to 60.4 μs. In Fig. 3b the output spectrum is shown, which is centered 1560 nm. More in detail about the pulses at the laser output, see the reference [9].

4 Conclusions

In this paper, we present a mechanism for the generation of laser pulses using the phenomenon of thermocavitation. Thermocavitation is due to the high laser light absorption by a homogeneous solution at a specific wavelength, which enables the focal point to reach superheated conditions (~300º C). Here, vapor bubbles were induced using a CW laser at 980 nm (which is an inexpensive energy source) focused into a saturable solution of copper nitrate dissolved in water. Here the losses are caused by time-varying reflectivity due to the dynamic growth of a thermocavitation bubble.

These reflectivity changes are detected by an optical fiber, which is coupled to a simple erbium-doped fiber ring laser. The amplitude of the laser pulses is greater and constant when they pass through the ring cavity, compared what the pulse is obtained from the fiber optic hydrophone setup. Control over the pulse repetition rate is realized by adjusting the laser power to induce thermocavitation, obtaining a repetition rate from 118 Hz to 2 KHz, with a pulse width that change from 64 to 57 μs.

References

1. Yin, S., Ruffin, P. B., Francis, T. S.: Fiber optic sensors. CRC Press (2017)
2. Álvarez-Tamayo, R. I., Durán-Sánchez, M., Pottiez, O., Ibarra-Escamilla, B., Kuzin, E. A., Espinosa-Martínez, M.: Active Q-switched fiber lasers with single and dual-wavelength operation. Optical Fiber Technology (2016)
3. Shen, Y., Wang, Y., Zhu, F., Ma, L., Zhao, L., Chen, Z., Wang, H., Huang, C., Huang, K., Feng, G.: 200 μJ, 13 ns Er: ZBLAN mid-infrared fiber laser actively Q-switched by an electro-optic modulator. Optics Letters, vol. 46, no. 5, pp. 1141–1144 (2021) doi: 10.1364/OL.418950
4. Zaca-Morán, P., Ortega-Mendoza, J. G., Lozano-Perera, G. J., Gómez-Pavón, L. C., Pérez-Sánchez, G. F., Padilla-Martínez, J. P., Felipe, C.: Passively Q-switched erbium-doped fiber laser based on Zn nanoparticles as a saturable absorber. Laser Physics, vol. 27, no. 10, pp. 105101 (2017) doi: 10.1088/1555-6611/aa83e0
5. Ramirez-San-Juan, J. C., Rodriguez-Aboytes, E., Martinez-Canton, A. E., Baldovino-Pantaleon, O., Robledo-Martinez, A., Korneev, N., Ramos-Garcia, R.: Time-resolved analysis of cavitation induced by CW lasers in absorbing liquids. Optics Express, vol. 18, no. 9, pp. 87358742 (2010) doi: 10.1364/OE.18.008735
6. Padilla-Martinez, J. P., Berrospe-Rodriguez, C., Aguilar, G., Ramirez-San-Juan, J. C., Ramos-Garcia, R.: Optic cavitation with CW lasers: A review. Physics Fluids, vol. 26, no. 12, pp. 122007 (2014) doi: 10.1063/1.4904718
7. Arvengas, A., Davitt, K., Caupin, F.: Fiber optic probe hydrophone for the study of acoustic cavitation in water. Review of Scientific Instruments, vol. 82, no. 30 (2011) doi: 10.1063/1.3557420
8. Zaca-Morán, R., Amaxal-Cuatetl, C., Zaca-Morán, P., Castillo-Mixcóatl, J., Ramos-García, R., Padilla-Martínez, J. P.: Thermocavitation: a mechanism to pulse fiber lasers. Optics Express, vol. 29, no. 15, pp. 23439–23446 (2021). doi: 10.1364/OE.430319

ISSN 1870-4069

Spatio-Spectro-Temporal Characterization of Ultrashort Vortex Pulses

Erick R. Baca-Montero, Oleksiy V. Shulika

Universidad de Guanajuato,
Departamento de Ingeniería Eléctrica,
Mexico

{er.bacamontero, oshulika}@ugto.mx

Abstract. Due to the promising features of optical vortices a variety of methods have been developed for their generation, however, these methods are mostly intended for CW vortex beams and thus can be hardly usable for generation of ultrashort vortex pulses. A spiral phase plate (SPP) is a robust method for vortex generation with potential to be used in ultrafast optics, however, the resulting vortex is not a pure vortex mode but contains contributions of different radial orders. As well, the SPP exhibits a wavelength-dependent phase shift, due to its material dispersion. Here we present a (3+1)D numerical analysis of the spatio-spectro-temporal properties of ultrashort vortex pulses generated with spiral phase plates characterizing the effects of material dispersion and propagation geometry. These results can serve as a basis for the design of new passive and active devices for singular optics and photonics.

Keywords: Spatio-spectro-temporal characterization, ultrashort vortex pulses, spiral phase plate (SPP), laguerre–gaussian (LG) modes, material dispersion.

1 Introduction

Ultrashort vortex pulses are electromagnetic radiation with durations in the order of picoseconds or less (broadband optical spectrum) and that present points where the intensity of the wave is zero around the axis of the beam and the phase is undefined [1]. In recent years the study of vortex pulses has peaked due to their promising features in super-resolution microscopy [7], optical tweezers [6], ultra-fast optical communications [3], quantum computing [9] and astrophysics [4]. Laguerre–Gaussian (LG) modes are the most commonly studied set of vortices. They are derived by solving the paraxial Helmholtz equation in cylindrical coordinates [1]. An LG pulse is given by:

$$u_{p,l}^{LG}(r,\phi,z,t) = \underbrace{\frac{C_{lp}^{LG}}{w(z)}\left(\frac{r\sqrt{2}}{w(z)}\right)^{|l|} L_p^{|l|}\left(\frac{2r^2}{w^2(z)}\right) e^{-\frac{r^2}{w^2(z)}} e^{\frac{-ikr^2}{2\left(z^2+z_R^2\right)}} e^{-il\phi} e^{(i(2p+l+1)\psi)}}_{\text{Laguerre Gaussian Mode Factor}} \underbrace{e^{\frac{-(t-t_0)}{\tau^2}} e^{i\omega_t t}}_{\text{Temporal Profile factor}}. \quad (1)$$

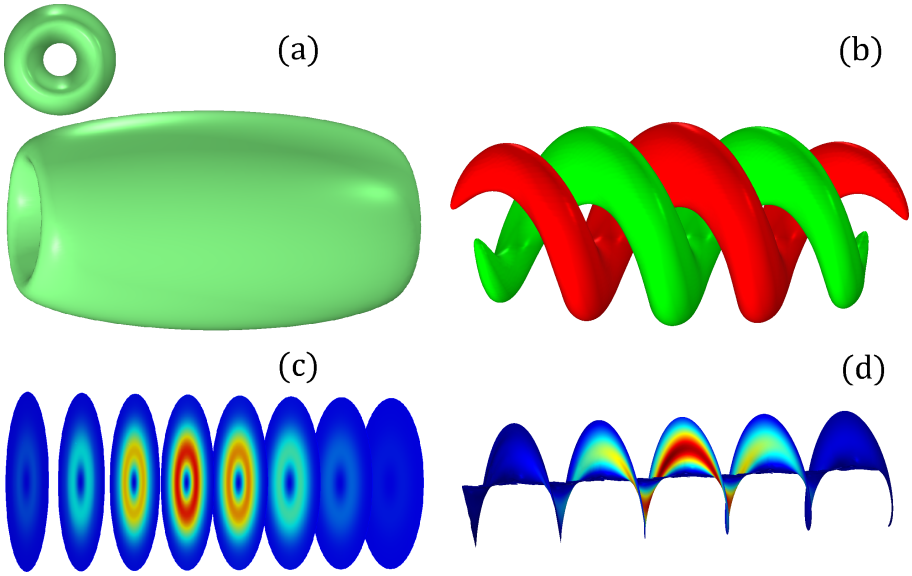

Fig. 1. 3D vortex pulse $LG_{0,1}$ with a duration $\tau = 5\,\text{fs}$: (a) Spatio-temporal intensity profile isosurface set at half of the peak intensity. (b) Isosurfaces of the real part of the complex field. (c) Slices of the characteristic doughnut spatial intensity profile of the vortex pulse along. (d) Isosurface of the spiraling phase of the vortex pulse.

Here w_0 is the beam radius at the beam waist, r is the radial distance from the center axis of the beam, z_R is the Rayleigh range, ψ is the Gouy phase, $R(z)$ is the radius of curvature, C_{lp}^{LG} is a normalization constant [1], $L_p^{|l|}$ is the generalized Laguerre polynomial of order p and l, and $w(z)$ is the radius of the beam at a given position z, l is called topological charge and it defines the azimuthal distribution (the amplitude has azimuthal angular dependence, $e^{-il\phi}$) that can be positive or negative indicating left or right circulation, while p defines the radial distribution index.

In the temporal factor τ is the duration of the pulse, t_0 is the pulse center time and ω_t is the central angular frequency. A LG mode retains its intensity profile upon propagation, although with a different width and the Gouy phase changes by multiples $(2p + |l| + 1)\pi/2$ as it travels. For $l = 0$, $p = 0$, the expression eq. 1 reduces to that of an ordinary Gaussian beam, as $L_p^{|l|} = 1$. Because l is an integer, the phase of the field can only increase or decrease by multiples of 2π as one follows a closed path around the axis of the beam.

The radial distribution p gives a number of dark rings nested in the beam profile. Figure 1 shows a three-dimensional reconstruction of the vortex pulse $LG_{0,1}$ with a duration $\tau = 5\,\text{fs}$ The characteristic zero intensity point at the vortex axis can be observed in figures 1 (a) and (c) which show the spatio-temporal intensity profile $|u(x, y, t)|^2$ and slices through the centre of the beam, respectively. The spiraling nature can be observed in figures 1 (b) and (d) which show isosurfaces of the real part of the complex field, $\Re\,|u(x, y, t)|$ and of the phase (Here the color scale shows the spatio-temporal intensity profile of the vortex pulse along spiraling phase).

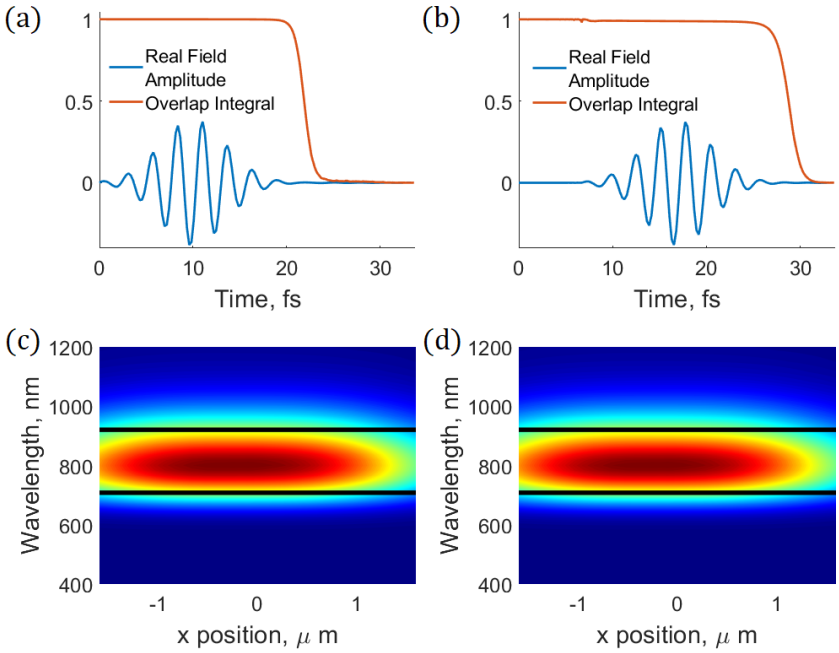

Fig. 2. Spatio-spectro-temporal properties of a vortex pulse upon dispersive propagation in 2λ long SiO_2 block: (a) Real field amplitude of the input vortex pulse and overlap integral (b) Real field amplitude of the vortex pulse and overlap integral after propagation (c) Spatially resolved spectral intensity of the input vortex pulse. (d) Spatially resolved spectral intensity of the output vortex pulse.

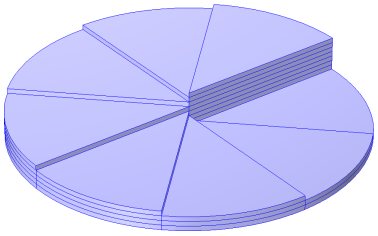

Fig. 3. Schematic of a 8-levels discrete SPP.

2 Ultrashort OVs Spatio-Spectro-Temporal Characterization During Propagation and Generation with a Spiral Phase Plate

In this work, the propagation and generation of ultrashort vortex pulses is analyzed using control parameters calculated at the input and output of the model domain, these are the real field value of the electric field, the electric field intensity, the spatially resolved spectral intensity and OI_I the overlap integral between the amplitude of the analytic LG01 mode (eq. 1) and its numerical counterpart (u_{num}).

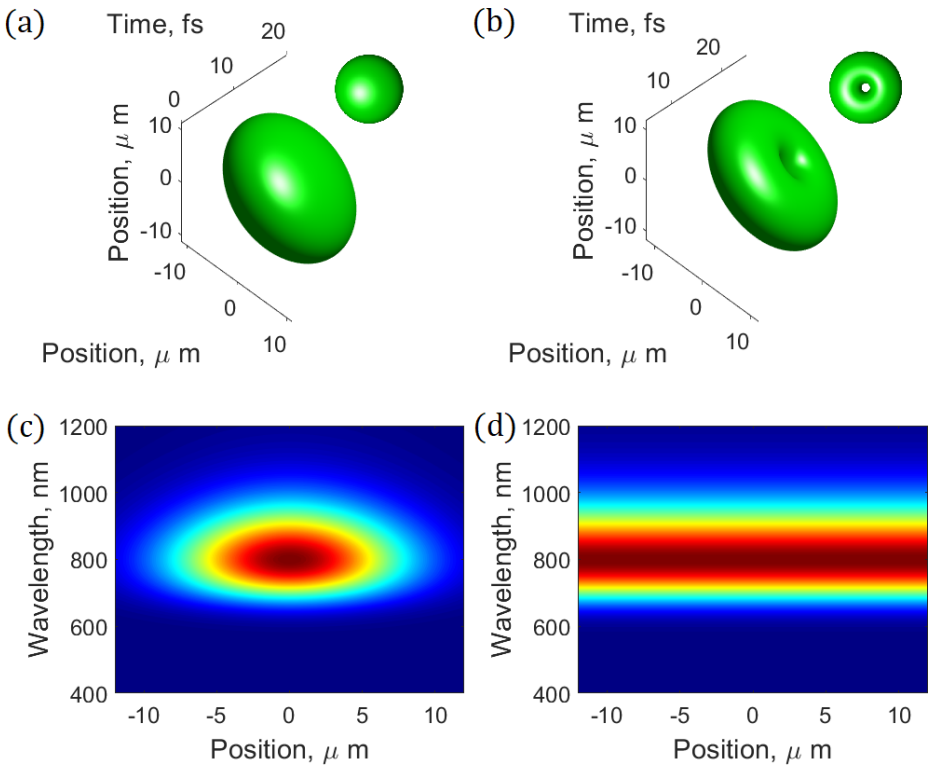

Fig. 4. Spatio-spectro-temporal properties of input pulse to a SPP and of the generated vortex pulse: (a) Spatio-temporal intensity profile isosurface set at half of the peak intensity of the input gaussian pulse. (b) Spatio-temporal intensity profile isosurface set at half of the peak intensity of the generated vortex pulse. (c) Spatially resolved spectral intensity of the input gaussian pulse. (d) Spatially resolved spectral intensity of the generated vortex pulse.

The overlap integral is given as:

$$OI_I = \frac{\left| \int u_{0,1}^{\mathrm{LG}} * u_{\mathrm{num}} dA \right|^2}{\int \left| u_{0,1}^{\mathrm{LG}} \right|^2 dA \int \left| u_{\mathrm{num}} \right|^2 dA}. \tag{2}$$

And it gives the quality of vortex modes [2].

2.1 Propagation of Ultrashort Vortex Pulses in Dispersive Media

The characteristics of a $5\,\mathrm{fs}$ vortex pulse of wavlength $\lambda = 800\,\mathrm{nm}$ upon propagation in a dispersive SiO_2 block of thickness $t = 2\lambda$ are studied. The refractive index of the SiO_2 is given in [5]. Fig. 2 (a) and (b) show the real field amplitude and the overlap integrals (eq. 2) of the vortex before and after propagation, small temporal chirp is acquired (less than $1\,\mathrm{fs}$), while the spatial spectral intensity measured along a line at the

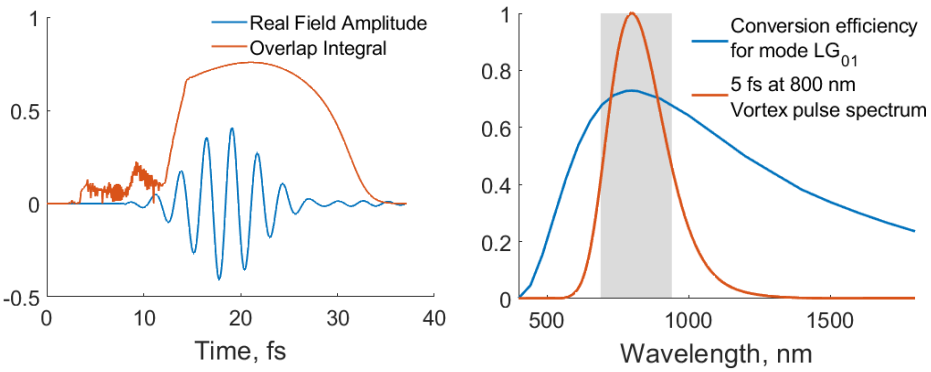

Fig. 5. (a) Temporal real field amplitude and overlap integral between analytic LG_{01} mode (eq. 1) and generated ultrashort vortex pulse. (b) Conversion efficiency dependence in wavelength for an 8-levels SPP and spectrum of a $5\,\mathrm{fs}$ vortex pulse at $\lambda = 800\,\mathrm{nm}$.

left side maximum of the vortex 2 (c) and (d) before and after propagation respectively, shows that the spectrum half amplitude remains constant and therefore the vortex does not present spatial chirp, furthermore, it is then possible to compensate for the time chirp through normal dispersion compensation techniques, as also shown in [8].

2.2 Ultrashort Vortex Generation with a Spiral Phase Plate

A Spiral Phase Plate (SPP) [2] is an optical component for the generation of vortex beams. In this device with refractive index n the optical thickness t is varied with an azimuthal angle ϕ according to:

$$t = \phi l \lambda / 2\pi (n - n_b), \tag{3}$$

where λ is the incident beam wavelength and n_b is the refractive index of the medium containing the SPP. Fig. 4 shows the spatio-spectro-temporal properties of the vortex pulse generated with an 8-levels SPP (fig. 3), the spectrum half amplitude (fig. 3 (c) and (d)) remains constant for the input gaussian pulse and the generated vortex pulse, thus there is no spatial chirp.

The SPP has maximum conversion efficiency (Overlap integral, eq. 2) of 0.73 (fig. 5 (a)), while it presents a conversion efficiency of more than 0.68 in the bandwidth of the pulse (from $700\,\mathrm{nm}$ to $930\,\mathrm{nm}$) (fig. 5 (b)).

3 Conclusions

In this work, vortex pulses propagation and generation was simulated solving a time-domain wave-equation. Chromatic dispersion induces temporal broadening of the vortex pulses while the spatial profile and spatio-spectral properties remained unchanged, thus conventional dispersion compensation techniques, can be used to compress back broadened vortices.

As well the effect of a SPP chromatic dispersion is negligible on the temporal profile of optical vortex pulses (very small broadening at the studied temporal and spectral range), while the spatial profile and spatio-spectral properties of the vortex remained unchanged. The analyzed SPP presents a conversion efficiency of more than 0.6 in a bandwidth from $630\,\mathrm{nm}$ to $1050\,\mathrm{nm}$. The results obtained in modeling vortex pulses can serve as a basis for novel devices design.

Acknowledgments. This work is supported by CONACyT via the PhD scholarship grant 763343 and by University of Guanajuato under research grant CIIC 272.2021.

References

1. Allen, L., Beijersbergen, M., Spreeuw, R. J. C.: Orbital angular momentum of light and the transformation of laguerre-gaussian laser modes. Physical Review A, vol. 45, no. 11, pp. 8185–8189 (1992) doi: 10.1103/physreva.45.8185
2. Beijersbergen, M. W., Coerwinkel, R. P. C., Kristensen, M., Woerdman, J. P.: Helical-wavefront laser beams produced with a spiral phaseplate. Optics Communications, vol. 112, no. 5-6, pp. 321–327 (1994) doi: 10.1016/0030-4018(94)90638-6
3. Bozinovic, N., Yue, Y., Ren, Y., Tur, M., Kristensen, P., Huang, H., Willner, A. E., Ramachandran, S.: Terabit-scale orbital angular momentum mode division multiplexing in fibers. Science, vol. 340, no. 6140, pp. 1545–1548 (2013) doi: 10.1126/science.1237861
4. Foo, G., Palacios, D. M., Swartzlander-Grover, A.: Optical vortex coronagraph. Optics Letters, vol. 30, no. 24, pp. 3308 (2005) doi: 10.1364/ol.30.003308
5. Malitson, I. H.: Interspecimen comparison of the refractive index of fused silica. Journal of the Optical Society of America, vol. 55, no. 10, pp. 1205 (1965) doi: 10.1364/josa.55.001205
6. Paterson, L., MacDonald, M. P., Arlt, J., Sibbett, W., Bryant, P. E., Dholakia, K.: Controlled rotation of optically trapped microscopic particles. Science, vol. 292, no. 5518, pp. 912–914 (2001) doi: 10.1126/science.1058591
7. Tamburini, F., Anzolin, G., Umbriaco, G., Bianchini, A., Barbieri, C.: Overcoming the rayleigh criterion limit with optical vortices. Physical Review Letters, vol. 97, no. 16 (2006) doi: 10.1103/physrevlett.97.163903
8. Toda, Y., Nagaoka, K., Shimatake, K., Morita, R.: Generation and spatiotemporal evolution of optical vortices in femtosecond laser pulses. Electrical Engineering in Japan, vol. 167, no. 4, pp. 39–46 (2009) doi: 10.1002/eej.20791
9. Wang, X. L., Luo, Y. H., Huang, H. L., Chen, M. C., Su, Z. E., Liu, C., Chen, C., Li, W., Fang, Y. Q., Jiang, X., Zhang, J., Li, L., Liu, N. L., Lu, C. Y., Pan, J. W.: 18-qubit entanglement with six photons' three degrees of freedom. Physical Review Letters, vol. 120, no. 26 (2018) doi: 10.1103/physrevlett.120.260502

ISSN 1870-4069

Temperature Sensor based on Vernier Effect Using Two Cascaded Capillary Hollow-Core Fiber Mach-Zehnder Interferometers

Sigifredo Marrujo-García[1], Iván Hernandez-Romano[2], Daniel A. May-Arrioja[3], Vladimir P. Minkovich[4], Miguel Torres-Cisneros[1]

[1] Universidad de Guanajuato, Electronics Department, DICIS, Mexico

[2] Universidad de Guanajuato, CONACYT-Electronics Department, DICIS, Mexico

[3] Centro de Investigaciones en Óptica, Aguascalientes, Mexico

[4] Centro de Investigaciones en Óptica, Guanajuato, Mexico

s.marrujogarcia@ugto.mx

Abstract. The purpose of this work is to report the fabrication of an exceptionally sensitive cascaded Vernier Effect-based temperature sensor using two Mach-Zehnder interferometers (MZIs). The MZIs sensors were fabricated by fusion splicing a small section of capillary hollow-core fiber (CHCF) between two, 1 mm length, segments of multimode fibers (MMFs). The laboratory results showed that the proffered sensor has a temperature sensitivity of 0.02804 nm/°C from 20 to 50 °C, while the in-line configuration shows an increment of around 67.35 times regarding the single sensor, being of 1.8885 nm/°C in a range from 20 to 60 °C. Furthermore, this sensor configuration shows a resolution of 0.0159 °C. Considering the materials used, temperature range, easy fabrication, low-weight, and low-power consumption we believe that our sensor based on the Vernier effect can be used in applications like cell culture, microfluidic microchannels, and edge computing.

Keywords: Optical fiber sensors, capillary hollow-core fiber, Mach–Zehnder interferometer, Vernier effect.

1 Introduction

The optical fiber sensors have been growing to become a meaningful and necessary technology for industry development and scientific advancement. These optical devices are appealing due to their immunity to electromagnetic interference, compact size, being lightweight and instant response. Also, fiber optic sensors can be used to test and measure a far-reaching number of physical variables among which is temperature.

All these fiber optic sensors (FOS) exploit two silica glass properties, the thermo-optic [1] and thermal expansion [2] effects to transform the changes of temperature into one of the following cases, the first case could be a wavelength shift or the second case could be power variations of the output spectrum.

One drawback of the all-fiber optic temperature sensors is their low sensitivities which make them ideal for high-temperature measurements but not adequate for low-temperature applications like in cell culture.

Different techniques have been used to overcome this disadvantage such as adding polymers [3] or nanoparticles to the fiber structures [4], they have shown good results, but the fabrication process becomes cumbersome. In the late years, the use of the Vernier effect has increased to enhance the temperature sensitivity of the fiber optic sensors, this is carried out by setting two fiber optic interferometers in parallel [5] or series [6] configuration.

In this work, we propose and demonstrate a temperature sensor built with two Mach-Zehnder interferometers (MZIs) in a series configuration (Vernier effect). The MZIs were made by fusion splicing a small piece of capillary hollow-core fiber between two pieces of multimode fiber.

2 Working Principle

2.1 Working Principle of a Single MZI

As shown below, the structure of the single MZI is made-up of a part of CHCF that is spliced between two small arts of MMFs. The dimensions of the transversal section of the CHCF are 65.5 μm for the inner diameter and 125 μm for the outer diameter. Using a broadband source of light, it is possible to inject light through the sensor and redirect it to the OSA to measure it, making use of the SMFs that are spliced to the sensor.

In previous works, a modal analysis of the MZI, to know the modes propagating in the fiber and it was found that two modes propagate in this structure [7]. The first one is the mode that travels in the hollow core made of air (the fundamental mode), and the second one is a ring cladding mode that propagates in the silica glass section. While the temperature changes, the RI of the silica glass also changes due to the TOC, giving place to temperature fluctuations and originating the wavelength shifts.

2.2 Working Principle of Two Cascaded MZIs

As aforementioned, the Vernier effect is observed when two signals are added together, to achieve this, it is necessary to set two MZIs in a series configuration, being the first sensor named as the reference and the second sensor as a sensing element. The sensing

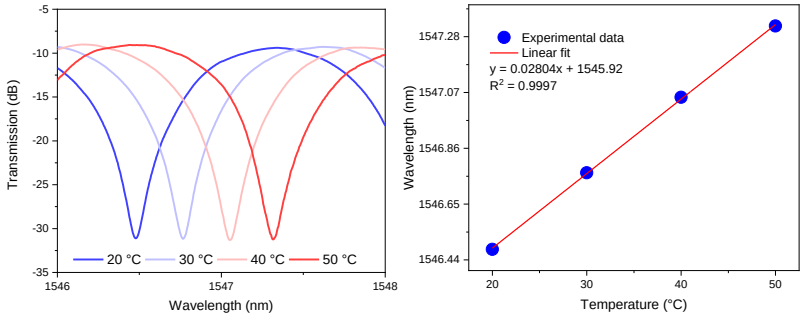

Fig. 1. Transmission spectra and wavelength shift of the MZI sensor at different temperatures.

MZI suffers the temperature variations, and the reference sensor is kept fixed at a sustained temperature. The sum (superposition) of the two signals creates an envelope. Then it is necessary to follow the wavelength shift of said envelope, allowing the measurement of temperature variations with higher sensitivities.

3 Fabrication and Experimental Results

3.1 Fabrication of a Single MZI

To begin with the fabrication of the sensors it is necessary to separate the manufacturing process into two parts. The first part of this process consists of splicing a 1 m long of SMF to a section of MMF and then cleaving the MMF to 1 mm in length.

This section is going to work as a beam splitter. After that, a section of CHCF was spliced to the MMF (beam splitter), and then the section of CHCF was cleaved to a length of 3 mm. This part of the sensor structure is set aside.

The second part requires fabricating another beam slitter (SMF + MMF), cleaving again the MMF to a 1 mm length. Finally, the part of the sensor that was set aside was spliced together with the newly fabricated beam splitter, completing the sensor.

3.2 Experimental Results of a Single MZI as a Temperature Sensor

To demonstrate that it is possible to use the Vernier Effect in a series configuration to enhance the temperature sensing capabilities of two MZI connected. It is necessary to characterize, at different temperatures, the sensitivity of the single MZI that will be used as a sensing element.

The setup consists of a light source, in our case a super luminescent diode (SLD) that injects light to the sensor using the 1 m long SMF attached to it and delivers the output transmission of the device to an OSA by the second SMF.

It is necessary to set the sensing MZI on a heating element, a Peltier cell in our case, to increment the temperature from 20 to 50 °C in little increments of 10 °C. The wavelength shift of the dip as the temperature increases shows a temperature sensitivity of 28.04 pm/ °C.

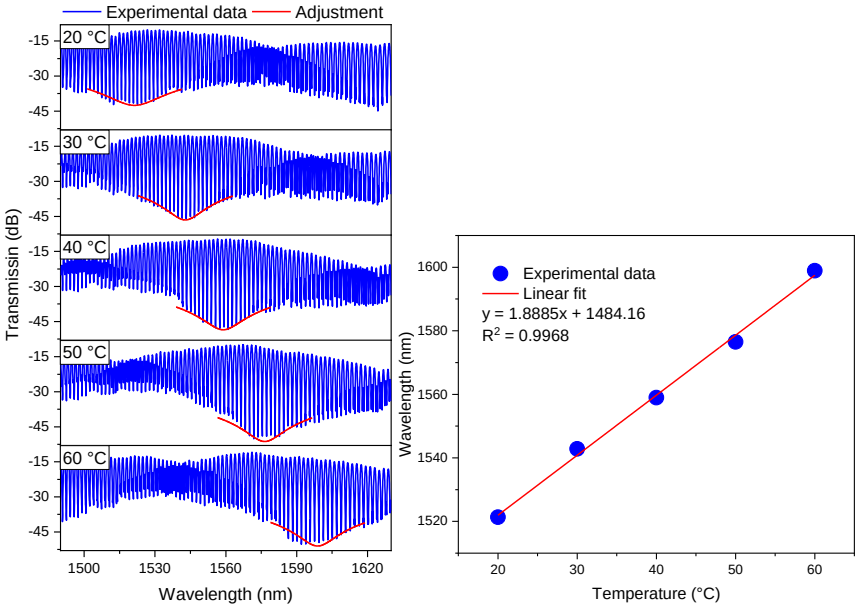

Fig. 2. Transmission spectra and wavelength shift of two cascaded MZI at different temperatures.

3.3 Experimental Results of Two Cascaded MZI Using the Vernier Effect

To test the temperature response of the two MZIs that were connected in series, it was necessary to reduce the temperature variations in the second MZI (the one used as reference). To achieve that a second heating element, with a fixed temperature, was necessary. It is worth noting that this new experimental setup works exactly like the previous one, but in this case, the sensing MZI was set on the Peltier cell, where temperature changes in steps of 10 °C, ranging from 20 to 60 °C, were made; meanwhile, the reference MZI was set on a hot plate at the fixed temperature of 30 °C.

The spectral response, as well as the wavelength shift, of the two cascaded MZIs using this configuration, is shown in Fig. 2. It is possible to observe that an interference pattern modulated with a low-frequency envelope is created. To measure the temperature sensitivity, we followed one dip of the lower envelope, obtaining its wavelength shift.

The temperature sensitivity of the two cascaded MZIs was 1.8885 nm/° C. By taking advantage of the Vernier effect, in the second experimental setup, we observed that the temperature sensitivity of the two cascaded MZIs is approximately 67.35 times higher than the sensitivity of the sensing MZI alone.

4 Conclusions

By way of conclusion, when exploiting the configuration of the cascaded Vernier effect, we demonstrated an exceptionally sensitive temperature sensor using two MZIs made entirely of silica glass. By employing this configuration, it was possible to achieve, in

a range from 20 to 60 °C, temperature sensitivity of 1.8885 nm/ °C, which is approximately 67.35 times higher than the sensitivity of the MZI alone. In addition, the MZIs sensors showed an excellent temperature resolution of 0.0159 °C.

Considering the materials used, temperature range, easy fabrication, low-weight, and low-power consumption we believe that our sensor based on the Vernier effect can be used in applications like cell culture, microfluidic microchannels, and edge computing.

References

1. Komma, J., Schwarz, C., Hofmann, G., Heinert, D., Nawrodt, R.: Thermo-optic coefficient of silicon at 1550 nm and cryogenic temperatures. Applied Physics Letters, vol. 101, no. 4, pp. 041905 (2012) doi: 10.1063/1.4738989
2. Li, X., Lin, S., Liang, J., Zhang, Y., Oigawa, H., Ueda, T.: Fiber-optic temperature sensor based on difference of thermal expansion coefficient between fused silica and metallic materials. IEEE Photonics Journal, vol. 4, no. 1, pp. 155–162 (2011) doi: 10.1109/JPHOT.2011.2181943
3. Hernández-Romano, I., Cruz-Garcia, M. A., Moreno-Hernández, C., Monzón-Hernández, D., López-Figueroa, E. O., Paredes-Gallardo, O. E., Villatoro, J.: Optical fiber temperature sensor based on a microcavity with polymer overlay. Optics express vol. 24, no. 5, pp. 5654–5661 (2016).
4. Urrutia, A., Goicoechea, J., Arregui, F. J.: Optical fiber sensors based on nanoparticle-embedded coatings. Journal of Sensors, vol. 2015 (2015) doi: 10.1155/2015/805053
5. Wang, Z., Huang, L., Liu, C., Wang, H., Sun, S., Yang, D.: Sensitivity-enhanced fiber temperature sensor based on Vernier effect and dual in-line Mach–Zehnder interferometers. IEEE Sensors Journal, vol. 19, no. 18, pp. 7983–7987 (2019) doi: 10.1109/JSEN.2019.2916891
6. Marrujo-García, S., Hernández-Romano, I., May-Arrioja, D. A., Minkovich, V. P., Torres-Cisneros, M.: In-line Mach–Zehnder interferometers based on a capillary hollow-core fiber using Vernier effect for a highly sensitive temperature sensor. Sensors, vol. 21, no. 16, pp. 5471 (2021) doi: 10.3390/s21165471
7. Marrujo-García, S., Hernández-Romano, I., Torres-Cisneros, M., May-Arrioja, D. A., Minkovich, V. P., Monzón-Hernández, D.: Temperature-independent curvature sensor based on in-fiber Mach–Zehnder interferometer using hollow-core fiber. Journal of Lightwave Technology, vol. 38, no. 15, pp. 4166–4173 (2020)

ISSN 1870-4069

Design of a Vibrations and Curvatures Sensor based on Optical Fibers by Using a FPGA

Jose Leopoldo Rubio-Galeana, Victor Manuel Carmona Reyes, Jesus Noe Rivera-Olvera, Rogelio Manuel Higuera-Gonzalez, Yanelis Lopez-Dieguez

Tecnológico Nacional de México/TES Ixtapaluca, División de Ingeniería Electrónica, Mexico

yanelis.ld@ixtapaluca.tecnm.mx

Abstract. In this work, we present the simulations results for a building monitoring system design. The goal is the flexibility to activate one or more alert modes (alarm sound, warning light, or both) to alert the population in the most effective way possible to a seismic movement. The mechanical effects we are testing are vibration, curvature, displacement, and strain. By the proposed sensing setup, using mono-mode optical fiber and an optical fiber sensor, can be analyzed remotely the data acquired and take decisions in an opportune way. The use of a Field Programmable Gate Array (FPGA) is proposed for data acquisition and processing. The simulations we realize, using six different data sets, are very promising, because of that, many other applications in corrosive or electromagnetics environments could be explored. In future investigations, industrial equipment, conveyor belt structures, or motors will be tested with this design, to detect breakage or malfunction promptly.

Keywords: FPGA; DOFS, optical fiber.

1 Introduction

Optical fiber has taken a leading role in recent decades, specifically, optical sensors are highly versatile [1]. This, coupled with the possibilities offered by distributed optical fiber sensors (DOFS Distributed Optical Fiber Sensor), has led to their being implemented for dissimilar applications; among which we highlight the evaluation of the health and integrity of the structures [2].

A DOFS has distinctive features compared to traditional electronic sensors, including the ability to provide long-distance monitoring of strain, vibration, and many other physical parameters with a single wire mode [3, 4].

For a long time, a human being has been looking for different ways to generate an alert before a seismic movement. This effort has resulted in many ways to do that from an empty bottle placed inverted on the floor, too expensive impact sensors placed in cars, showcases, and buildings, etc. However, how efficient are these systems? This

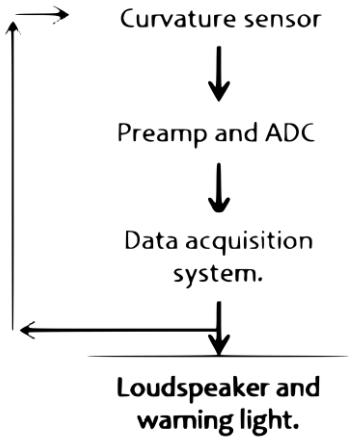

Fig. 1. Block Diagram for the seismic warning system.

question is one of the reasons that can cause more problems when choosing a seismic alarm.

In countries prone to seismic activity, there are certain construction standards that respond to studies of the demand and displacement capacity of structures [5]. However, due to the high construction costs, on some occasions, structures are designed with lower resistance than elastic since these demands are not considered in the correct way [5]. Consequently, the damages or collapses in buildings due to seismic activity are generally greater than those predicted by the engineers who worked on their design [5].

Although the economic losses that the collapse of a structure implies are, at times, invaluable, if we consider that they may be the cultural heritage of a certain region, the most important damages are the human losses that they could cause [6, 7]. Therefore, it is important to design policies that minimize these effects [6, 8, 9].

For these reasons, we present the design of a system that allows us to monitor the vibrations, curvatures, displacements, and strain of any structure. The proposed setup uses optical fiber as a transmission medium and a Field Programmable Gate Array (FPGA) as a data acquisition card [10].

With this system, it will be possible to remotely monitor buildings to alert people, using one or more alert modes (alarm sound, warning light, or both), in the most effective way possible to a seismic movement. Additionally, this system takes the advantage that the fiber optics system has magnific immunity to electromagnetic field [11–13].

2 Design

A seismic warning system is composed of a typical vibration signal processing and measurement system. It is made up of a vibration transducer, a pre-amplifier, a data acquisition card, and, in most cases, a loudspeaker. These transducers transform vibrations into electrical signals [14].

Table 1. Experimental data for curvature.

Curvature [m^{-1}]	Voltage [mV]	Analogic data	Binary data
50	4.66	3.817472	01000000110100000000000000000000
52	4.84	3.964928	01000000011111011011110000000000
54	5.02	4.112384	01000000100000111001100000000000
56	5.2	4.25984	01000000100010000000000000000000
58	5.38	4.407296	01000000100011010000000000000000
60	5.56	4.554752	01000000100100011100000000000000

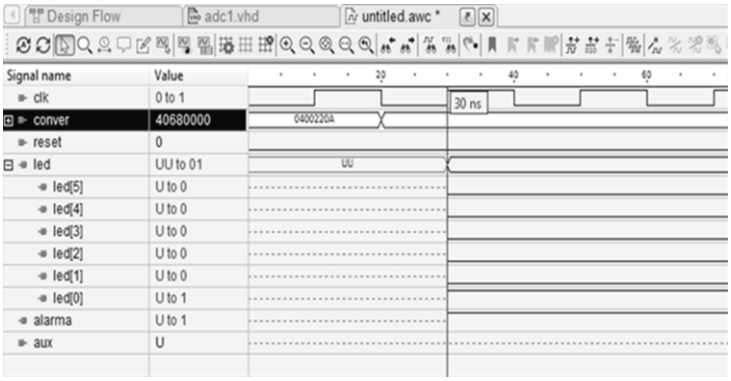

Fig. 2. Simulation's testing.

The main structure of a curvature sensor is formed by an optical fiber filament through which a beam of light is sent and depending on the change in refraction that occurs, a product of the curvature existing in the optical fiber, the curvature is quantified [15]. Curvature sensors allow us to obtain a highly sensitive and compact sensing system when determining small variations in displacement [16-21].

In our project, a curvature sensor will take the place of the vibration transducer, while as a data acquisition card we will use an FPGA from the Altera brand, from the Cyclone V family, model: 5CSEMA5F31C6N.

As a first step, the ADC converter equation was cleared. The original equation was obtained in the card's user manual:

$$ADC_{dato} = \frac{4096 * V_{muestra}}{5v}. \quad (1)$$

Once the equation was obtained, the conversion of the voltage obtained in the sensor to the analog data was carried out, to place it in the code. The analog data were converted to binary, however, when we realized that the analog data obtained was with decimals, we proceeded to use the IEEE 754 protocol, obtaining the following table of results (**¡Error! No se encuentra el origen de la referencia.**).

As the last step, the code was made using the "Modelsim-Altera" software. This allowed us to select from the beginning the FPGA with which we will work and, in this way, make the code with the respective pins.

3 Simulations Results

Considering the table of values shown in the development, we conclude that we have six different cases, which is why in our system we will have a series of LEDs that indicate each of the cases, in addition to activating a loudspeaker.

The simulation has the reading of the ADC pin, placing a variable that has a range of 4096 bits (which is the maximum value of bits of our ADC).

4 Conclusions

The results obtained during the simulations have been satisfactory, since we have used different tools to perform an adequate calculation, such as the IEEE 754 standard (used to make our programming code). This system is viable to monitor housing structures by recording the data of vibration, curvature, displacement, and strain to which they are subjected during an earthquake to be able to predict structural effects, even when they are not visible to the naked eye.

This system will allow to intervention in a timely manner in houses, rooms, walls, columns, or any other civil works whose structure has not been affected by the earthquake in its verticality or geometry, however, it has structural damage that could cause total or partial collapse of the work, thus avoiding the possible material losses or human lives that it could entail.

It should be noted that, although our system is oriented to structures such as buildings or homes, it can be adapted to any structure and/or industrial area, such as monitoring motors, conveyor belt structures, etc. By using fiber optics, it allows us to monitor large spatially distributed structures with a single cable (multi-mode or mono-mode fiber optic). It must also be taken into consideration, that the system has high durability and low-cost maintenance because of the use of fiber optics as a transmission medium.

Acknowledgments. Rubio-Galeana, Jose Leopoldo is grateful to Tecnológico Nacional de México and Gobierno del Estado de México for the supported under project "Monitoreo de vibraciones y curvaturas en estructuras" 2021.

References

1. Rajan, G.: Optical fiber sensors: Advanced techniques and applications. Press Taylor & Francis Group, p. 575 (2015) doi: 10.1201/b18074
2. Wijaya, H., Rajeev, P., Gad, E.: Distributed optical fibre sensor for infrastructure monitoring: Field applications. Optical Fiber Technology, vol. 64, p. 102577 (2021) doi: 10.1016/j.yofte.2021.102577
3. Sánchez, J. C., Alzate, L. H.: Diseño de alarma sísmica. Revista Mexicana de Física E, vol. 65, no. 1, pp. 15–21 (2019) doi: 10.31349/RevMexFisE.65.15
4. Perez-Conde, C.: Sensores ópticos. Universitat de València, vol. 30 (1996)
5. Rodríguez, M.: A Critical review of the seismic design practice of structures in Mexico. Ingeniería sísmica, vol. 94, pp. 27–48 (2016)
6. Caprano, S., Ortiz, S., Valencia, R.: Los efectos económicos de los sismos de septiembre. Revista Economía Informa, vol. 408, pp. 16–33 (2018)

7. Álvarez-Icaza, D., Medina-Mora, M. E.: Impacto de los sismos de septiembre de 2017 en la salud mental de la población y acciones recomendadas. Salud Pública de México, vol. 60, pp. 52–58 (2018)
8. Lino-Noboa, J. F., Moreira-Zambrano, M. J.: Prototipo de un módulo web para evaluar el daño post-sísmico en la estructura de edificios, mediante el uso de indicadores de gestión para la toma de decisions. Caso de estudio: Universidad de Guayaquil. Facultad de Ciencias Matemáticas y Físicas, Universidad de Guayaquil (2018)
9. Vallejo, M. L., Rodrigo, J. A.: FPGA: Nociones básicas e implementación. Departamento de Ingeniería Electrónica, Universidad Computense de Madrid (2004)
10. Rajan, G.: Optical fiber sensors: Advanced techniques and applications. Press Taylor & Francis Group, pp. 575 (2015) doi: 10.1201/b18074
11. Born, M., Wolf, E.: Principles of optics: electromagnetic theory of propagation, interference and diffraction of light. Elsevier (2013)
12. Santos, J. L., Farahi, F.: Handbook of optical sensors. Press Taylor & Francis Group, pp. 718 (2014) doi: 10.1201/b17641
13. Leal-Junior, A., Frizera, A., Lee, H., Mizuno, Y., Nakamura, K., Leitão, C., Domingues, M. F., Alberto, N., Antunes, P., André, P., Marques, M., Pontes, M. J.: Design and characterization of a curvature sensor using fused polymer optical fibers. Optics letters, vol. 43, no. 11, pp. 2539–2542 (2018)
14. Búa, M. S.: Sensores de curvatura: optimización de su rendimiento. Universidad Santiago de Compostela (2007)
15. Herrera-Piad, L. A., Haus, J. W., Jauregui-Vazquez, D., Lopez-Dieguez, Y., Estudillo-Ayala, J. M., Sierra-Hernandez, J. M., Rojas-Laguna, R.: A dual modality optical fiber sensor. Journal of Modern Optics, vol. 65, no. 3, pp. 342–347 (2018)
16. Jauregui-Vazquez, D., Rojas-Laguna, R., Estudillo-Ayala, J. M., Hernandez-Garcia, J. C., Lopez-Dieguez, Y., Sierra-Hernandez, J. M.: A multi-wavelength erbium-doped fiber ring laser using an intrinsic Fabry–Perot interferometer. Laser Physics, vol. 26, no. 10, p. 105105. (2016) doi: 10.1088/1054-660X/26/10/105105
17. Bai, Y., Yan, F., Liu, S., Wen, X.: All fiber Fabry–Pérot interferometer for high-sensitive micro-displacement sensing. Optical and Quantum Electronic, vol. 48, no. 206 (2016) doi: 10.1007/s11082-015-0323-y
18. Gutierrez-Rivera, M., Jauregui-Vazquez, D., Garcia-Mina, D. F., Sierra-Hernandez, J. M., Estudillo-Ayala, J. M., Almanee, M., Rojas-Laguna, R.: Fiber optic fabry-perot micro-displacement sensor based on low-cost polymer film. IEEE Sensors Journal, vol. 20, no. 9, pp. 4719–4725 (2019) doi: 10.1109/JSEN.2019.2944998
19. Kepak, S., Cubik, J., Zavodny, P., Siska, P., Davidson, A., Glesk, I., Vasinek, V.: Fibre optic track vibration monitoring system. Optical and Quantum Electronics, vol. 48, no. 354, pp. 1–10 (2016) doi: 10.1007/s11082-016-0616-9

ISSN 1870-4069

Sistema óptico HSI mediante la conjugación de la pupila con la superficie de un espejo refractor

Luis Arturo Tapia-Alarcón, Martin Alberto Vazquez-Castrejon, J. Jesús Escobedo-Altorre, Omar Palillero-Sandoval

Universidad Autónoma del Estado de Morelos,
Centro de Investigación en Ciencias básicas y Aplicadas (CIICAp),
México

omar.palillero@uaem.mx

Resumen. En un sistema óptico formador de imágenes con luz incoherente, el estudio de imágenes espectrales es de gran importancia debido al gran contenido de información que se puede obtener de algún objeto en cuestión. Con ayuda de un objeto colocado en la pupila de salida, y siguiendo la teoría de formación de imágenes se muestra el diseño un sistema formador de imágenes que permite observar el espectro óptico de un objeto de prueba, en este caso una abertura circular y un filamento de una lámpara incandescente, mediante la conjugación de la pupila sobre un espejo refractor que, con un sistema mecánico para realizar el escaneo, obtenemos un conjunto de imágenes hiperespectrales.

Keywords: Spectral imaging, image processing, optical systems.

HSI Optical System by Conjugating the Pupil with the Surface of a Refracting Mirror

Abstract. In an optical system that forms images with incoherent light, the study of spectral images is of great importance due to the great content of information that can be obtained from any object in question. With the help of an object placed in the exit pupil, and following the theory of image formation, the design of an image-forming system is shown that allows observing the optical spectrum of a test object, in this case an aperture. circular and a filament of an incandescent lamp, by conjugating the pupil on a refracting mirror that, with a mechanical system to perform the scanning, obtains a set of hyperspectral images.

Keywords: Spectral imaging, image processing, optical systems.

1. Introducción

El diseño de sistemas ópticos formadores de imágenes ha visto un desarrollo desde hace tiempo en las técnicas espectroscópicas, como medio de análisis e inspección no invasivo, debido a la posibilidad de obtener información sobre los componentes de una muestra basándose en la absorción de la luz [1-4]. Con el apoyo de las técnicas

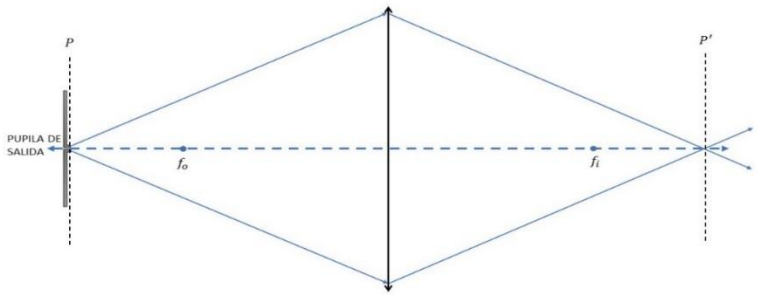

Fig. 1. El objeto en este caso, la pupila de salida, y los puntos de la imagen en P', corresponden entre sí y pueden intercambiarse.

espectroscópicas del visible/infrarrojo cercano y las técnicas de visión por computadora, ha surgido lo que se conoce como espectroscopia de imágenes [5-7]. Las imágenes hiperespectrales son un mapa de intensidad de luz que se puede extender en una o varias regiones del espectro electromagnético [8]. Las imágenes hiperespectrales son un conjunto de datos tridimensionales de un objeto o muestra, estos datos contienen información espacial y espectral.

Al conjunto de datos tridimensional comúnmente se le denomina "cubo hiperespectral". Los datos de un cubo hiperespectral pueden revelar información oculta, como por ejemplo la composición química o anatómica de un objeto [9]. Las imágenes hiperespectrales a menudo se utilizan para detectar elementos físicos y geométricos. Características tales como color, tamaño, forma y textura. También se puede utilizar para extraer información química y molecular intrínseca (como agua, grasas, proteínas y otros constituyentes) de un producto.

Los sistemas de imágenes hiperespectrales o también llamados HSI tienen la capacidad de obtener imágenes de más de 100 bandas espectrales. Los elementos principales de un sistema formador de imágenes espectrales son los siguientes [10]: Fuente puntual de luz, lentes y filtros, sensor de imagen, sistema de barrido, y hardware y software para procesamiento de imágenes.

2. Conjugación de pupila

Se entiende como conjugación de planos cuando el plano P, es el plano P', tal que los puntos P son imágenes de P'. En relación con la conjugación de pupila, tomamos la salida de la pupila como el plano P, y a la superficie del espejo refractor como el plano P', de manera que la pupila es imagen de la pupila que se forma sobre la superficie del espejo difractor.

Teniendo como base la teoría de formación de imágenes, y aplicando el tratamiento matemático para el caso con luz incoherente, se puede describir matemáticamente la obtención de las imágenes hiperespectrales mediante la conjugación de pupila y obedeciendo a la siguiente ecuación:

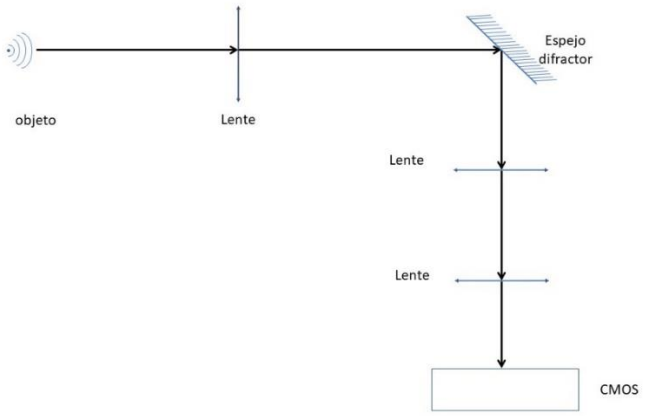

Fig. 2. Esquema del sistema formador de imágenes.

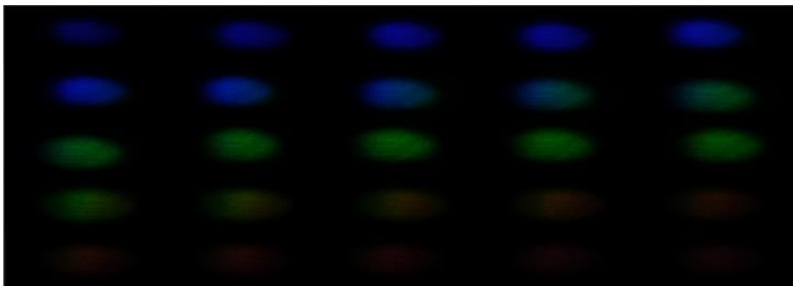

Fig. 3. Resultados de la segmentación de frecuencias de la luz emitida por LED.

$$g(x,y) = h(x,y) * O_i(x,y), \tag{1}$$

donde g(x,y) corresponde a la imagen, h(x, y) al sistema óptico y O(x, y) la intensidad del objeto.

3. Diseño de experimento y resultados

3.1. Diseño de experimento

Con ayuda de un objeto prueba, colocado en la pupila de salida del sistema óptico, se monta un sistema formador de imágenes que permite observar el espectro óptico del objeto. Para este trabajo, se utiliza un espejo que contiene una rejilla sobre su superficie lo cual da a lugar a una conjugación de planos para obtener la formación de imágenes, este método se conoce como conjugación de la pupila.

– El sistema se probó utilizando una apertura circular en el plano del objeto, para simular una fuente cuasi-puntual.

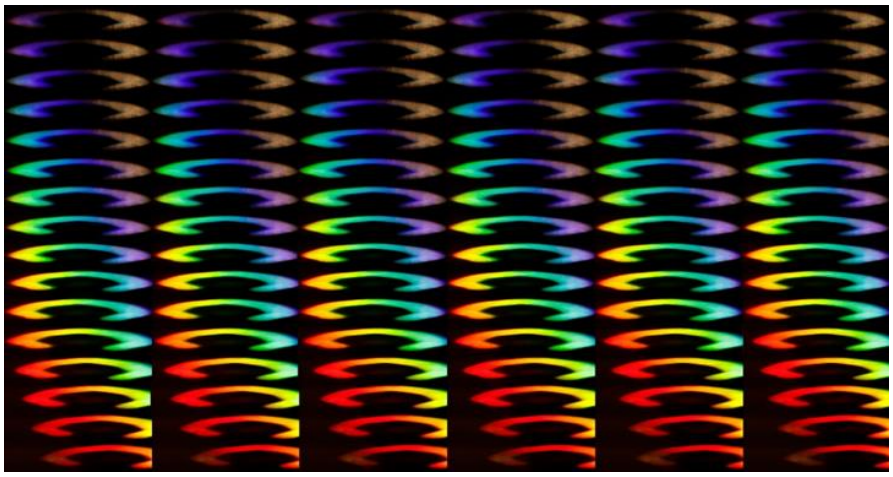

Fig. 4. Segmentación frecuencial del filamento incandescente.

- Posterior a la pupila se colocó una lente para colimar los rayos de luz provenientes de ella.
- En seguida con el haz de luz colimada de coloco un espejo difractor de forma cóncava.
- Finalmente, con el reflejo de la luz ya difractada se monta un sistema de lentes telescópico y se forma la imagen sobre el detector CMOS.

Un sistema mecánico realiza el escaneo en el plano imagen, la cantidad de imágenes obtenidas pertenecen a imágenes hiperespectrales.

3.2. Resultados

Las primeras pruebas se realizaron con un LED blanco, al cual se le coloco una pupila enfrente de manera que se pudiera simular una fuente cuasi-puntual, de esta prueba logramos obtener un set de imágenes donde se observa la transición de las frecuencias del espectro óptico en las que emite el LED, se puede apreciar claramente como en las zonas más frías del espectro emite con mayor intensidad, pero en la zona del espectro rojo, se aprecia en menor medida.

Se volvió a realizar el procedimiento, pero se sustituyo el LED por un foco incandescente, el cual nos permitió observar un mayor rango de frecuencias del espectro mucho mejor definidas y con más intensidad en su filamento, lo que nos permitió corroborar como el sistema es capaz de obtener una gran cantidad de imágenes a lo largo de todo el espectro óptico que emite un objeto.

4. Conclusiones

- Con un Sistema formador de imágenes se puede tener una gran cantidad de imágenes en el ancho del espectro de la luz visible, como se puede observar en

el filamento del foco incandescente, inclusive la configuración, no cambiaría mucho si se desea medir infrarrojo cercano y el UV.

– Esta técnica permite realizar análisis de imágenes espectrales que contienen una gran cantidad de información en áreas como los son el estudio de muestras biológicas o químicas, para así conocer su estado, defectos o incluso si están contaminadas con algún agente externo.

Referencias

1. ElMasry, G., Sun, D. W.: Principles of hyperspectral imaging technology. Hyperspectral imaging for food quality analysis and control, Academic Press, pp. 3–43 (2010) doi: 10.1016/B978-0-12-374753-2.10001-2
2. Du, C. J., Sun, D. W.: Learning techniques used in computer vision for food quality evaluation: a review. Journal of food engineering, vol. 72, no. 1, pp. 39–55 (2006) doi: 10.1016/j.jfoodeng.2004.11.017
3. Goodman, J. W.: Introduction to Fourier optics. Roberts and Company publishers (2005)
4. Fowles, G. R., Lynch, D. W.: Introduction to modern optics, Courier Corporation. vol. 36, no. 8 (1968)
5. Zavala-De Paz, J., Isaza, C., Mosquera-Mosquera, J., Anaya-Rivera, E., Rizzo-Sierra, J., Palillero-Sandoval, O., Escobedo, J.: Non-invasive methodology for the study of wound healing process using spectral images. IEEE Latin America Transactions, vol. 18, no. 4, pp. 687–695 (2020) doi: 10.1109/TLA.2020.9082211
6. Isaza, C., Mosquera, J. M., Gómez-Méndez, G. A., Paz, Z. D., Jonny, P., Karina-Anaya, E., Palillero-Sandoval, O.: Development of an acousto-optic system for hyperspectral image segmentation. Metrology and Measurement Systems, vol. 26, no. 3 (2019) doi: 10.24425/mms.2019.129576
7. Du, C. J., Sun, D. W.: Learning techniques used in computer vision for food quality evaluation: a review. Journal of food engineering, vol. 72, no. 1, pp. 39–55 (2006) doi: 10.1016/j.jfoodeng.2004.11.017
8. Inoue, T., Hirai, A., Itoh, K., Ichioka, Y.: Compact spectral imaging system using liquid crystal for fast measurement. Optical Review, vol. 1, no. 1, pp. 129–131 (1994) doi: 10.1007/s10043-994-0129-9
9. Levenson, R. M.: Spectral imaging perspective on cytomics. Cytometry Part A: the journal of the International Society for Analytical Cytology, vol. 69, no. 7, pp. 592–600 (2006) doi: 10.1002/cyto.a.20292
10. Qiao, J., Ngadi, M. O., Wang, N., Gariépy, C., Prasher, S. O.: Pork quality and marbling level assessment using a hyperspectral imaging system. Journal of Food Engineering, vol. 83, no. 1, pp. 10–16 (2007) doi: 10.1016/j.jfoodeng.2007.02.038

ISSN 1870-4069

Interfaz gráfica para monitoreo de vibración en puentes de concreto

José María Sánchez-Manzo[1], Víctor Iván Ruíz-Perez[2], Héctor Crespo-Guerra[1], Jorge Luis Camas-Anzueto[1], Joel Gómez-Pérez[1]

[1] Tecnológico Nacional de México, Instituto Tecnólogico de Tuxtla Gutierréz, México

[2] Universidad Autónoma de Chiapas, Facultad de Ciencias en Física y Matemáticas, México

{js925222, 9612715227}@gmail.com

Resumen. Las vibraciones en puentes ocurren en dirección vertical, horizontal y en algunos casos torsional, provocando deficiencia en la rigidez pueden llegar a generar desde grietas hasta que el puente colapse, una prueba de ello es el terremoto que se vivió el 7 de septiembre de 2017 en México. Por lo que es necesario contar con sensores que ayuden a monitorear el estado en que se encuentran los puentes para asegurar la funcionalidad de este [3]. El Monitoreo de Salud Estructural -SHM- se describe como el registro permanente, continuo o periódico de parámetros que reflejan la condición y el rendimiento de una estructura [5]. Con los datos recopilados se puede identificar daños, planear obras de mantenimiento, aumentar su confiabilidad, y ampliar el conocimiento de la estructura dada. Para ello se requiere contar con sistemas de medición precisos y rentables. Este artículo presenta el diseño de una interfaz gráfica aplicada al -SHM-, específicamente a la detección de vibración en puentes de concreto. Para adquirir los datos de un sensor de vibración de fibra óptica se requiere conectar a la salida un foto-detector y convertir la potencia óptica a voltaje. Este es acondicionado a una tarjeta de adquisición de datos, para poder comunicarse con la interfaz desarrollada en el entorno de Labview. Con la finalidad de observar la frecuencia de la vibración que como se menciona es un parámetro importante para el monitoreo de puentes de concreto. Finalmente se puede capturar los datos obtenidos, para análisis posteriores, diversas pruebas, o reportes de investigación en los que se requiera de ellos. Toda esta información puede ayudar a desarrollar propuestas de prevención de desastres, y así prevenir y alertar a la población en general [4].

Palabras clave: Interfaz gráfica, fotodetector óptico, transmisor óptico, vibración.

Graphical Interface for Monitoring Vibration in Concrete Bridges

Abstract. Vibrations in bridges occur in vertical, horizontal, and in some cases, torsional directions. These vibrations, if they indicate a deficiency in rigidity,

can result in issues ranging from cracks to the complete collapse of the bridge. A prime example of this was the earthquake on September 7, 2017, in Mexico. Hence, it is essential to have sensors that help monitor the condition of bridges to ensure their functionality. Structural Health Monitoring (SHM) is defined as the constant, continuous, or periodic recording of parameters reflecting the condition and performance of a structure. Using the gathered data, it's possible to identify damages, plan maintenance, increase reliability, and enhance the understanding of a given structure. This necessitates precise and cost-effective measurement systems. This article presents the design of a graphical interface applied to SHM, specifically targeting vibration detection in concrete bridges. To acquire data from an optical fiber vibration sensor, it needs to be connected to a photodetector output and convert the optical power to voltage. This is conditioned to a data acquisition card to communicate with the interface developed in the Labview environment. The aim is to observe the vibration frequency, which, as mentioned, is a crucial parameter for monitoring concrete bridges. Finally, the captured data can be used for subsequent analysis, various tests, or research reports that require them. All this information can contribute to the development of disaster prevention proposals, thus helping to warn and safeguard the general population.

Keywords: Graphical interface, optical photodetector, optical transmitter, vibration.

1. Introducción

Un puente es fundamental para el desarrollo socioeconómico del país, como el nuestro ya que debido a su geografía enlaza a diferentes lugares gracias a su red de carreteras y puentes, por ello es de vital importancia garantizar la seguridad de los usuarios porque de no ser así el deterioro o daño de estos llega a desencadenar grandes perdidas. En los últimos años se han desarrollado distintos estudios y equipos de monitoreo para detectar anomalías o fallas estructurales. Uno de los métodos mas conocidos es el –SHM–.

Es un método no destructivo que ayuda a la identificación y detección de posibles daños en estructuras civiles, como deformaciones, fatiga, etc. por lo general esta técnica se implementa a distancia en tiempo real, usando sensores in situ, reduciendo costos de inspección y tiempo de respuesta. En años recientes debido a los constantes avances de los sensores de fibra óptica y sus mejoras contra sensores convencionales como un mejor tiempo de respuesta, durabilidad, mayor soporte a territorios hostiles [6] hacen que su uso para este tipo de monitoreo sean los ideales y tengan un mejor desempeño.

1.1. Las vibraciones

Es el fenómeno mecánico descrito por un movimiento oscilatorio de un sistema estructura lo mecánico respecto a su punto de equilibrio, está definida en términos de frecuencia, y amplitud. La vibración de una estructura implica la existencia de energía potencial que afecta su frecuencia natura. En estructuras civiles la vibración se considera un efecto indeseable, debido a que produce desgastes,fatigas o fracturas de partes o elementos, y sensación de incomodidad para los usuarios.

Tabla 1. Captura de mediciones.

Fecha	Amplitud (V)	Frecuencia (Hz)
11/7/2021 10:30:54	0.081024	3.857023
11/7/2021 10:30:54	0.040732	3.885094
11/7/2021 11:02:21	0.228978	4.113476
11/7/2021 11:02:21	6.653000	4.040936
11/7/2021 11:02:22	0.092951	3.974555

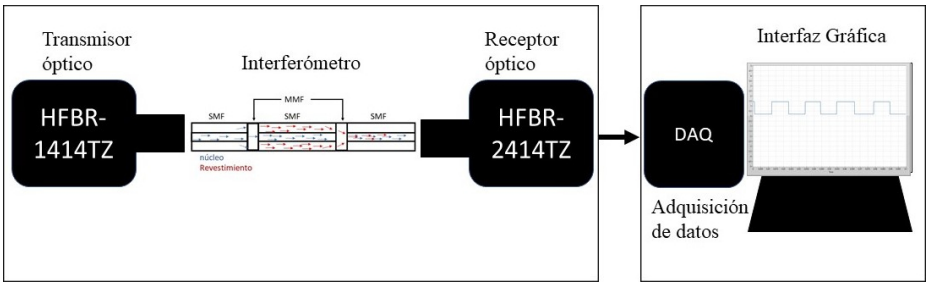

Fig. 1. Sistema de análisis de vibración.

Vibraciones estructurales. "Una estructura es una combinación de partes unidas entre ellas para crear un marco de soporte, que pueden ser parte de un edificio, barco, máquina, vehículo espacial, motor o cualquier otro sistema" [2]. Se definen 4 tipos de fuentes de vibración, libre, forzada, aleatoria y desvalance rotatorio. Para el análisis de este tipo de vibraciones esesencial el modelado matemático, que se define de la siguiente manera. La ecuación general de las vibraciones es:

$$m\frac{\partial^2 y}{\partial^2 t} + b\frac{\partial y}{\partial t} + ky = p(t), \tag{1}$$

donde -y- es la magnitud que sufre vibraciones periódicas temporales, -$P(t)$- la variable de reforzamiento o fenómeno incidente de la vibración; a, b, y k son las constantes características del sistema. Utilizando la transformada de Laplace, tenemos que:

$$(as^2 + bs + k)y(s) = p(s), \tag{2}$$

$$\frac{y(s)}{P(s)} = G(s) = \frac{1}{s^2 + \frac{b}{a}s + \frac{k}{a}}. \tag{3}$$

La ecuación 3 define la función de transferencia general de un sistema de vibración, lo que facilita el modelado y diseño de simulaciones [1].

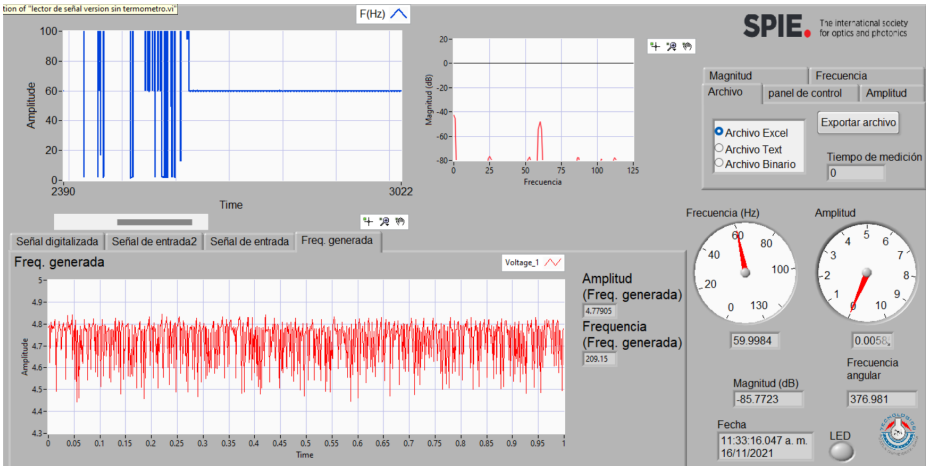

Fig. 2. Interfaz gráfica.

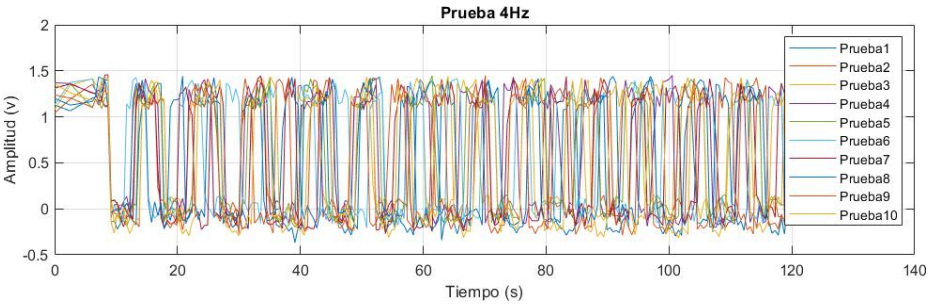

Fig. 3. Prueba a 4 Hz.

2. Desarrollo del sistema

La necesidad de garantizar la seguridad de los usuarios de los puentes es de gran importancia desde temas de investigación, monitoreo y control estructural. Las vibraciones en puentes pueden ocurrir en dirección vertical, horizontal y en algunos casos torsional, provocando deficiencias en la rigidez que pueden llegar a generar desde grietas hasta el colapso del puente [5].

Para este trabaja utilizamos un sensor de fibra óptica para detectar vibración basado en interferometría específicamente un Interferómetro Mach Zehnder -MZI-. El diagrama a bloques del sistema utilizado en este trabajo se de investigación se muestra en la Fig. 1. El sistema fue diseñado para monitorear las vibraciones y esta constituido principalmente por el Hardware de adquisición -Transmisor óptico, Interferómetro, Receptor óptico- y el software de procesamiento de la señal -Interfaz gráfica desarrollada en **Labview**-.

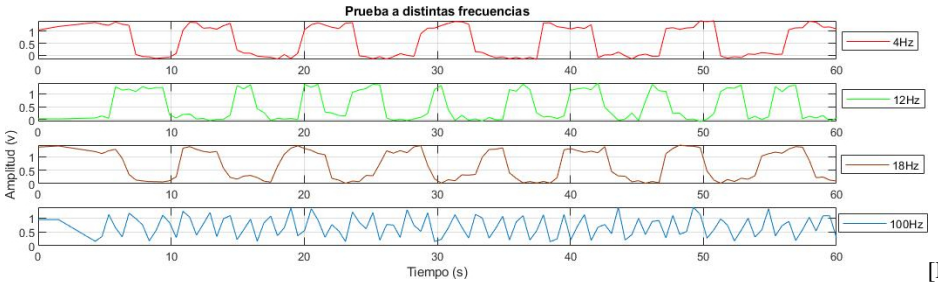

[H]

Fig. 4. Prueba a distintas frecuencias.

2.1. Sistema de adquisición

El sistema esta conformado por cuatro etapas -ver Fig. 1-, donde la primera es una etapa de transmisión -utilizando el transmisor óptico `HFBR-1414TZ`, y el generador de señales `FG-100`, emitiendo luz y viajando atravez de la -FO- hasta llegar a la segunda etapa donde se encuentra el MZI, la tercera etapa contiene un receptor óptico -`HFBR-2414TZ`- donde recibe la luz proveniente del -MZI- y se convierte en voltaje análogo. Finalmente la Ultima etapa consiste en recibir el voltaje del receptor en una `DAQ-Ni usb 6002`, y esta es procesada y visualizada en la Interfaz desarrollada.

3. Diseño de la interfaz gráfica

3.1. Interfaz gráfica

La interfaz diseñada en el entorno de Labview se observa en la Fig. 2. Esta se encarga de muestrear la señal adquirida en diferentes gráficas, la visualización de datos como la amplitud y frecuencia de la señal en todo momento, configurar los periodos de muestreo y un menú que te da la opción de almacenar los datos en archivos -.xlsx, .text- para todo tipo de análisis, de igual manera se pueden exportar las gráficas.

4. Resultados y conclusión

4.1. Resultados

En la tabla 1 se muestran algunos datos obtenidos de las mediciones realizadas datos que nos sirven para llevar un registro de las pruebas realizadas para su análisis. En la Fig. 3 se muestra una prueba a $4\,\mathrm{Hz}$ repetida diez veces en un lapso de $120\,\mathrm{s}$, con el fin de observar el comportamiento de todo el sistema y vemos que durante las pruebas el voltaje detectado era de $1.5\,\mathrm{V}$ manteniéndose constante durante todas las mediciones. En la Fig. 4 se muestra el comportamiento del sensor a distintas frecuencias.

4.2. Conclusión

Con los resultados obtenidos se asegura que la interfaz mediante el uso de un MZI, es una buena alternativa para la obtención de frecuencias de vibración ya que para el tipo de aplicaciones que esta pensado se requiere de sistemas que detecten bajas frecuencias desde $-2\,\mathrm{Hz}$ hasta $20\,\mathrm{Hz}$ como se reporta en la literatura que aborda el análisis de vibraciones en puentes donde en esos rangos se encuentran las frecuencias naturales de puentes estudiados [8, 7, 9].

Referencias

1. Barajas, P. O. M.: Vibraciones Mecánicas – Modelamiento Matemático (2022)
2. Beards, C. F.: Structural vibration: Analysis and damping. Elsevier Science (1996)
3. Garita, C.: Enfoques de integración de información para sistemas de monitoreo de salud estructural de puentes. Revista Tecnología en Marcha, vol. 29, no. 1, pp. 96 (2016) doi: 10.18845/tm.v29i1.2542
4. Isaza-Monsalve, C. M., Muñoz-Saldarriaga, J. E., Agudelo-Mesa, L. M.: Sistema inalámbrico detector de vibraciones sísmicas, con interfaz gráfica en el entorno industrial labview. Informe Final de Trabajo de Grado, Instituto Tecnológico Metropolitano (2018)
5. Moughty, J. J., Casas, J. R.: A state of the art review of modal-based damage detection in bridges: development, challenges, and solutions. Applied Sciences, vol. 7, no. 5, pp. 510 (2017) doi: 10.3390/app7050510
6. Navarro-Henríquez, F.: Sensores de fibra óptica FBG para el monitoreo de la salud estructural de los puentes. Revista Tecnología en Marcha, vol. 27, no. 4, pp. 3 (2014) doi: 10.18845/tm.v27i4.2080
7. Navarro-Henríquez, F., Ureña-Muñoz, D.: Mediciones y análisis de vibraciones en el puente Virilla, Ruta Nacional no 1. Tecnología en Marcha, vol. 28, no. 2, pp. 16 (2015)
8. Rodriguez, S., Gallardo, J., Araúz, O.: Estudio del período de vibración de puentes de concreto en Panamá. Revista I+D Tecnológico, vol. 13, no. 1, pp. 83-90 (2017)
9. Secretaria de Comunicaciones y Transportes: Evaluación de puentes mediante el análisis de vibraciones. Publicación Técnica, no. 132 (1999)

ISSN 1870-4069

Higher Order Numerical Derivatives for Data Processing in Optics and Photonics

Luis David Lopez-Zavala, Oleksiy V. Shulika

Universidad de Guanajuato,
Departamento de Ingeniería Eléctrica,
Mexico

luiszavala@live.com.mx, osulika@ugto.mx

Abstract. Data processing is fundamental for the correct interpretation and analysis of experimental results, so it is common to compute derivatives of noisy sets of data. The same situation is observed when data to be processed are obtained from numerical simulations. Here we present three different methods for numerical calculation of higher-order derivatives, up to 20th order. The complex integration and automatic differentiation show the best results.

Keywords: Higher-order derivatives, numerical approximation, holomorphic function, data processing, automatic differentiation, integration in complex plane.

1 Introduction

When working on any experimental development, the results often includes a mixture of noise and measurement-related phenomena, so it is not easy to draw conclusions from a set of raw data, and this is where data processing plays an important role. Differentiation is the process of determining how quickly a function varies, as the quantity on which it depends change. Geometrically, it can be seen as the slope of a tangent line at a given point within the domain of the function, so the derivative of a functions is capable of giving information about the behavior of functions [4].

The derivative of the result of another derivative is called the second derivative of the original function, and geometrically represents the rate of change of the slope of the original function's tangent line. Higher-order derivatives are useful, especially, when dealing with functions such as those from real experimental data. Here we present three different derivative methods are studied and compared in terms of accuracy and derivative order to choose the best for row data processing applications.

2 Richardson's Extrapolation

Richardson's extrapolation makes a faster convergent sequence from another already convergent sequence in order to get a recursive method that is reliable in convergence speed and accuracy. To do so, two different derivative approximations, $D(h)$ and $D(h_1)$ for two different parameters h and h_1, supposing that $h_1 > h$, are considered.

Generally, an approximation of a derivative, which depends on the length of step h and its truncation error, can be expressed in the series form such as the finite differences method, which arises from the following series expansion:

$$f'(x_0) = D(h) + a_1 h^{n_1} + a_2 h^{n_2} + a_3 h^{n_3} + \cdots n_1 < n_2 < n_3. \tag{1}$$

Expanding the derivative approximation for h_1, and using the ratio between the step sizes $r = h_1/h \Longrightarrow h_1 = rh$ an equation in terms of h can be written as:

$$f'(x_0) = D(rh) + a_1 (rh)^{n_1} + a_2 (rh)^{n_2} + a_3 (rh)^{n_3} + \cdots \tag{2}$$

Then, to eliminate a truncation error term, Eq. (1) is multiplied by r^{n_1}, and Eq. (2) is subtracted from it, to get:

$$f'(x_0) = \frac{r^{n_1} D(h) - D(rh)}{r^{n_1} - 1} + a_2 h^{n_2} \frac{r^{n_1} - r^{n_2}}{r^{n_1} - 1} + a_3 h^{n_3} \frac{r^{n_1} - r^{n_3}}{r^{n_1} - 1} + \cdots \tag{3}$$

The Eq. (3) represents the extrapolation process and substituting:

$$D_1(h) = \frac{r^{n_1} D(h) - D(rh)}{r^{n_1} - 1}, \quad b_2 = a_2 \frac{r^{n_1} - r^{n_2}}{r^{n_1} - 1}, \quad b_3 = a_3 \frac{r^{n_1} - r^{n_3}}{r^{n_1} - 1}, \cdots \tag{4}$$

In the result a new approximation arises, in which an error term has been eliminated, and becomes a formula with error $O(h^{n_2})$. Finally, substituting r into Eq. (3) gives:

$$f'(x_0) = \frac{\left(\frac{h_1}{h}\right)^{n_1} D(h) - D(h_1)}{\left(\frac{h_1}{h}\right)^{n_1} - 1} + b_2 h^{n_2} + b_3 h^{n_3} + \cdots \tag{5}$$

2.1 Recursion

From a set of approximations F, obtained by different values of h, it is possible to apply the Richardson's formula in a recursive way using the following expression:

$$F_m^n = \frac{\left(\frac{h_n}{h_{n+m}}\right)^{\beta} F_{m-1}^{n+1} - F_{m-1}^n}{\left(\frac{h_n}{h_{n+m}}\right)^{\beta} - 1}. \tag{6}$$

The Eq. (6) can only be used when the truncation error of F has the form:

$$\sum_{k=1}^{\infty} a_k h^{\beta k}. \tag{7}$$

So a special case of Richardson's recursive formula can be obtained by using the centered finite difference formula as the base convergent sequence, whose truncation error can be expressed as:

$$2 \sum_{k=1}^{\infty} \frac{h^{2k}}{(2k+1)!} \; f^{2k+1}(x_i). \tag{8}$$

And therefore the condition for the recursive formula is satisfied with $\beta = 2$. Finally considering that $h_n = 2h_{n-1}$ the Expr. (6) becomes:

$$F_m^n = \frac{4^m F_{m-1}^{n+1} - F_{m-1}^n}{4^m - 1}. \tag{9}$$

This particular case is the most widely used form of Richardson's extrapolation due to the oversimplifying of the calculations [1].

3 Complex Integration Method

The concept of holomorphic function in complex number's theory states that if a complex valued function is complex differentiable in a neighborhood of each point in a domain, then it is infinitely differentiable and locally equal to its Taylor series [5].

Consider a function $f(z)$ holomorphic in the simple closed contour C and at all points inside it, then a circle C_0 with center in z_0 and radius r small enough that all points of C_0 are inside C, so the function is holomorphic in C, C_0 and at all the points of the doubly connected domain. Then considering the function $f(z)/(z - z_0)$, which is holomorphic at every point except $z = z_0$, the contour C can be related to C_0 trough the contour deformation principle, since the singularity violates the Cauchy-Goursat theorem the relation is not nullified, and is written as:

$$\oint_C \frac{f(z)}{z - z_0}\, dz = \oint_{C_0} \frac{f(z)}{z - z_0}\, dz. \tag{10}$$

This allows to evaluate the integral, using polar coordinates since the contour C_0 is a circle, to solve for $f(z_0)$. To do so, C_0 is parametrically expressed through the polar angle θ and with the following change of variable $z = re^{i\theta} + z_0$ and $\frac{dz}{d\theta} = ire^{i\theta}$, the Eq. (10) is rewritten as:

$$\oint_{|z-z_0|=r} \frac{f(z)}{z - z_0}\, dz = \int_0^{2\pi} f(z(\theta)) \frac{dz}{d\theta} d\theta = i \int_0^{2\pi} f(z_0 + re^{i\theta})\, d\theta. \tag{11}$$

To know the value $f(z)$ in $z = z_0$, the limit when r tends to 0 is applied in the right side of Eq. (11):

$$\oint_C \frac{f(z)}{z - z_0}\, dz = \lim_{r\to 0} i \int_0^{2\pi} f(z_0 + re^{i\theta})\, d\theta = i \int_0^{2\pi} f(z_0)\, d\theta = i\theta f(z_0)|_0^{2\pi} = 2\pi i f(z_0). \tag{12}$$

And solving the Eq. (12) for $f(z_0)$, the Cauchy integral formula is obtained:

$$f(z_0) = \frac{1}{2\pi i} \oint_C \frac{f(z)}{z - z_0}\, dz. \tag{13}$$

Given the holomorphic criteria, $f(z)$ has derivatives of all the orders in the domain in which it is analytic and its derivatives are also analytic in the domain, hence Eq. (13) can be generalized as:

$$f^{(n)}(z_0) = \frac{n!}{2\pi i} \oint_C \frac{f(z)}{(z - z_0)^{n+1}}\, dz. \tag{14}$$

3.1 Parameterized Cauchy Integral Formula

Since the Cauchy's formula is written for complex functions, the contour C must be parameterized as a function of time $C(t) = a + e^{it}$, for $0 \leqslant t \leqslant 2\pi$ where a is the center of the unitary circle, in order to apply Cauchy's formula for real functions. The parameterized Cauchy's integral formula states that if a function $f(t)$ is analytic within the simple connected domain D and C is any simple closed contour wholly located at D, then for any point a within C:

$$f^{(n)}(a) = \frac{n!}{2\pi} \int_0^{2\pi} f(a + e^{it}) e^{-int}\, dt. \tag{15}$$

4 Automatic Differentiation Method

The automatic differentiation method is based in decompose a function in a set elemental operations sequence easily differentiable each and computing the derivative by attach each elemental derivative using the chain rule, taking the problem by a combination of numerical and symbolical techniques which take advantage of the benefits of both. Since elemental function's derivatives are already known the results reach symbolical accuracy [3].

A good graphical representation of the evaluation path of the method is a graph, which is an important tool based in dynamic coding and very useful to identify the dependency relations between variables, that stores the result of each elementary operation in intermediate variables v_j. The derivative of single dependent variable function with respect to a independent variable can be calculated applying systematically the chain rule from the input vertices to the output vertice of the graph, this evaluation path is called Forward mode since the evaluations are propagated forward from input to output.

Considering that the derivative of a vertice with respect to the independent variable is the sum of the values of the incoming edges, and each contribute with the total derivative of the vertice at the begin of the edge times the partial derivative of the vertice that the edge points with respect to the vertice at the begin of the edge [2]. This evaluation can be generalized as a column of a Jacobian matrix of a function $f : \Re^n \rightarrow \Re^m$, if the respective input variable is initialized in 1 and the rest in 0. In this way the entire matrix will be formed after the n-times applications of the forward mode. It is easy to think that if each elemental operations knows its derivative, the recursive application of the method should result in the higher order derivatives of the original function.

5 Results

To compare which method is the best for data processing, the accuracy and maximum order of the higher-order derivatives of a noisy exponential function, computed by each method, are studied. An exponential function is chosen due that all its derivatives are equal to the exponential function, also if results are plotted on a semi-logarithmic scale the derivatives looks like a straight line.

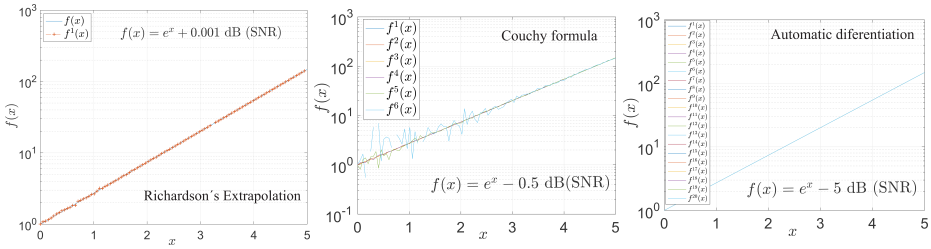

Fig. 1. Higher-order numerical derivatives computed by each of the three methods.

Then, for each method a noisy exponential function, generated by adding a sample noisy vector to the evaluated function vector, is considered. The sample noisy vector is generated by the Matalab's random number generation function which return a standard normally distributed matrix numeric array of any size.

6 Conclusions

Richardson's extrapolation method can compute accurately at least the first four derivative orders of a fundamental function, although its noise tolerance is very low since noise that generates a signal to noise ratio of 0.01 dB is enough to get divergent results for the first derivative. On the other hand, the complex integration method is capable of calculating the first sixteen derivative orders of a fundamental function and the fourth derivative of a noisy signal, filtering a signal with an SNR of up to -0.05 dB.

Finally, the automatic differentiation method is the most accurate way to compute higher order derivatives of fundamental functions, no matter the order, avoiding truncating and round error by its symbolic properties, however, the higher the derivative order, the higher the processing time, so it is not recommended for real time applications. Its noise tolerance is enough to compute accurate derivatives of signals with an SNR up to -7 dB.

Acknowledgments. This work is supported by University of Guanajuato under research grant CIIC 272.2021.

References

1. Burden, R. L., Faires, J. D.: Análisis numérico. Thomson Learning (2002)
2. Callejo-Goena, A., García-de-Jalón-de-la-Fuente, F. J., Hidalgo, A.: Diferenciación automática de fuerzas en la integración implícita de sistemas multicuerpo. In: XVIII Congreso Nacional de Ingeniería Mecánica, pp. 3–5 (2010)
3. Günes-Baydin, A., Pearlmutter, B. A., Andreyevich-Radul, A., Mark-Siskind, J.: Automatic differentiation in machine learning: A survey. The Journal of Machine Learning Research, vol. 18, no. 1, pp. 1–43 (2018)
4. Riley, K. F., Hobson, M. P., Bence, S. J.: Mathematical methods for physics and engineering. American Association of Physics Teachers (1999) doi: 10.1017/cbo9781139164979
5. Wunsch, A. D.: Variable compleja con aplicaciones. Addison-Wesley Longman (1999)

ISSN 1870-4069

Uso del aprendizaje profundo para la discriminación automática de imágenes que contienen autopartes defectuosas

Rafael Guzmán-Cabrera[1], Daniel Alberto May-Arrioja[2], Mary Carmen Peña-Gomar[3], Miguel Torres-Cisneros[1]

[1] Universidad de Guanajuato, Grupo de Física Aplicada y Tecnologías Avanzadas, División de Ingenierías, México

[2] Centro de Investigaciones en Óptica A.C., Laboratorio de Fibras Ópticas y Óptica Integrada, México

[3] Universidad Michoacana de San Nicolás de Hidalgo, FCFM, México

torres.cisneros@ugto.mx

Resumen. Se muestra la clasificación automática de imágenes de autopartes con defectos de soldadura, usando lenguaje de máquina que involucra la RESNET50 en el escenario de clasificación; conjuntos de entrenamiento-prueba se usaron 4 diferentes clasificadores con 2 métricas de evaluación. Se obtuvo 100 % de precisión en los resultados.

Palabras clave: manufactura, clasificación automática, lenguaje de máquina, redes neuronales.

Using Deep Learning for Automatic Discrimination of Images Containing Defective Auto Parts

Abstract. The automatic classification of images of auto parts with welding defects is shown, using machine language that involves the RESNET50 in the classification scenario; training-test sets, 4 different classifiers with 2 evaluation metrics were used. 100% accuracy was obtained in the results.

Keywords: Manufacturing, automatic classification, machine language, neural networks.

1. Introducción

En las últimas décadas, el uso de los sistemas de cómputo en diversas tareas humanas es cada vez más frecuente. Uno de los principales objetivos de su uso es el de respaldar

las tareas humanas. Por ejemplo, en esta tarea de asistencia se ha incorporado el uso de herramientas de inteligencia artificial, tales como el aprendizaje profundo (*Deep Learning*), en el diagnóstico médico [1].

De la misma manera, la calidad en los procesos industriales se ha incrementado notablemente al utilizar inteligencia artificial para mejorar la precisión en la detección de diversos tipos de defectos en manufactura [2]. De manera particular, es posible utilizar imágenes en las diversas etapas del proceso de fabricación e incluso en la pieza terminada y ayudarse de ellas, clasificándolas, para determinar su calidad.

Como es sabido, la clasificación de imágenes se refiere a la tarea de extraer todo tipo de información de una imagen. Aunque existen dos tipos de clasificación, nosotros usaremos la clasificación supervisada. Este tipo de clasificación, parte de un conjunto de clases conocido. Estas clases deben caracterizarse en función de valores establecidos en un conjunto de variables que poseen los objetos de interés en las imágenes.

En el presente trabajo se aplica la inteligencia artificial en la clasificación automática de imágenes de piezas automotrices que presentan o no, omisión de puntos de soldadura. Por lo anterior, estas imágenes son clasificadas en dos posibles categorías: defectuosas y no defectuosas.

El Resto del artículo se encuentra organizado de la siguiente manera: en la sección 2 se presenta una breve descripción del problema a resolver. En la sección 3 se presenta el método propuesto, con una breve descripción de las variables y algoritmos utilizados. Posteriormente, en la sección 4, se presentan los resultados de la evaluación del método propuesto y finalmente, en la sección 5 hemos colocado las conclusiones del trabajo.

2. Descripción del problema

Una cierta compañía que fabrica autopartes, produce una en la que es necesario colocar 8 puntos de soldadura en ciertas posiciones de la pieza. En la figura 1a es posible apreciar la pieza fabricada con los 8 puntos de soldadura necesarios, ya que han sido etiquetados de forma manual con un recuadro en rojo.

Debido a que el proceso de colocar los puntos de soldadura lo realizan varios operadores de forma manual, es posible que pueda existir un error en la pieza al omitir uno o más puntos de los 8 necesarios, como se puede apreciar en la Figura 1b. Por esta razón, al final del proceso, cada pieza es inspeccionada, también manualmente, para verificar el cumplimiento de esta condición.

Este trabajo propone el uso de aprendizaje de máquina en imágenes de las piezas, en las que sea posible reconocer, de manera muy precisa, cualquier pieza defectuosa, es decir, que no cuente con los 8 puntos de soldadura.

3. Descripción del experimento

Para el presente trabajo creamos una base de datos mediante la adquisición de 115 imágenes, de las cuales 70 de ellas corresponden autopartes con 8 puntos de soldadura (No defectuosa) y las 45 imágenes restantes son de piezas en las que falta uno o más puntos de soldadura (Defectuosas).

(a) (b)

Fig. 1. Autopartes fabricadas, manualmente etiquetadas. a) Con 8 puntos de soldadura (no defectuosa). b) Con 7 puntos de soldadura (defectuosa).

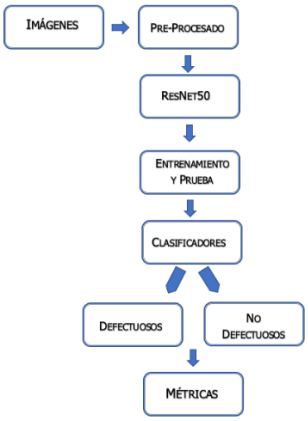

Fig. 2. Diagrama de flujo de la metodología realizada bajo el escenario de "Conjunto de entrenamiento y Prueba".

Posteriormente, correspondiendo al escenario de; Conjunto de entrenamiento y Prueba, a las imágenes se les realizó un pre-procesamiento a las imágenes utilizadas, ver Fig. 2. Este procedimiento es simple y es un requisito necesario para el siguiente paso. El pre-procesamiento, consiste en dos partes: (1) Relleno (*Padding*) y (2) Redimensionamiento (*Resizing*). Al final de esta etapa tendremos una matriz para cada imagen con dimensiones de 224 x 224 y con números del 0 al 255 en 3 canales (RGB).

El objetivo del pre-procesamiento es la de estandarizar todas las imágenes a las dimensiones mencionadas. Posteriormente, con el objetivo de mejorar los resultados de los métodos de clasificación, la matriz de imágenes es ingresada a la red neuronal; ResNet50, con el fin de obtener un vector de características de las imágenes.

La dimensión del vector resultante es 2048 y posee las características generales de las imágenes tales como: intensidad, brillo, luminosidad, etc. Estas, alimentarán a los

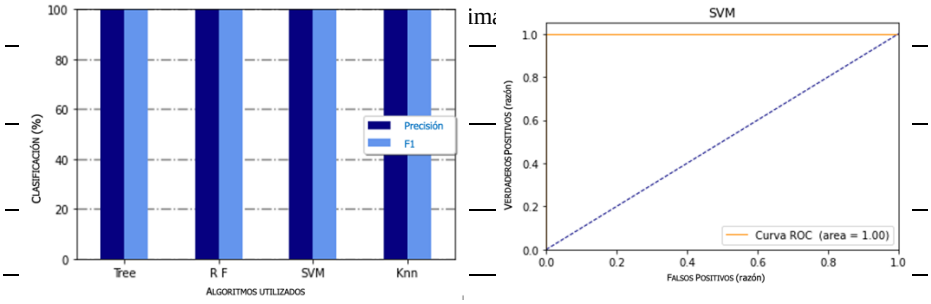

(a) (b)

Fig. 3. a) Resultados de las métricas "Precisión" y "F1" para cada uno de los 4 métodos de clasificación utilizados, b) Curva ROC para el método de Máquina de Vector de Soporte (SVM).

clasificadores con la finalidad de que puedan ayudar a discernir de mejor forma entre las dos clases posibles. Posteriormente, se crearon los conjuntos de Entrenamiento y Prueba, con el 80 % y 20 % del total de las 115 imágenes, respectivamente.

Posteriormente, con el fin de comparar resultados, utilizamos 4 métodos de clasificación: Máquinas de vector de soporte, Regresión Logística, Vecinos Cercanos y Árbol de Decisiones. Finalmente, los resultados son evaluados mediante dos métricas; Precisión y F1.

4. Resultados

Una vez realizadas las métricas de "Precisión" y "F1" a los resultados de clasificación realizada en el conjunto de prueba, los resultados arrojan un 0 % de error, como puede observarse en la fig. 3a. El mismo resultado es obtenido, independientemente del método de clasificación utilizado. La figura 3b presenta la curva ROC obtenida para el método de clasificación; Máquina de Vector de Soporte (SVM, por sus siglas en inglés).

Otra forma de poder apreciar los resultados es mostrada en la Tabla 1. En ella es posible verificar la forma en que las imágenes de las piezas, en el conjunto de prueba, fueron clasificadas. Puede observarse que todas las piezas fueron clasificadas de manera correcta, es decir, todas las imágenes de piezas no defectuosas fueron clasificadas como no-defectuosas (ND), de la misma forma con las imágenes que contienen piezas defectuosas fueron clasificadas como defectuosas (D).

5. Conclusiones

Los resultados obtenidos permiten concluir que la metodología propuesta es suficiente para obtener un sistema que permita discriminar las piezas defectuosas, mediante sus imágenes, con una precisión del 100 %. Esto es independientemente del método de clasificación usado y no es necesario probar un escenario distinto.

Agradecimientos. Este trabajo ha sido apoyado parcialmente por el Consejo Mexicano de Ciencia y Tecnología (CONACyT) mediante los apoyos: CB2016-286368 and CB-2016-01-286629, así como por la Universidad de Guanajuato mediante el apoyo CIIC-57/2022.

Referencias

1. Bagchi, S., Huong, A.: Signal processing techniques and computer-aided detection systems for diagnosis of breast cancer: A review paper. Indian Journal of Science & Technology, vol. 10, no. 3, pp. 1–6 (2017) doi: 10.17485/ijst/2017/v10i3/110640
2. Malkoff, D. B.: A framwork for real-time fault detection and diagnosis using temporal data. Artificial Intelligence in Engineering, vol. 2, no. 2, pp. 97–111 (1987) doi: 10.1016/0954-1810(87)90144-0

Electronic edition
Available online: http://www.rcs.cic.ipn.mx

http://rcs.cic.ipn.mx

Centro de Investigación
en Computación